Human danger zones in compact and modular air insulated 110 kV substations

Jan Kruize

TU Delft

Human danger zones in compact and modular air insulated 110 kV substations

door

Jan Hilvert Kruize

ter verkrijging van de graad van Master of Science
aan de Technische Universiteit Delft,
in het openbaar te verdedigen op woensdag 1 juli 2026 om 13.00 uur.

Studentnummer:	5261961	
Projectperiode:	november 2025 - juli 2026	
Afstudeercommissie:	prof. ir. P.T.M. Vaessen	TU Delft, eerste begeleider
	dr. ir. D. van der Born	TU Delft, dagelijks begeleider
	ir. C.S. Engelbrecht	TU Delft, dagelijks co-begeleider
	dr. J. Dong	TU Delft, onafhankelijk lid

HIGH VOLTAGE TECHNOLOGIES

TU Delft

Abstract

In the coming years, a large portion of the 110 and 150 kV substations in the Netherlands will be replaced. For this, the Dutch TSO TenneT has introduced the Bay Replacement Program (BRP), in which the old bays are being replaced completely by standard, modular, and compact skid-mounted bays. These bays are, in principle, plug-and-play, except for the busbar disconnector, for which the pantograph has to be aligned to the overhead busbar. To make substations even more compact in the future, this thesis aims to investigate the switching impulse breakdown strength of short air gaps relevant to maintenance of the 110 kV BRP busbar disconnector, in order to determine the minimum safety clearances.

The validity of the Schneider and Weck method for simulating the gap factor of short gaps (gap distance smaller than 2 meters) is investigated. Electric field simulations in COMSOL were compared with the original results from Schneider and Weck. The simulations reproduce the original results with deviations below 5% for gaps larger than 2 meters. For gaps smaller than 2 meters, the results show irregular behaviour. Experiments on a rod-plane and conductor-rod gap showed that the simulated gap factor deviates significantly from the experimentally found gap factor, and the Schneider and Weck model is therefore considered to be invalid for air gaps smaller than 2 meters. The experiments on a rod-plane and needle-plane show that the Feser equation best describes the breakdown strength of short rod-plane gaps, while the CRIEPI equation provides a conservative value suitable for clearance determination.

Experiments on the BRP busbar disconnector were conducted in the TU Delft high voltage laboratory to investigate the gap factor that may occur during maintenance. Four different gaps were tested: conductor-rod, pantograph-rod, pantograph-needle, and earthing contact-needle. The results show that the earthing contact-needle gap has the lowest gap factor of $k_g = 1.20$, and hence is the determining gap for the critical clearance. This critical clearance is found to be 45.6 cm, based on a worst-case risk evaluation. The currently enforced critical clearance by TenneT of 47.9 cm is considered to be adequate. A simulation is performed to study the minimum clearances related to the electric field.

Contents

1

Introduction

Since the 1990s, the electricity consumption of the Netherlands has increased by about 50% [1]. The prediction is that the energy demand of existing consumers will reduce by 7 to 39% due to new technologies, energy savings, and increased efficiencies. However, new consumers (e.g. data centres) and the energy transition will cause the overall energy demand to increase by 180 to 250% due to significant electrification in almost all end-user sectors [2], [3].

To meet this increase in demand, the Dutch Transmission System Operator (TSO), TenneT, has to modernise their high voltage grid to prepare for future demand. A separate problem lies in the regional transmission grid (110 and 150 kV), as the substation components are reaching the end of their lifetime or have already surpassed it. To replace these components in a fast and efficient manner, TenneT introduced the Bay Replacement Program (BRP). This program targets substations where both the primary and secondary components are due for replacement. The existing bays are being replaced completely by retractable, standard, modular, skid-mounted bays. A total of 140 substations will be modernised in the coming years [4], [5]. Figure 1.1 shows a substation with the compact and modular bays.

Figure 1.1: BRP substation with compact and modular bays. Image courtesy of C. Engelbrecht

The BRP stations are very compact in design, which prohibits maintenance without de-energising, dismounting, and extracting the bay at hand to a safe working area. However, not all maintenance can be performed with the bay in the safe working area, for instance, alignment of the pantograph busbar disconnector (see Figure 1.2) to the overhead busbar. Therefore, the bays are separated by a safe distance that allows for maintenance. To allow for further compaction in the future, it is necessary to determine how small these safety distances can become without compromising safety. The high voltage laboratory of TU Delft has been lent a 110 kV BRP busbar disconnector by TenneT. Determining the minimum safety clearances of this busbar disconnector is the main goal of this thesis.

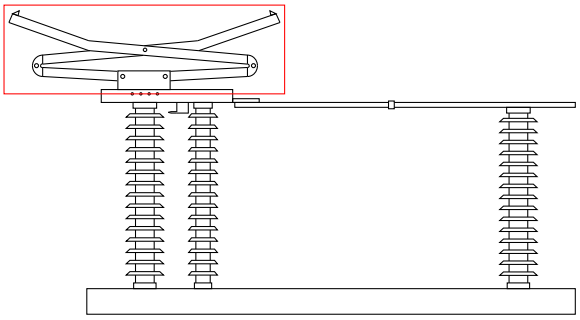

(a) One phase of the BRP skid-mounted busbar disconnector, with the pantograph boxed

(b) Pantograph connected to the overhead busbar. Image courtesy of C. Engelbrecht

Figure 1.2: BRP busbar disconnector pantograph and its connection to the overhead busbar

Main research objective

To define minimum safety clearances for the 110 kV BRP busbar disconnector.

To determine these safety clearances, the method defined in the IEC 61472 standard [6] is used. The clearances are determined based on, among other factors, a representative overvoltage that may occur on the bay and on a gap factor. This gap factor defines the relative strength of the clearances and is based on the geometry of the specific high voltage component and its surroundings. A method to simulate the gap factor is presented by Schneider and Weck [7], it is, however, only proven to be valid for gap distances larger than 2 meters. Literature provides references for the gap factor for relatively simple gaps with a gap distance larger than 2 meters. As the nominal voltage of the BRP busbar disconnector is relatively low, the gap distances will be shorter than 2 meters. Therefore, this work will investigate the validity of methods and equations for complex air gaps shorter than 2 meters. This gives rise to the following secondary research objectives:

Secondary research objective

To define gap factors for gaps occurring during maintenance of the 110 kV BRP busbar disconnector.

Secondary research objective

To validate the method of Schneider and Weck [7] for determining gap factors when applied to air gaps shorter than 2 meters.

1.1. Outline of chapters

This thesis is structured as follows: Chapter 2 explains in detail safe work procedures, clearance determination, switching surge strength, and introduces two methods to determine the gap factor. Chapter 3 elaborates on the gap factor simulation method from Chapter 2. Chapter 4 first introduces different high voltage testing methods and the analysis of results. It then describes the experimental work on simple geometries, the rod-plane, needle-plane and conductor-rod gap. As a logical next step, Chapter 5 describes the experimental work on complex geometries, namely gaps that are found around the busbar disconnector during maintenance. Chapter 6 combines the preceding chapters and introduces electromagnetic safety limits. These two factors combined will lead to defining the safety distance for personnel working on the BRP busbar disconnector. Chapter 7 discusses the findings of this work. Lastly, in Chapter 8, a conclusion, recommendations and directions for future work are presented.

2 Background

This chapter describes the background on the equations, models, and methods used.

2.1. Safe work procedures

Safe working is a top priority in all industries, but it becomes even more important when high voltages are involved. Working close to an energised part could potentially result in a breakdown, being lethal for the worker, and a blackout in case of a short-circuit, affecting a large number of consumers. Therefore, the conditions under which work may be performed close to an energised part are very strictly controlled and carefully described. For this, safety zones around an energised part are defined as shown in Figure 2.1. The parameters in Figure 2.1 are described below [8].

- D_L is the live working zone. Working in this zone has to be considered as working on an energised part, and is only allowed if live working techniques, tools and procedures are used. The minimum value of D_L is determined by calculating the electrical distance D_U, and adding a safety margin. D_U is the maximum distance at which sparkover to a grounded object can reasonably occur.
- D_V is the vicinity zone. Working in this zone is only allowed for trained personnel.
- D_E is an ergonomic component. This can be added to D_L to ensure that even during inadvertent movements, the live working zone will not be entered.

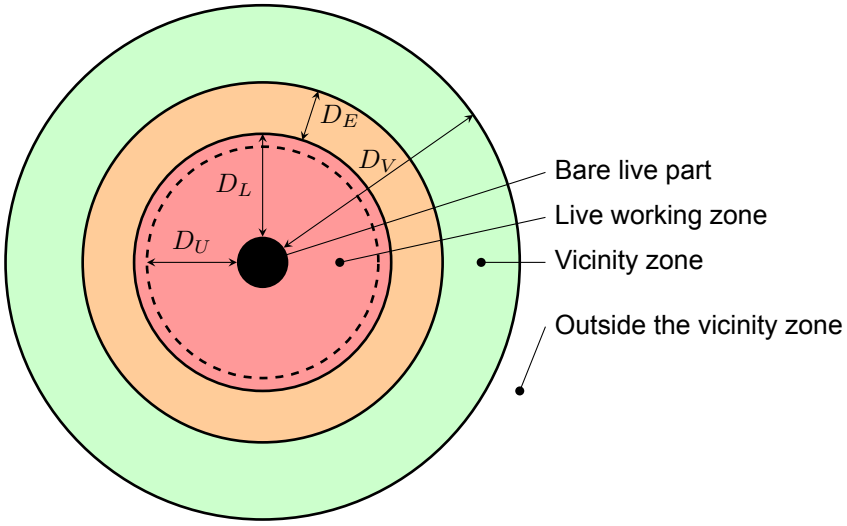

Figure 2.1: Definition of danger zones, based on [6], [8]

Both D_E and D_L are administratively defined. For this thesis, D_U is of main interest. The current

working distances TenneT enforces for the BRP project are listed in Table 2.1.

Table 2.1: Current danger zones, defined by TenneT [9]

U_n	D_U	D_L	D_E	D_V
110 kV	479 mm	500 mm	500 mm	1000 mm
150 kV	689 mm	700 mm	500 mm	1200 mm

N.B. *Unless stated otherwise, power-frequency system voltages (U_n, U_m) are given as RMS phase-to-phase voltages. Per-unit voltages are expressed relative to the phase-to-ground peak operating voltage. Impulse voltages (LIWV, SIWV) and statistical breakdown voltages (e.g., U_{50}, U_{10}) are expressed as peak values.*

In the design of high voltage systems, specifying the right insulation level is essential to prevent breakdowns. Breakdowns, however, do not behave like a step function, but are probabilistic. Because the phenomenon is not binary, selecting an appropriate insulation level is more involved than selecting one threshold value. The procedure of choosing the suitable insulation level is called insulation coordination. It is a trade-off between stress (what overvoltages are to be expected on the circuit) and strength (what is the maximum overvoltage that should not cause a flashover over the insulator). The stress can be determined through network transient studies (e.g. using EMTP-ATP), and the strength can be tested in a high voltage laboratory. Insulators are defined by their withstand voltage under a certain type of stress (e.g. 50 Hz AC, lightning impulse, etc.).

Based on the international standard for insulation coordination, IEC 60071-1 [10], substations can be divided into two ranges based on their maximum operating voltage. Substations with $U_m \leq 245$ kV are categorised as range I systems, and substations with $U_m > 245$ kV are categorised as range II systems. The following rated withstand voltages are used to define the rated insulation level (i.e. the insulation strength) [10]:

1. For equipment in range I ($U_m \leq 245$ kV):
    a. the standard rated lightning impulse withstand voltage (LIWV)
    b. the standard rated short-duration power-frequency withstand voltage (ACWV)
2. For equipment in range II ($U_m > 245$ kV):
    a. the standard rated switching impulse withstand voltage (SIWV)
    b. the standard rated lightning impulse withstand voltage (LIWV)

This thesis discusses the clearances for a $U_n = 110$ kV BRP station, with a maximum operating voltage of $U_m = 123$ kV, resulting in a phase-to-ground peak voltage of $U = 123\sqrt{2/3} \approx 100$ kV, which is defined as 1 p.u. Hence, this substation is categorised as a range I substation. As explained above, for equipment in this range, the insulation level is defined by the standard lightning impulse and standard short-duration power-frequency withstand voltages. TenneT determines air insulation distances solely by transient overvoltages [11], and as IEC 60071-1 [10] does not specify SIWV as a parameter for range I equipment, the SIWV and switching overvoltages in a range I system are generally not considered, and therefore not properly defined.

It is not allowed to perform work in a substation when lightning is visible, or thunder is heard within 10 kilometres of the station [12], which rules out lightning as a potential cause for overvoltages during maintenance activities. As a consequence, only switching overvoltages need to be considered and are used to calculate the safety clearances [6]. This raises an important contradiction for range I equipment. For dimensioning the insulation of range I equipment, switching overvoltages are not taken into account, but for determining safety clearances, switching overvoltages are the most important factor. As a result, little information is available on the switching impulse strength of range I substations and the applicability of the equations used to determine clearances.

In situations where switching overvoltages need to be considered, the LIWV can be converted to an equivalent SIWV that can be used to determine the correct insulation level for the range I system.

IEC 60071-2 [13] gives a method to relate the two withstand voltage levels: LIWV $=$ SIWV$(1.05 +$ SIWV$/6000)$, and consequently:

$$\text{SIWV} = -3150 + \sqrt{3150^2 + 6000 \times \text{LIWV}} \tag{2.1}$$

The LIWV for the BRP busbar disconnector is 550 kV $= 5.5$ p.u. [11]. According to Equation 2.1, the expected SIWV of the busbar disconnector would be 486.27 kV ≈ 4.9 p.u.

2.2. Determining the live working zone

The international standard on live working (IEC 61472 [6]) gives a method for calculating the live working zone (D_U in Figure 2.1). This method is illustrated in the flowchart in Figure 2.2, and described in more detail below.

N.B. *IEC 61472 does not use the same terminology as the standards on insulation coordination (IEC 60071). In this flowchart, the terminology of the IEC 61472 standard is used.*

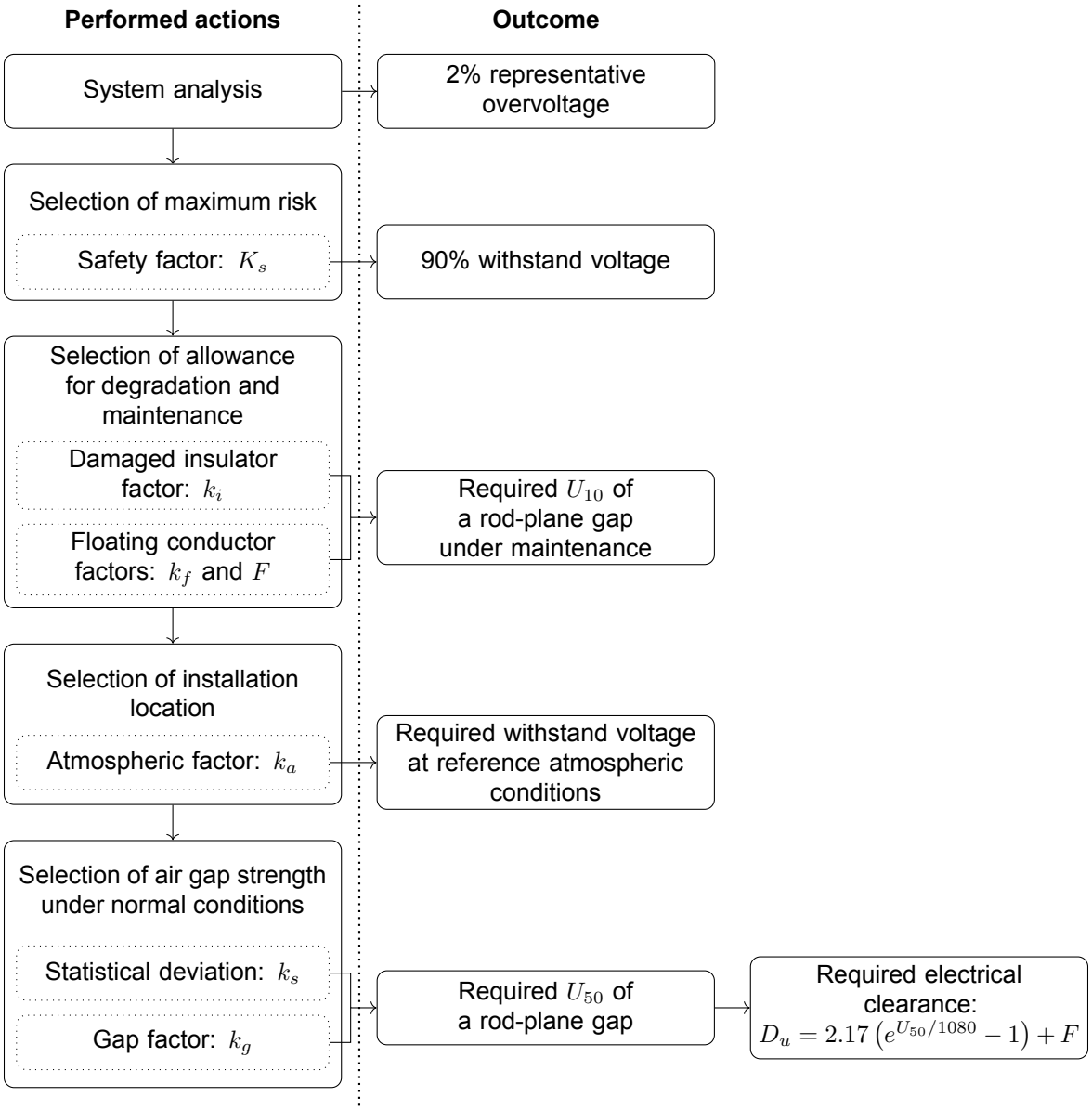

Figure 2.2: Flowchart to determine the electrical clearance, based on [6], [13], [14]

System analysis: As described in Section 2.1, only switching overvoltages need to be accounted for when determining D_U. The IEC 61472 standard takes the 2% switching overvoltage, which can be determined using a system study (e.g. with EMTP-ATP), or using Figure 2.3.

Safety margin: The safety margin K_s relates the 2% switching overvoltage to the 90% withstand voltage U_{10}. The safety margin K_s can be set to $K_s = 1.1$ if no ergonomic component D_E is defined in the zones, and to $K_s = 1.0$ if an ergonomic component is defined. In both cases, Equation 2.2 should hold. This states that, even if an ergonomic component is added and $K_s = 1$, the total clearance should be larger than when setting $K_s = 1.1$ without an ergonomic component.

$$D_{U(K_s=1.0)} + D_E > D_{U(K_s=1.1)} \tag{2.2}$$

N.B. This is different from IEC 60071-2, where the coordination withstand voltage is related to the representative overvoltage with a deterministic or statistical coordination factor, and a safety factor is only introduced to differentiate between internal and external insulation.

Damaged insulators, k_i: This factor takes into account working next to damaged insulators. Its value is based on the length of undamaged insulators (A_o), length of damaged insulators (A_d) and a coefficient related to the material of the insulator ($k_d = 1$ for toughened glass insulators, $k_d = 0$ to 1 for porcelain insulators, and $k_d = 1.25$ for composite insulators). This results in $k_i = 1 - 0.8k_d(A_d/A_o)$. In this work, damaged insulators are not considered, resulting in $k_i = 1$.

Floating conductors, k_f & F: Conductors at floating potential in the gap influence the strength of the gap. Determining their influence is more elaborate, refer to [6, Sec. 4.3.2.4]. This work does not consider floating conductors, resulting in $k_f = 1$ and $F = 0$.

Atmospheric factor, k_a: The atmospheric factor accounts for the effect of humidity and air density, which is influenced by temperature and altitude. The combined effect of temperature and humidity is considered negligible in comparison with the effect of altitude [13]. The average altitude in the European Netherlands is around 30 meters above sea level [15], which results in an atmospheric factor of $k_a = 1$. If, however, the highest part of the European Netherlands is taken (around 300 m above sea level [16]), this atmospheric factor changes to $k_a = 0.983$. A full list of k_a values is shown in [6, Tab. 1].

Statistical deviation factor, k_s: This factor accounts for the statistical nature of the breakdown voltage, and relates U_{50} to U_{10} via $U_{50} = U_{10}/(1 - 0.0128\sigma) = U_{10}/k_s$. A standard value of $k_s = 0.936$ ($\sigma = 5\%$) can be used in case U_{50} was calculated [6]. [13] suggests $\sigma = 6\%$ and [17] proposes $\sigma = 7\%$. If U_{50} is known from tests, the resulting standard deviation of that test should be used.

Gap factor, k_g: The gap factor accounts for the geometry of the gap and relates the 50% breakdown voltage of the gap of interest to the 50% breakdown voltage of a rod-plane gap. This factor will be discussed in detail in this thesis.

Operational factor, K_t: The operational factor is the multiplication of all the previous factors, i.e., $K_t = k_s k_g k_a k_f k_i$.

N.B. This is different from the flowchart in Figure 2.2, where the different operational factors are shown separately.

Final clearance determination: The electrical clearance D_U is determined using the CRIEPI equation (Eq. 2.6), which relates the U_{50} of a rod-plane for a critical switching overvoltage to the gap distance. Using the operational factor K_t, and the floating conductor length F, the electrical distance can be calculated using Equation 2.3 [6].

$$D_U = 2.17\left(e^{U_{10}/(1080K_t)} - 1\right) + F \tag{2.3}$$

2.3. Switching overvoltages

Switching overvoltages are transients that occur in the power system due to sudden changes in the network conditions, usually due to switching operations. This could, for instance, be the energisation or de-energisation of a line or cable, transformer switching or restrikes in a circuit breaker. The magnitude of the overvoltage due to a switching operation is highly dependent on the system and its components.

Switching overvoltages in a network are usually characterised by a representative overvoltage which has a 2% probability of exceedance (this is the 2% representative overvoltage in Figure 2.2). Typical values of the representative overvoltages that can be expected in EHV and UHV networks are presented in Figure 2.3. Depending on the system and components, they typically range from 1 p.u. to 3.7 p.u. The maximum overvoltage due to a switching operation rarely exceeds 4.9 p.u. [18]. This specific overvoltage may occur on a reclosed line after clearing a multi-phase fault on a radial network with a conventional circuit breaker.

Although [6] and [18] do not fully agree on the overvoltages to be expected, they give a good indication. In the previous subsection, the equivalent SIWV of the BRP busbar disconnector was calculated to be 4.9 p.u., and [18] specified the maximum overvoltage due to a switching operation to be 4.9 p.u., hence the SIWV of the busbar disconnector is right at the boundary. However, only considering the maximum overvoltage of 3.7 p.u. specified in [6], the SIWV of the busbar disconnector would be sufficient.

The Nota Isolatiecoördinatie (memo on insulation coordination for Dutch high voltage grids) [19] reports on the Dutch grid, where the maximum overvoltage due to switching is found to be 3.7 p.u. This value is retrieved from [13, Fig. 1] (on which Figure 2.3 is based) [19]. These overvoltages do not consider the presence of surge arresters.

A recent measurement study in the 110 kV TenneT grid shows however, that the maximum overvoltage in a substation observed over one year is 1.55 p.u. [20]. The study includes around 300 measurements that include system faults (15 events), transformer (15 events) and other component switching (200 events), and unknown events (40 events).

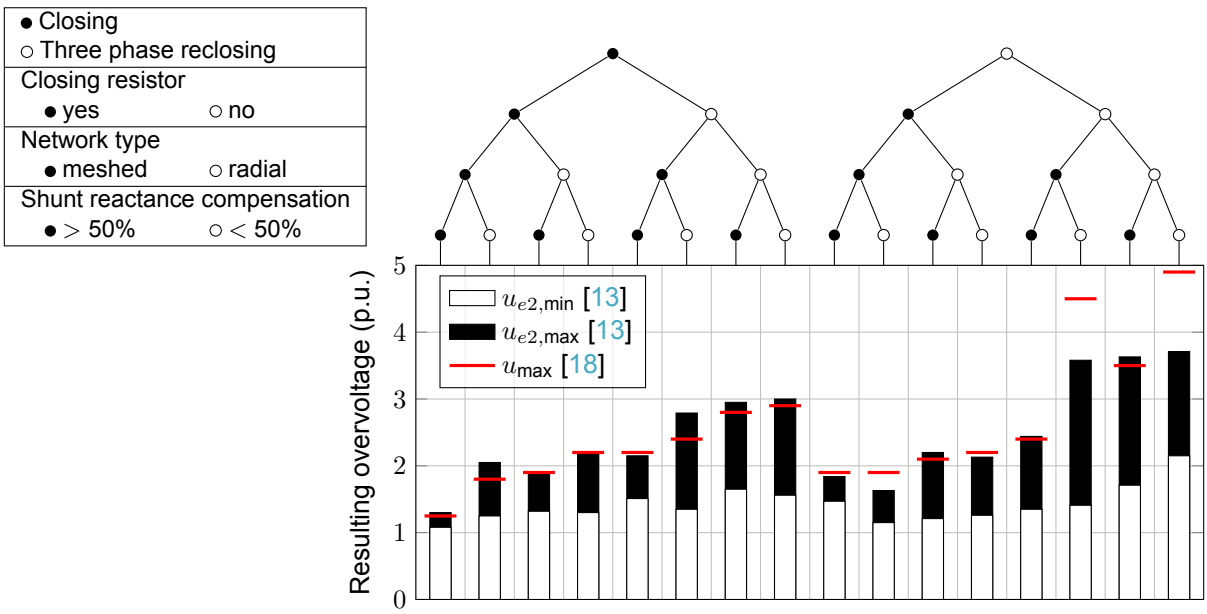

Figure 2.3: Overvoltages to be expected due to different switching operations

During maintenance operations, switching overvoltages may be reduced due to restrictions on switching operations during the period of maintenance. Absence of switching operations can however not be guaranteed, as involuntary switching operations due to faults or other abnormal system conditions can not be planned nor postponed. Therefore, the conservative assumption is made that there will be no restrictions on switching operations during the period of maintenance.

The insulation strength under switching surges is determined with an impulse voltage. This impulse ideally has a double exponential wave shape, which is defined by its peak voltage U_{pk}, the time-to-crest T_{cr}, and the time-to-half T_{tail} [21]. These parameters are graphically shown in Figure 2.4.

N.B. This is the definition as per the IEC 60060-1:2010. The most recent version of the standard, IEC 60060-1:2025, uses a front time T_1 instead of the time-to-crest.

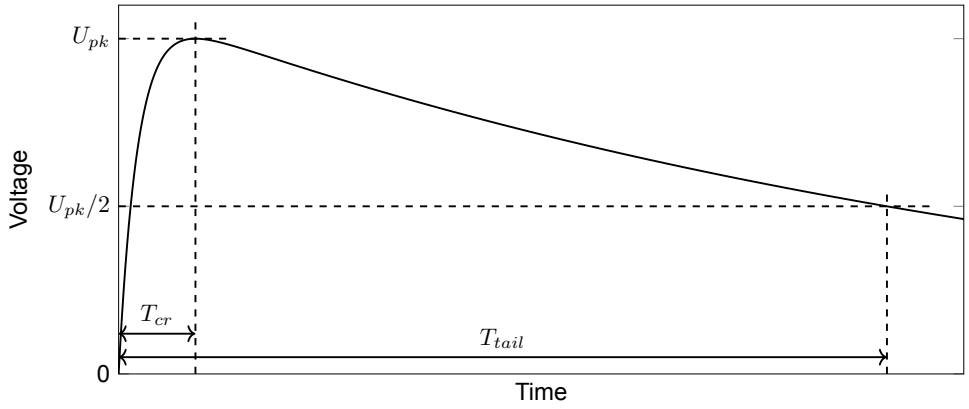

Figure 2.4: Impulse wave with its parameters

To systematically test high voltage equipment for this kind of overvoltages, a standard switching impulse is defined. The standard switching impulse has a time-to-crest of $T_{cr} = 250$ µs and a time-to-half of $T_{tail} = 2500$ µs. The U_{50} for this standard switching impulse on a rod-plane gap, as shown in Figure 2.5, is known as the Paris equation [22] and is defined in Equation 2.4. This equation holds for $2 < d < 6$ m.

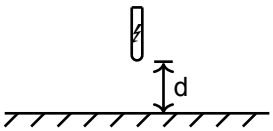

Figure 2.5: Rod-plane gap

$$U_{50,r-p} = 500d^{0,6} \tag{2.4}$$

Where d is the gap spacing in meters, and $U_{50,r-p}$ the 50% breakdown voltage in kV.
Switching surges in the electric power system do not always have the same wave shape, i.e. every surge might have a different T_{cr} and T_{tail}. Laboratory tests have shown that the switching breakdown voltage is highly dependent on T_{cr}, and only very little on T_{tail}. It was found that for every gap length, there is a critical value of T_{cr}, where the breakdown voltage U_{50} reaches a minimum value [23], [24]. This is shown in Figure 2.6 for rod-plane gaps at different laboratories and gap distances of 0.5 and 1 meters.

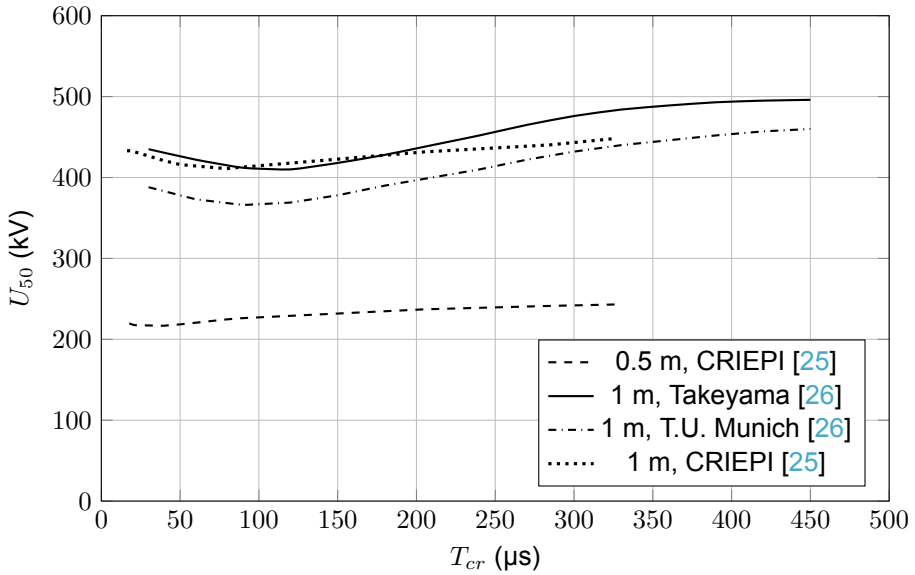

Figure 2.6: Positive rod-plane breakdown voltage as a function of T_{cr}

The positive flashover strength of a rod-plane gap at critical time to crest, with a validity of $1 < d < 21$ m, is defined by Gallet et al. [26] as:

$$U_{50,r-p,cr} = \frac{3450}{1 + \frac{8}{d}} \tag{2.5}$$

and separately by CRIEPI [25], for $0.5 < d < 12$ m:

$$U_{50,r-p,cr} = 1080 \ln(0.46d + 1) \tag{2.6}$$

Feser [27] introduced an equation for the flashover strength of specifically short rod-plane gaps under switching impulses with a $60/525$ µs wave shape, being valid for $0.4 \leq d \leq 3$ m:

$$U_{50,r-p} = 100\sqrt{50d + 1} - 250 \tag{2.7}$$

All the four equations mentioned above are shown in Figure 2.7.

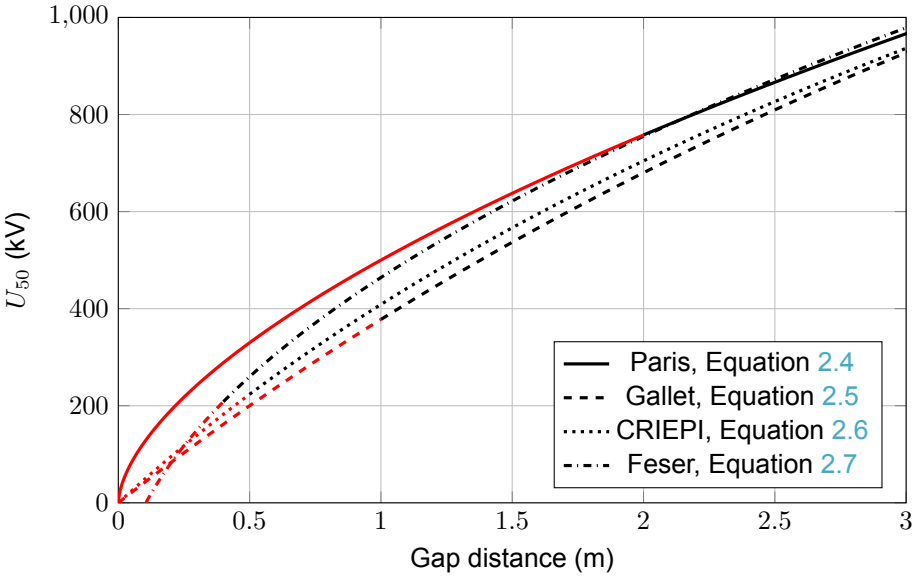

Figure 2.7: Rod-plane gap strength for positive switching impulses. Extrapolation of the breakdown equations outside their validity range is shown in red.

It can be concluded from Figure 2.7 that both the Gallet and the CRIEPI equations are closely related to each other, and that the Paris equation shows a higher U_{50} (as this equation is defined for the standard impulse, not the critical). The Feser equation lies between the Paris and CRIEPI equations for $0.25 < d < 2.1$ m. There is a large spread amongst these four equations (around 80 kV at a gap distance of 1 m), potentially leading to incorrect clearances. Typical air gaps in 110 and 150 kV networks are in the order of 1 to 1.5 m [9], and therefore it is important that the equation that represents this range best is used for clearance determination.

The breakdown strength of a gap under negative switching impulses is usually higher than under positive switching impulses. The U_{50} of a rod-plane gap for critical negative switching impulses is given in Equation 2.8. This equation is valid for $2 < d < 14$ m [17], [28].

$$U_{50,r-p,cr} = -1180d^{0.45} \tag{2.8}$$

2.4. Rod diameter

For smaller gap spacings, it is found that the shape and size of the electrode may have an influence on the breakdown strength. Especially, the diameter of the rod in a rod-plane geometry is of interest [29]. For every gap distance of a rod-plane gap, there exists a maximum radius below which the breakdown strength is not dependent on the rod radius anymore [29], [30]. This radius is called the critical radius, and is illustrated in Figure 2.8, where the dashed line shows inter- and extrapolated values of the results from [29].

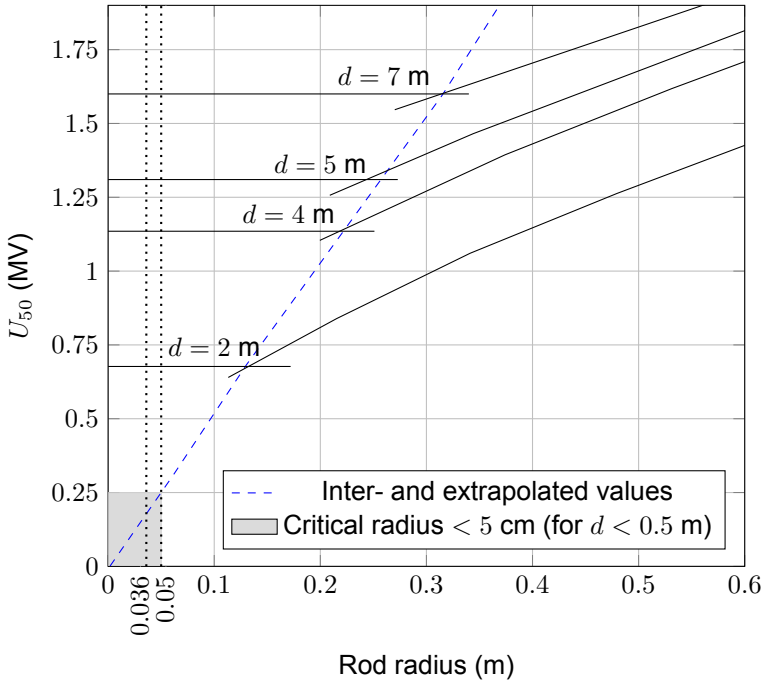

Figure 2.8: Critical radii for different gap distances d, modified from [29, Fig. 4]

The concept of the critical radius is also introduced by the Les Renardières Group [31], with the formula:

$$R_c = 38\left(1 - e^{-d/500}\right) \tag{2.9}$$

where R_c is the critical radius in cm and d is the gap distance in cm. For a gap distance of $d = 0.5$ m, this leads to a critical radius $R_c \approx 3.6$ cm. The anticipated breakdown voltage for a gap distance of 0.5 m is around 250 kV (see Equation 2.7), which leads to a critical radius of around 5 cm using Figure 2.8. Therefore, the critical radius is expected to be at the lowest 3.6 cm.

2.5. Gap factor

Paris [22] first discussed the idea of the gap factor, as a method for estimating the flashover strength of practical gaps in substations and overhead lines. It relates the 50% breakdown voltage (U_{50}) of any gap geometry with the positive U_{50} of a rod-plane gap as follows:

$$k_g = \frac{U_{50,\text{gap}}}{U^+_{50,\text{rod-plane}}} \tag{2.10}$$

As the rod-plane gap is considered to have the lowest breakdown strength among all gap geometries, it represents the worst case, i.e., $k_g \geq 1$. The initial research of Paris performed tests for 13 different gaps, with the gap factor in the range $1.00 \leq k_g \leq 1.90$. Other references show slightly different gap factors [6], [17], although they are in a similar range. As the gap factor can be as high as 1.9, considerable errors can be made when not taking the gap geometry into account when dimensioning air insulation [32]. The U_{50} is generally lower for switching impulses of positive polarities, but for $k_g \gtrapprox 1.5$, the negative polarity switching impulses may cause a breakdown at lower voltages [13], [23], [33]. A list with common ranges of gap factors is shown in Table 2.2.

Table 2.2: Ranges of gap factors for different gap configurations under positive impulses [17]

Gap configuration	Range of gap factors k_g
Rod-plane	1.00
Vertical rod-rod	$1.25 - 1.35$
Horizontal rod-rod	$1.25 - 1.45$
Conductor-lateral structure	$1.25 - 1.40$
Conductor-lower rod	$1.40 - 1.60$
Conductor-plane	1.15
Post insulator	1.18

Schneider and Weck [7] introduced a method that allows the gap factor under positive impulses to be deduced from the asymmetry and inhomogeneity of the electric field distribution in the gap, in an attempt to eliminate the need for costly laboratory tests. Their method is described in more detail below.

Inhomogeneity of the gap The inhomogeneity of the gap is mostly determined by the shape of the positive electrode. The higher the inhomogeneity of the gap, the lower the gap factor due to a higher electric field at the positively charged electrode. Gap inhomogeneity can be described as:

$$\int_0^{x_i} E(x)dx = \varphi(x_i) = F_i \tag{2.11}$$

The outcome of the integral, F_i, is the space potential at distance x_i at which the E-field is equal to the electric field of a homogeneous gap with the same gap distance ($E = U/d$, with U the applied voltage across the gap). This is graphically shown in Figure 2.9a. For the 9 gaps considered in the paper, x_i was in the range $0.8\,d < x_i < 0.95\,d$. Schneider and Weck found $x_i = 0.9\,d$ (90% of the gap distance) to give the best fit for different gap types and distances.

Symmetry of the gap The symmetry of the gap is mostly determined by the shape of the grounded electrode. The higher the symmetry, the higher the gap factor. An increased electric field at the grounded electrode leads to a decreased electric field at the positive electrode. This produces a definite minimum electric field within the gap. The space potential at this definite minimum describes the gap symmetry and is given by the following integral:

$$\int_0^{x_s} E(x)dx = \varphi(x_s) = F_s \tag{2.12}$$

This integral is shown in Figure 2.9b. The gaps studied by Schneider and Weck showed a minimum between $0.3\,d$ and $0.5\,d$. They concluded that $x_s = 0.4\,d$ (40% of the gap distance) gives the best fit amongst different gaps.

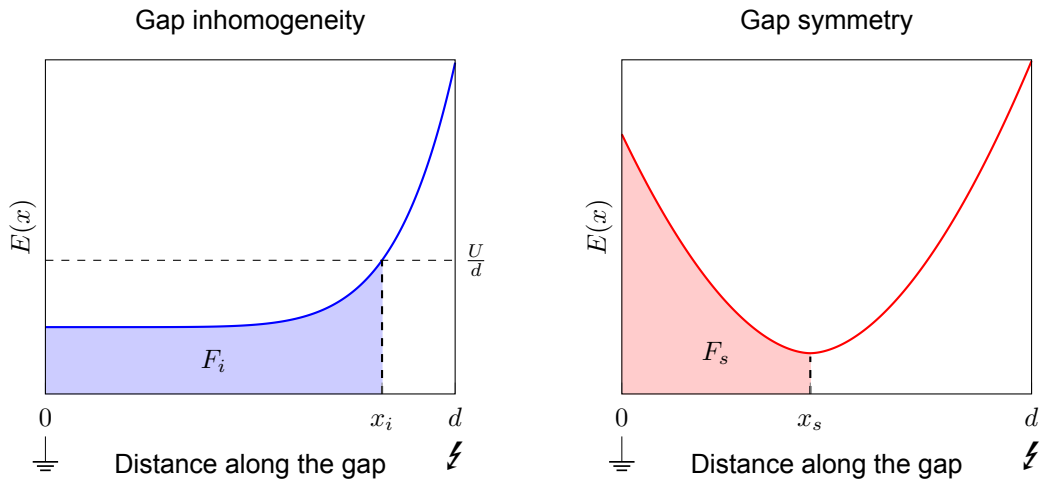

(a) Rod-plane gap: $F_i = \varphi(x_i)$

(b) Rod-rod gap: $F_s = \varphi(x_s)$

Figure 2.9: Definition of x_i and x_s, shown for different gaps

Based on the potentials described above, a ratio R is introduced:

$$R = \frac{\varphi(x_s = 0.4\,d)}{\varphi(x_i = 0.9\,d)} = \frac{\varphi_{40}}{\varphi_{90}} \tag{2.13}$$

This ratio relates to the gap factor k_g as:

$$k_g = 2.38R + 0.48 \tag{2.14}$$

Schneider and Weck validated this method with experiments in an electrolytical tank for different electrode configurations (rod-plane as the reference gap and 11 other gaps) and for four different gap distances (2, 3, 4, and 6 m). According to them, the validity of this method is limited by the minimum gap distance, from around 1 m at $k_g = 1$ to 2.7 m at $k_g = 2$ [7, Fig. 5]. Gaps shorter than 2 meters were not described or used to validate their model. As the gap distance for the 110 kV busbar disconnector may become lower than 2 m, the validity of this method for $d < 2$ m will be investigated.

2.6. Air gaps in substations

In substations, it is of great importance that the insulation strength is dimensioned well, as there might be people working there. Therefore, the gap factors proposed in standards are chosen to be conservative. Substations mainly have three types of phase-to-ground gaps [33]:

Type 1: Between conductors and portals

Type 2: Between live parts of the substation apparatus and portals

Type 3: Between conductor and ground

Gaps of type 1 are mainly encountered at the incoming overhead lines and at busbar portals in the substation. These gaps can be considered a conductor-lower structure gap with $k_g = 1.3$.
Type 2 gaps can be found between all types of apparatus (surge arresters, disconnectors, CTs, VTs, etc.) and portals. As all the apparatuses have different geometries, it is difficult to define one gap factor for all gaps. Therefore, a range of $1.1 < k_g < 1.3$ is used for these types of gaps. A configuration more similar to a rod-structure (e.g. an open disconnector switch near a portal) can be characterised by $k_g = 1.1$, whereas configurations more similar to a conductor-structure (e.g. a closed disconnector switch near a portal) can be characterised by $k_g = 1.3$.
The last gap is straightforward; it is the gap between an overhead conductor and the ground plane. These clearances are normally sufficiently high, as the busbars are supported by post insulators. For these types of gaps, a gap factor of $k_g = 1.1$ (rod-structure) covers all situations [33].

Minimum clearances for TenneT substations (including Table 2.1) are defined based on the rod-structure gap factor ($k_g = 1.1$) [11].

2.7. Breakdown mechanisms

When a high electric field is applied across an air gap, free electrons in the air are accelerated and collide with atoms, ejecting further electrons. This multiplication occurs entirely within the gas volume and is called an avalanche. This is depicted in Figure 2.10.

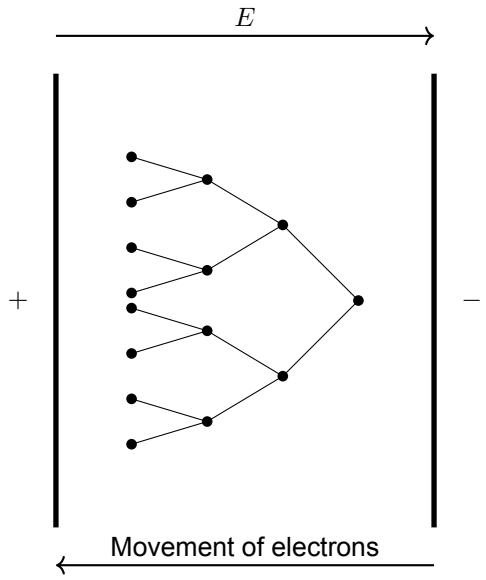

Figure 2.10: Electron avalanche

If the electric field only exceeds a critical threshold locally (near an electrode), avalanches remain confined to that region and cannot bridge the gap. This is called corona: a self-sustaining but localised discharge. It is characterised by a glow around the electrode.

When the electric field exceeds the critical threshold across a larger part of the gap, the space charge built up at the avalanche head distorts the local field enough to make the avalanche self-propagating. This propagating discharge is called a streamer. Under lightning surges, the gap is typically bridged in the streamer phase [34].

Under switching surges, where the electrical stress is lower, the streamer may transition into a leader. As the electron density in the streamer channel increases, energy transfer to surrounding ions and neutral atoms heats the gas locally. This thermal ionisation increases conductivity further until a hot, highly conductive plasma channel is formed, which is called a leader [34].

2.8. Research gap

The gap factor determined in literature is mostly defined for large air gaps ($d > 2$ m) and relatively simple geometries [7], [10], [23], [26], [32]. EPRI performed extensive literature research to gather literature containing breakdown values and gap factors for relatively long air gaps [35], and specifically for air gaps shorter than 1 m [36]. The gaps investigated in this research have relatively simple geometry. Gourgoulis et al. [37] report on breakdown experiments performed on a 50 cm conductor-rod gap, for both lightning and switching impulses. The aforementioned results are shown in Figure 2.11, together with the CRIEPI and Feser equations.

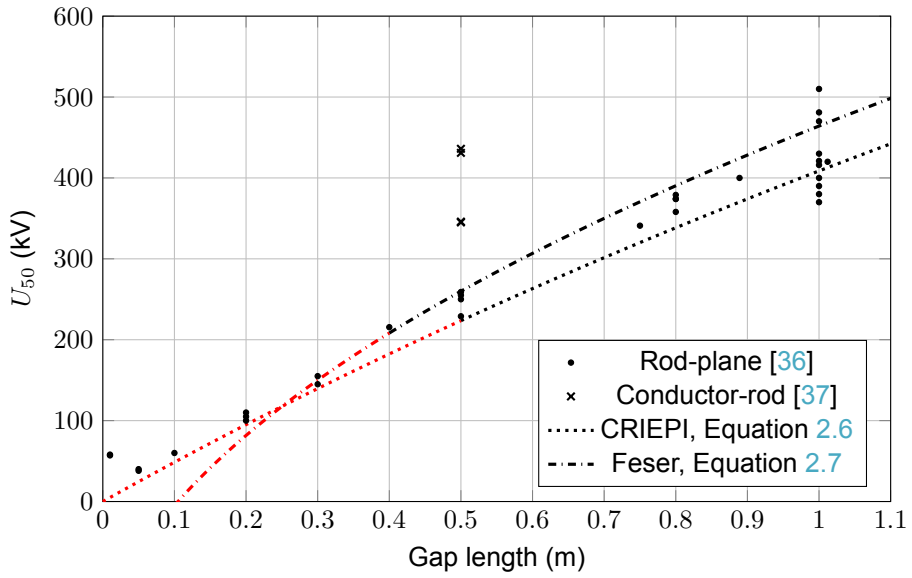

Figure 2.11: Breakdown voltages for rod-plane and conductor-rod gaps. The CRIEPI and Feser equation are shown for reference, sections of these equations marked in red are extrapolated.

The currently defined critical clearances in the BRP busbar disconnector are lower than 1 m (see Table 2.1), so most previously defined equations and methods to determine the U_{50} and k_g cannot be deemed valid anymore. As the busbar disconnector skid has a complex geometry, an accurate gap factor cannot be retrieved from existing literature. Therefore, this work aims to define critical clearances and gap factors for the 110 kV BRP busbar disconnector.

3

Simulation of the gap factor

As Schneider and Weck [7] discussed, it is possible to determine the gap factor for gaps with a gap distance $d > 2$ m using the electric field and space potential distribution. They used an electrolytical tank to simulate these fields, but nowadays it is possible to determine these using FEM software. This method is also investigated by Terna, the Italian TSO [38]. To validate the measurements done in [7] and to extend those measurements to smaller gaps, several simulations are performed in COMSOL Multiphysics®.

3.1. Verification of the method of Schneider and Weck

This section reproduces the results of Schneider and Weck. First, the rod-plane gap is investigated, and then the conductor-rod and conductor-plane are considered. The electric field distribution is simulated and then used to determine the gap factor.

3.1.1. Rod - plane

The rod-plane gap, as used by [7], is shown in Figure 3.1. The same geometry is used for a 3D electric field simulation for several gap distances. The simulated electric field for a 0.5 m gap is shown in Figure 3.2. The gap factors are studied using the previously described model of Schneider and Weck. The results are listed in Table 3.1 and shown in Figure 3.3, where they are compared to the results from Schneider and Weck and to gap factors in literature [17].

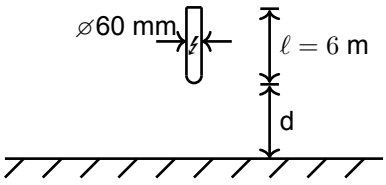

Figure 3.1: Rod-plane gap [7, Fig. 13a]

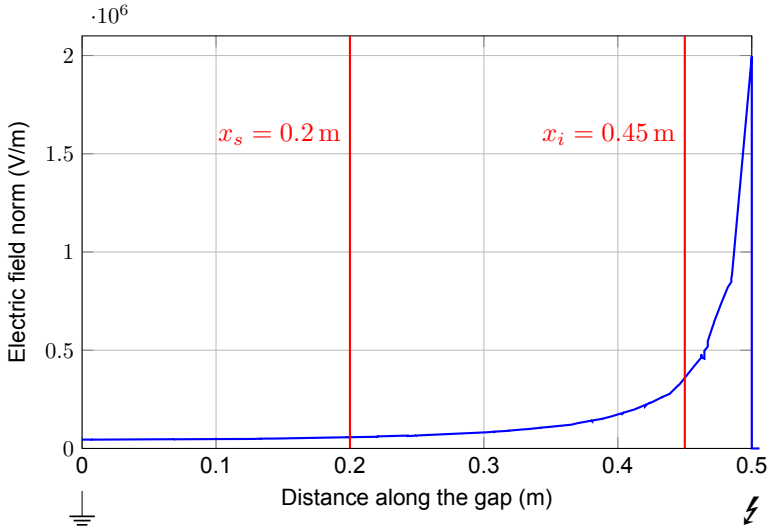

Figure 3.2: Electric field distribution of the 0.5 m rod-plane gap of Figure 3.1

Table 3.1: Results of the Schneider and Weck model for determining the gap factor of rod-plane gaps

Gap distance (m)	$\varphi(x_s)$ (V)	$\varphi(x_i)$ (V)	R (-)	k_g (-)
0.25	12331	48813	0.253	1.08
0.50	9788	40197	0.244	1.06
0.75	8613	35593	0.242	1.06
1	7875	37291	0.241	1.05
2	6363	26673	0.234	1.05
4	5139	21908	0.235	1.04
6	3977	18519	0.215	0.99

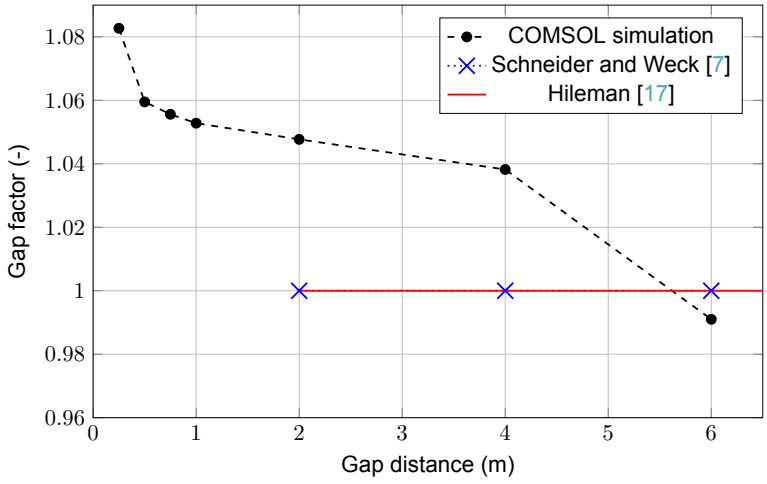

Figure 3.3: Comparison of simulated rod-plane gap factor with literature results

It can be concluded that, although the values from the simulation are relatively close to $k_g = 1$ from the literature, it does not represent the actual gap factor. By definition, the gap factor of the rod-plane gap is 1.0, as it is taken as a reference. Therefore, the other gap configurations have to be scaled according to the rod-plane gap factors found in Table 3.1. This normalisation is performed as follows:

$$k_{g,\text{normalised}} = \frac{k_{g,\text{from simulation}}}{k_{g,\text{rod-plane from simulation}}} \tag{3.1}$$

3.1.2. Conductor - rod

The second setup to be simulated is the conductor-rod geometry, shown in Figure 3.4 and simulated in 3D.

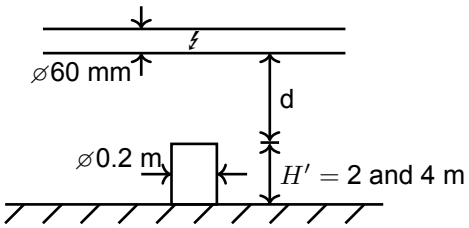

Figure 3.4: Conductor-rod gap [7, Fig. 13h]

The simulation for a gap distance of 0.5 m results in an electric field distribution as shown in Figure 3.5. Schneider and Weck introduce $x_s = 0.4d$ and $x_i = 0.9d$. This leads to $x_s = 0.2$ m and $x_i = 0.45$ m. The space potential at these locations is retrieved from the simulation, the ratio R is calculated using Equation 2.13 and the gap factor k_g is calculated using Equation 2.14. These parameters are shown in Table 3.2.

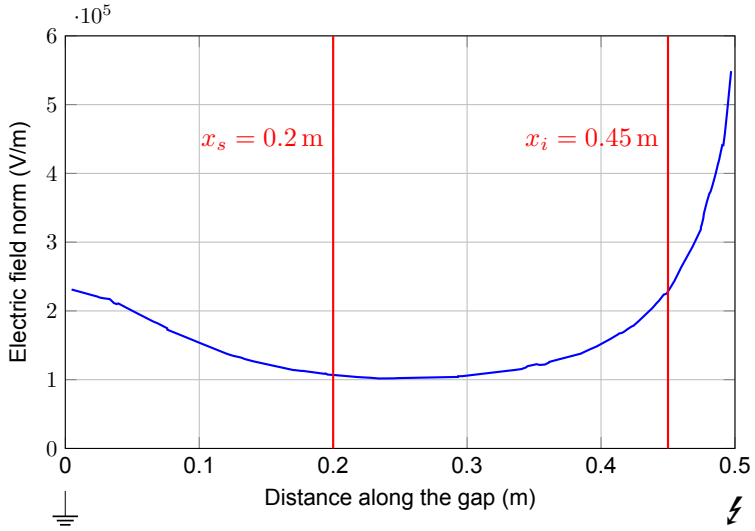

Figure 3.5: Electric field distribution of the 0.5 m conductor-rod gap of Figure 3.4 ($H' = 4$ m)

Table 3.2: Non-normalised results of the Schneider and Weck model for determining the gap factor of conductor-rod gaps

Gap distance (m)	$\varphi(x_s)$ (V)	$\varphi(x_i)$ (V)	R (-)	k_g (-)
0.25	33300	80811	0.412	1.46
0.50	33336	70422	0.473	1.61
0.75	32294	65512	0.493	1.65
1	31033	62223	0.499	1.67
2	26871	54827	0.490	1.65
4	22568	49313	0.458	1.57
6	14284	38958	0.367	1.35

Figure 3.6 shows that in the range $d > 2$ m (where both Hileman [17] and the model [7] are valid), the normalised simulation results are comparable with the literature results. The simulation results, however, show a sudden change in the gap factor between $0.25 < d < 1$ m. This could already indicate the invalidity of this method for small gap distances.

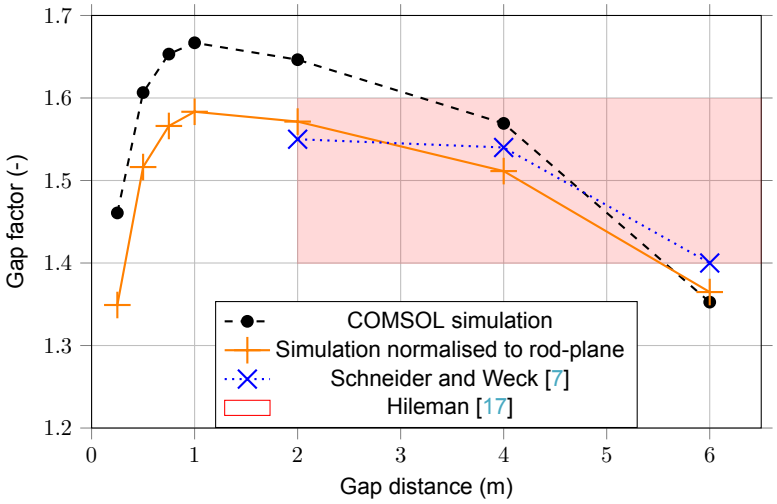

Figure 3.6: Conductor-rod gap factor ($H' = 4$ m)

3.1.3. Conductor - plane

The simulation was performed in 2D for the conductor-plane gap setup (shown in Figure 3.7). The electric field distribution is shown in Figure 3.8. The results are shown in Table 3.3 and Figure 3.9.

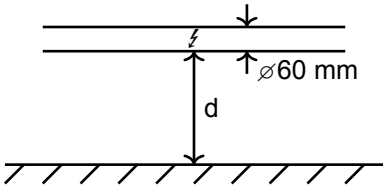

Figure 3.7: Conductor-plane gap [7, Fig. 13d]

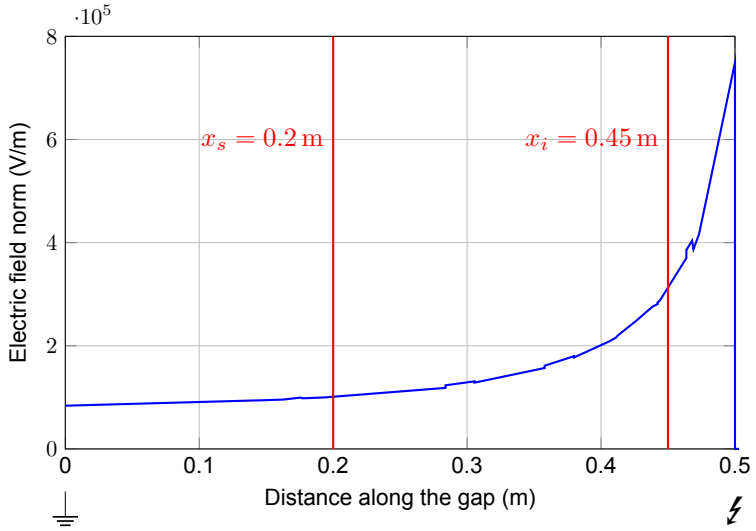

Figure 3.8: Electric field distribution of the 0.5 m conductor-plane gap of Figure 3.7

Table 3.3: Non-normalised results of the Schneider and Weck model for determining the gap factor of conductor-plane gaps

Gap distance (m)	$\varphi(x_s)$ (V)	$\varphi(x_i)$ (V)	R (-)	k_g (-)
0.25	21006	62671	0.335	1.28
0.50	18251	57633	0.317	1.23
0.75	16761	54477	0.308	1.21
1	15832	52192	0.303	1.20
2	14004	46994	0.298	1.19
4	12737	42786	0.298	1.19
6	12549	41335	0.304	1.20

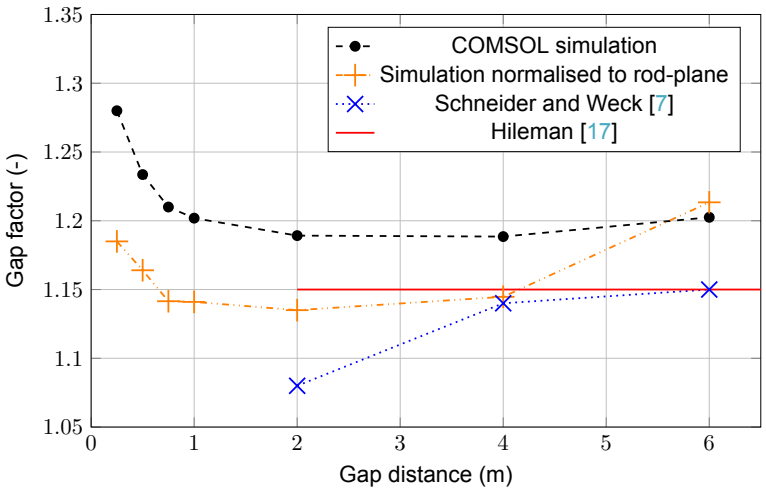

Figure 3.9: Conductor-plane gap factor

Figure 3.9 shows that the normalised gap factor aligns well with the literature. The discrepancy between the raw and the normalised results at $d = 6\ m$ is caused by the simulated rod-plane gap factor, which is smaller than 1. The normalised simulation results differ at most 5% from the results from Schneider and Weck.

Results for more gaps are listed in Table A.1.

3.1.4. Conclusion

The method of Schneider and Weck [7] in the electrolytical tank is verified with simulations in COMSOL Multiphysics®, showing a difference of at most 5%. The cause of this difference is likely due to the fact that Schneider and Weck used an electrolytical tank, resulting in a lower accuracy than COMSOL. As there is no comparison possible outside the validity range of literature [17] and outside of the validity range defined by Schneider and Weck, the validity outside this range remains uncertain.

3.2. Experimental gaps

This section deals with the simulation of gaps, used for experimental work in a later stage. The setups are simulated in a model of the high voltage laboratory, shown in Figure 3.10. The red dot marks the location where the setups are placed. This corresponds with the actual placement in the laboratory. The floor, walls and ceiling of the laboratory are grounded in this simulation.

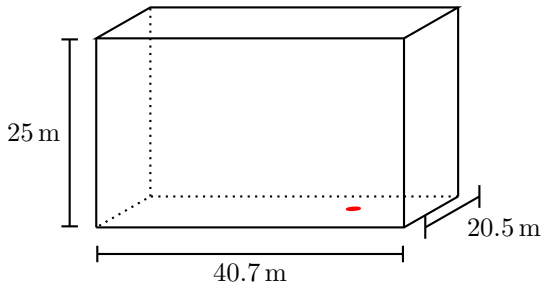

Figure 3.10: The modelled high voltage laboratory. Walls, floor and ceiling are grounded.

The results of this section will be used to compare with the experimental results of the following chapters.

3.2.1. Rod - plane

A rod-plane gap that can be constructed in the laboratory is shown in Figure 3.11. This geometry is placed in the modelled high voltage laboratory, and the electric field is studied to arrive at the gap factor, following the method of Schneider and Weck described earlier. The results are listed in Table 3.4.

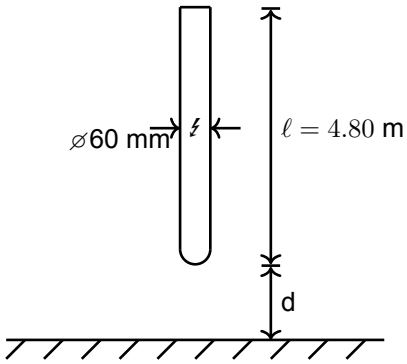

Figure 3.11: Rod-plane geometry

Table 3.4: Results of the Schneider and Weck model for determining the gap factor of realistic rod-plane gaps

Gap distance (m)	$\varphi(x_s)$ (V)	$\varphi(x_i)$ (V)	R (-)	k_g (-)
0.50	11959	49128	0.243	1.06
0.75	10459	43518	0.240	1.05
1	9530	39873	0.239	1.05

Table 3.4 shows that the simulated gap factor is around 1.05. This gap factor can be used to normalise the gap factor of the conductor-rod geometry, as explained in Section 3.1.1.

These results compare well with the results of Schneider and Weck (Section 3.1.1). The geometry is the same, except for the length of the rod. The dimensions of the laboratory are now included in the model, meaning that this has a negligible effect.

3.2.2. Conductor - rod

A conductor-rod geometry that can be constructed in the laboratory is shown in Figure 3.12. Its gap factors are again studied using the method of Schneider and Weck.

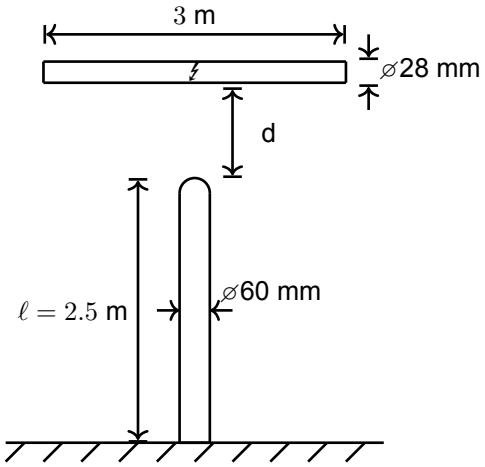

Figure 3.12: Conductor-rod geometry

This yielded the gap factors listed in Table 3.5. The gap factor normalised to the rod-plane gap factors is also shown.

Table 3.5: Results of the Schneider and Weck model for determining the gap factor of realistic conductor-rod gaps

Gap distance (m)	$\varphi(x_s)$ (V)	$\varphi(x_i)$ (V)	R (-)	k_g (-)	$k_{g,\text{normalised}}$ (-)
0.50	34310	69213	0.496	1.66	1.57
0.75	29343	63558	0.462	1.58	1.50
1	25537	59293	0.431	1.51	1.43

The normalised results are in the range Hileman mentions ($1.4 \leq k_g \leq 1.6$) [17]. The gap factors are slightly lower than the results from [7] (shown in Figure 3.6), due to the difference in geometry.

The results of these rod-plane and conductor-rod gaps will be verified using experimental results in the following chapter.

4

Experimental work on simple geometries

This chapter starts with an introduction and background on high voltage testing, after which a relatively simple geometry will be tested to validate the method of Schneider and Weck [7], namely the conductor-rod gap. Conductor-rod gaps are considered to be found during work in substations, for instance, while walking with a ladder, or while pointing with a screwdriver.

Gap factors are always taken with reference to the positive rod-plane gap (see Eq. 2.10) [23]. Therefore, the breakdown strength of rod-plane gaps has to be known before gap factors for different geometries can be studied. The gaps in this chapter will be studied at gap distances of $d = 0.5, 0.75$, and 1 m, for both positive and negative stresses.

4.1. Introduction to high voltage testing

This section describes the test setup, test methods and analysis of test results used for the experimental work.

4.1.1. Test setup

To perform impulse testing, an impulse generator is connected to the device under test, and a voltage divider is connected. The voltage is measured using an oscilloscope. A general test setup is shown in Figure 4.1.

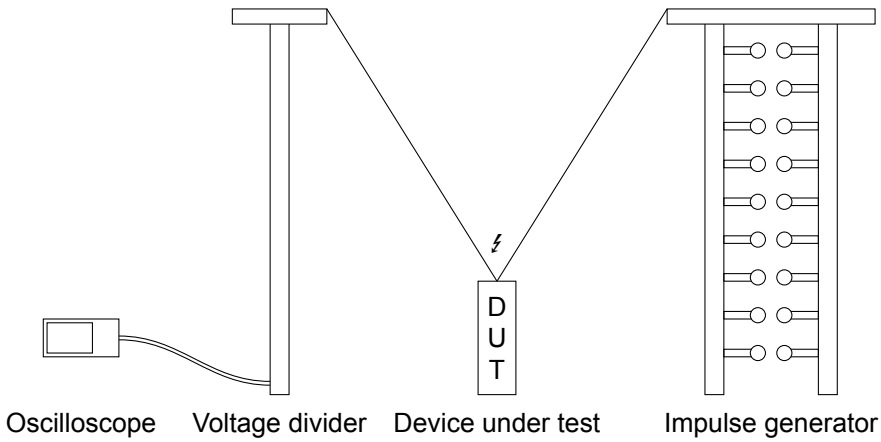

Figure 4.1: High voltage test setup

An impulse generator consists of several resistors and capacitors (see Figure 4.2). C_l represents the capacitance of the device under test (DUT), R_d the tail resistor, R_f the front resistor, R_{ch} the charging resistor and C_d the impulse capacitors. The combination of resistors and capacitors determines the wave parameters. For the gaps considered in this thesis, the critical time-to-crest is around 100 µs (see Sections 4.2, 4.4, and Chapter 5). The critical time-to-crest is used, as the worst-case scenario has to be considered when determining clearances. The critical time-to-crest gives rise to the lowest breakdown strength, and hence is the worst case. The time-to-half used should be close to the time-to-half of a standard switching impulse, which is 2500 µs [21]. Only a limited number of resistors are available to be used in the impulse generator, therefore it is not possible to generate all arbitrary waveforms.

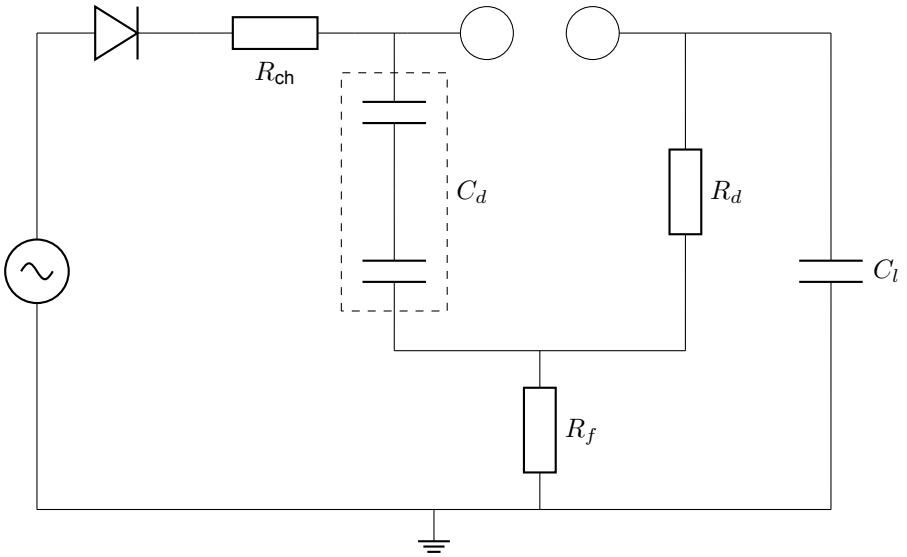

Figure 4.2: Equivalent circuit of the TU Delft impulse generator for switching impulses

To generate the desired T_{cr} and T_{tail}, the resistances are tuned as listed in Table 4.1. With these values and 5 stages of the impulse generator, the generated waveform will have $T_{cr} \approx 125$ µs and $T_{tail} \approx 2100$ µs.

Table 4.1: Impulse generator capacitance and resistances, per stage

C_d	0.5 µF
R_f	1.7 kΩ
R_d	5 kΩ

The DUT is connected to the impulse generator using a copper wire. The voltage divider is connected to the device under test via a copper band. It has a divider ratio of $1604 : 1$ V. A band is preferred over a wire to minimise self-inductance and measure the high-frequency wave without distortion. The low voltage side of the divider is connected to a measurement system via a coaxial cable. The voltage divider is an RC-divider, meaning that it consists of resistors and capacitors, as shown in Figure 4.3.

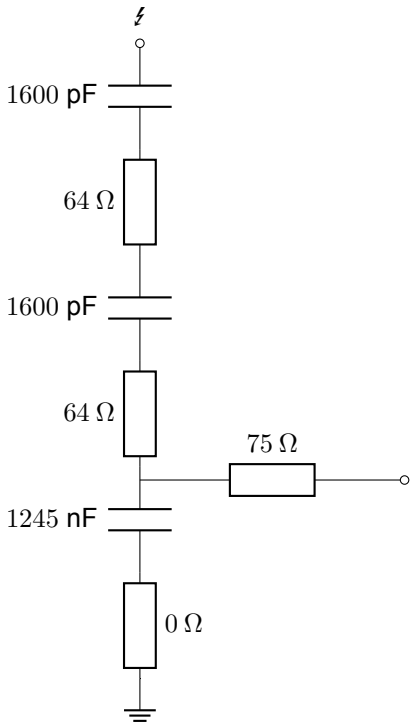

Figure 4.3: TU Delft RC voltage divider

The applied voltage is measured according to the IEC 60060-2 standard [39], stating that the peak value should be measured with an expanded uncertainty of $U_M \leq 3\%$. The time parameters (T_{cr} and T_{tail}) should be measured with an expanded uncertainty $U_M \leq 10\%$. The expanded uncertainty corresponds to a 95% confidence interval.

4.1.2. Test methods

Determining U_{50}

To determine the 50% withstand voltage, the up-and-down method specified in IEC 60060-1 [21] can be used. In this method, a number of $m \geq 15$ groups with $n = 1$ voltage stresses are applied at voltage levels U_i ($i = 1, 2, ..., l$). The applied voltage is increased by ΔU in case of a withstand, and decreased by the same ΔU in case of a breakdown. ΔU can be chosen as $\Delta U =$ (0.01 to 0.03)$U_{50,\text{expected}}$. The test sequence starts with the group k_i with the voltage level U_i, at which at least two groups of stresses have been applied. U_{50} is calculated as the arithmetic mean of all applied impulses during the test sequence, i.e. $\sum_{i=1}^{l}(k_i U_i)/m$. This method is shown in Figure 4.4a. From the figure, it can be seen that after every breakdown, the applied voltage decreases, and after every withstand, it increases by one level. Eventually, the mean converges to the U_{50}.

Determining U_{10}

To determine the breakdown probability U_p, a number of n gaps can be tested in parallel. This leads to a breakdown probability of $p = 1 - 0.5^{1/n}$, from which it follows that $n = \frac{\ln(0.5)}{\ln(1-p)}$, with $n \in \mathbb{Z}$. Instead of testing n gaps in parallel, the same result can be obtained by performing an up-and-down test with n voltage stresses per group. For $p = 0.1$, this leads to $n = 6.578 \rightarrow 7$ voltage stresses. If there were no breakdowns after $n = 7$ stresses, the applied voltage is increased by ΔU. If there was a breakdown, the applied voltage is immediately lowered by ΔU. ΔU can be chosen as $\Delta U =$ (0.01 to 0.03)U_{50}. The test sequence consists of l voltage levels U_i at which at least two groups of stresses k_i have been applied. U_{10} is approximated as the arithmetic mean of all applied groups during the test sequence, i.e. $\sum_{i=1}^{l}(k_i U_i)/m$. This method is shown in Figure 4.4b. From the figure, it can be seen that after every breakdown, the applied voltage decreases. After $n = 7$ withstands, the voltage increases by one level. Care has to be taken that it is not exactly U_{10} that is found, but $U_{9.427}$, as n is limited to be an integer value.

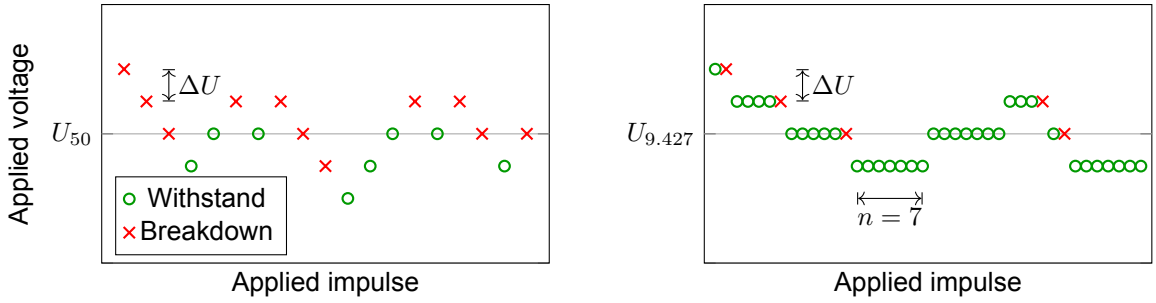

(a) Determination of U_{50}

(b) Approximation of U_{10}

Figure 4.4: Methods to determine 50% and 10% withstand voltages

Multiple-level method

Contrary to the up-and-down test, where the number of impulses per level n is varied to centre the voltage levels around the breakdown percentage of interest, the multiple-level method [21] does not centre around voltage levels. Instead, an invariant number of $n \geq 10$ impulses is applied at $m \geq 5$ voltage levels U_i (i=1, 2, ..., m), causing k_i breakdowns at voltage level U_i, with the difference between two adjacent voltage levels being $\Delta U = (0.01 \text{ to } 0.06)U_{50,\text{expected}}$. This method is shown in Figure 4.5a. The empirical breakdown probability $p_i = k_i/n_i$ at voltage level U_i can be used as an estimate of the breakdown probability $p(U_i)$. Fitting a normal distribution to all the m breakdown probabilities $p(U_i)$, the standard deviation σ, and a specific breakdown probability (e.g. U_{50} or U_{10}) can be determined.

Modified multiple-level method

The drawback of the multiple-level method is that it allows for a breakdown probability $p_i = 0$ and $p_i = 1$ (n out of n withstands or breakdowns). This does not provide information about the slope of the breakdown probability curve, or is not acceptable for some probability distributions. To overcome this drawback, a modified multiple-level method is introduced [40]. In this method, a minimum number of impulses is applied at each voltage level, but if the breakdown probability is very high or low (e.g. 1 or 0), the number of impulses is increased until, for example, 2 withstands or breakdowns occur at that voltage level. In other words: a minimum number of $n_i \geq 10$ impulses is applied at $m \geq 5$ voltage levels U_i ($i = 1, 2, ..., l$), causing k_i breakdowns at voltage level U_i. If $k_i \leq 2$ or $k_i \geq n_i - 2$, n_i is increased until $k_i = 2$ or $k_i = n_i - 2$. The difference between the voltage levels is the same as in the multiple-level method, $\Delta U = (0.01 \text{ to } 0.06)U_{50,\text{expected}}$. This method is shown in Figure 4.5b. A specific breakdown probability can be determined in the same way as for the multiple-level method, by fitting a normal distribution to the empirical breakdown probabilities.

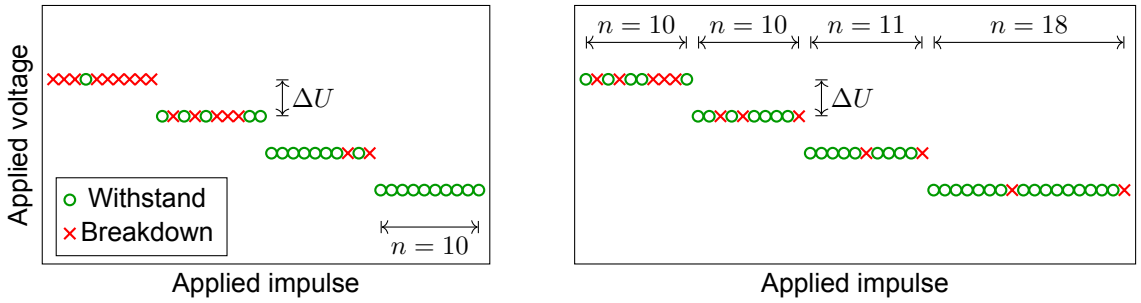

(a) Multiple-level method

(b) Modified multiple-level method

Figure 4.5: Multiple-level methods

4.1.3. Analysis of test results

The IEC up-and-down methods described above will give the sample mean ($\hat{U}_{50}$ for $n = 1$, and $\hat{U}_{9.427}$ for $n = 7$). However, this estimate is based solely on the observed test sequence, rather than the underlying statistical behaviour. To obtain estimates of the population parameters, the maximum likeli-

hood method can be used [41].
The principle of this method is to determine the statistical parameters that fit the observed breakdown data best. The flashover behaviour under a limited number of impulses can be described by a binomial distribution: the probability $f(x_i)$ of observing x_i flashovers in n_i applications at the i^{th} voltage level V_i is:

$$f(x_i) = \frac{n_i!}{x_i!(n_i - x_i)!} p_i^{x_i} (1 - p_i)^{n_i - x_i} \tag{4.1}$$

where p_i is the true probability of flashover at voltage level V_i and is a function of two parameters, the population mean U_{50} and standard deviation σ. The functions describes the flashover probability as a function of the applied voltage.
As flashovers, in general, are independent events, the likelihood of observing the complete test sequence is given as

$$L = \prod_{i=1}^{N} f(x_i) \tag{4.2}$$

The maximum likelihood estimates of U_{50} and σ are obtained by equating the partial derivatives of the likelihood function to zero: $\frac{\partial L}{\partial U_{50}} = \frac{\partial L}{\partial \sigma} = 0$. In practice, it is more convenient to maximise the logarithm of the likelihood function, leading to the equation to solve:

$$\frac{\partial \ln(L)}{\partial U_{50}} = \frac{\partial \ln(L)}{\partial \sigma} = 0 \tag{4.3}$$

The found U_{50} and σ represent the population from which the samples were taken best. The MATLAB function `binofit` [42] returns the two parameters and the 95% confidence intervals using the Clopper-Pearson method [43].

An estimation of the population mean, U_{50}, is the sample mean, $\hat{U}_{50}$. A typical value of σ that can be used as a start estimator is $\hat{\sigma} = 0.05\hat{U}_{50} = 5\%$ [41].

4.1.4. Atmospheric correction

The breakdown strength of an air gap highly depends on the atmospheric conditions during testing [21], [44]. To compensate for this behaviour, the results are corrected to reference atmospheric conditions:

- Temperature: $t_0 = 20\,^{\circ}\text{C}$
- Absolute pressure: $p_0 = 1013$ hPa
- Absolute humidity: $h_0 = 11$ g/m^3

The experimentally found voltage can be corrected to the reference conditions as follows [21]:

$$U_0 = U/(k_1 k_2) \tag{4.4}$$

The parameters k_1 and k_2 are obtained using the following equations:

$$k_1 = \delta^m \tag{4.5}$$

$$k_2 = k^w \tag{4.6}$$

where δ and k are found as follows:

$$\delta = \frac{p}{p_0} \times \frac{273 + t_0}{273 + t} \tag{4.7}$$

$$k = 1 + 0.010(h/\delta - 11) \text{ for impulse stresses and } 1 < h/\delta < 20 \text{ g/m}^3 \tag{4.8}$$

Exponents m and w are obtained using Table 4.2, where g:

$$g = \frac{U_{50}}{500 L \delta k} \tag{4.9}$$

where:

- U_{50} is the (anticipated) 50% breakdown voltage, at actual atmospheric conditions
- L is the minimum gap distance

Table 4.2: Exponents m and w

g	m	w
< 0.2	0	0
0.2 to 1.0	$g(g-0.2)/0.8$	$g(g-0.2)/0.8$
1.0 to 1.2	1.0	1.0
1.2 to 2	1.0	$(2.2-g)(2.0-g)/0.8$
>2.0	1.0	0

The above-mentioned method gives an error less than 2% for $2 < h/\delta < 11$ g/m^3 (rod-plane) and provides accurate values for sphere-plane gaps for $1 < h/\delta < 11$ g/m^3. This was tested for rod-plane and sphere-plane gaps of 0.60, 1, and 2 m [45].
The voltages mentioned in this thesis are corrected to reference atmospheric conditions.

4.2. Rod - plane gap

The rod-plane geometry is considered first, as its 50% withstand voltage is used as a reference for the gap factor [23]. Another reason for investigating this geometry, is that there is a large spread between the 4 equations (Paris, Feser, CRIEPI, and Gallet) describing the breakdown strength of a rod-plane gap (see Figure 2.7).

4.2.1. Geometry

The rod-plane setup is defined as follows:

- Diameter rod: 6 cm (smaller than the critical diameter of 7.2 cm, see Sec. 2.4), with a hemispherical tip
- Length rod: 4.80 m
- Ground plane: 2 metal sheets of 2x1 m and 1 sheet of 2.25x1 m

This is graphically shown in Figures 4.6a and 4.6b.

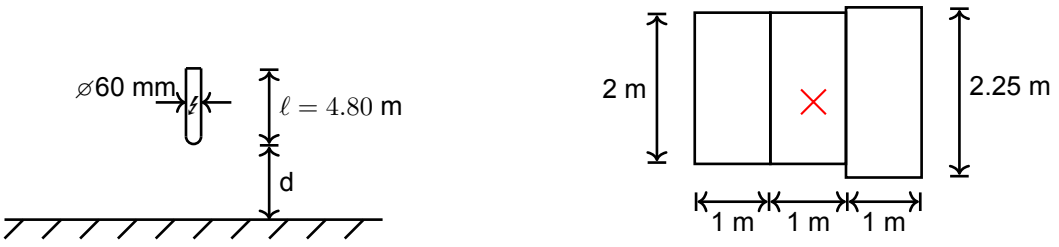

(a) Rod-plane geometry used for testing

(b) Ground plane with the projection of the rod indicated

Figure 4.6: Rod-plane test setup

The laboratory setup is shown in Figure 4.7.

Figure 4.7: Rod-plane geometry in the laboratory

4.2.2. Test execution

An up-and-down test with $n = 1$ was executed with the impulse generator, generating a waveform of $T_{cr} \approx 125$ µs and $T_{tail} \approx 2100$ µs. This T_{cr} is close to the critical time-to-crest for this gap (see in Figure 2.6 the Takeyama and T.U. Munich results) [23], [30]. The continuous mechanical ventilation in the laboratory caused noticeable movement of the rod during the tests. This will have caused an effect on the results, as the gap distance was not the same during multiple impulses. However, as more impulses were applied, this effect would naturally decrease, as the rod was moving back and forth.

Figure 4.8: Breakdown of the rod-plane gap

4.2.3. Results

The experimental results were analysed using the maximum likelihood (ML) method, leading to the results listed in Table 4.3. The full test results are reported in Appendix B.

Table 4.3: Rod-plane results, with 95% confidence intervals

Gap distance and polarity	U_{50} (kV)	σ (kV)	σ/U_{50} (%)	# impulses
0.5 m +	279 ± 2	6 ± 4	2.2 ± 1.4	32
0.5 m -	637 ± 10	33 ± 21	5.2 ± 3.3	52
0.75 m +	381 ± 2	5 ± 3	1.3 ± 0.8	37
0.75 m -	859 ± 5	15 ± 10	1.8 ± 1.2	41
1 m +	488 ± 7	20 ± 14	4.1 ± 2.9	49
1 m -	1082 ± 19	44 ± 30	4.1 ± 2.8	37

Figure 4.9 compares the results for the positive rod-plane gap with the equations introduced in Section 2.3. Although the applied impulse has a T_{cr} close to critical [23], the experimental results are not very close to the Gallet and CRIEPI equations. This could be because these equations are fitted for a larger domain ($1 < d < 21$ m and $0.5 < d < 12$ m, respectively). The Feser equation is fitted on a smaller domain ($0.4 \leq d \leq 3$ m), and is therefore more tailored to smaller gap distances.

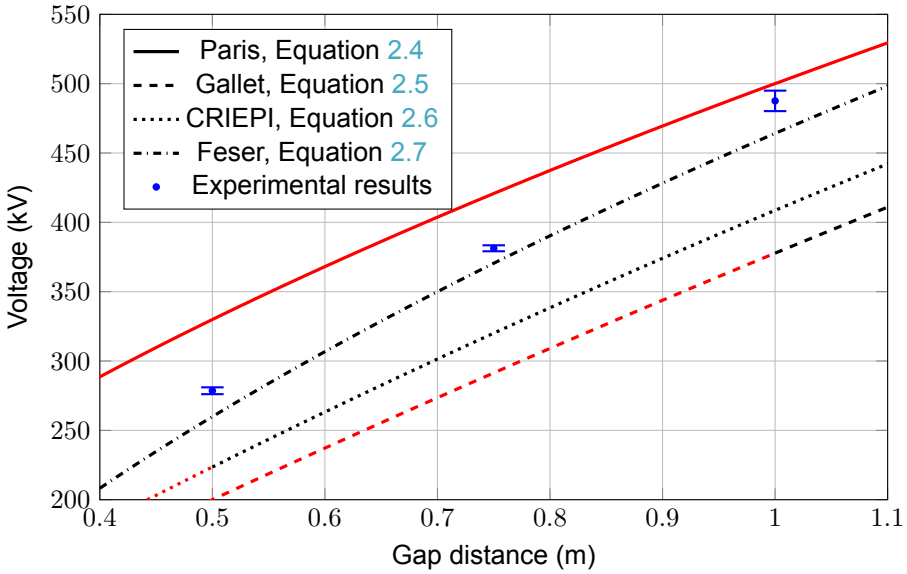

Figure 4.9: Rod-plane results with 95% confidence intervals for positive stresses compared to the U_{50} equations. Extrapolation of the breakdown equations outside their validity range is shown in red.

Figure 4.10 shows the results for negative impulses, together with Equation 2.8. This equation is only valid for $d > 2$ m. The experimental results show, however, that as the gap distance approaches 2 m, the experimental results approach Equation 2.8.

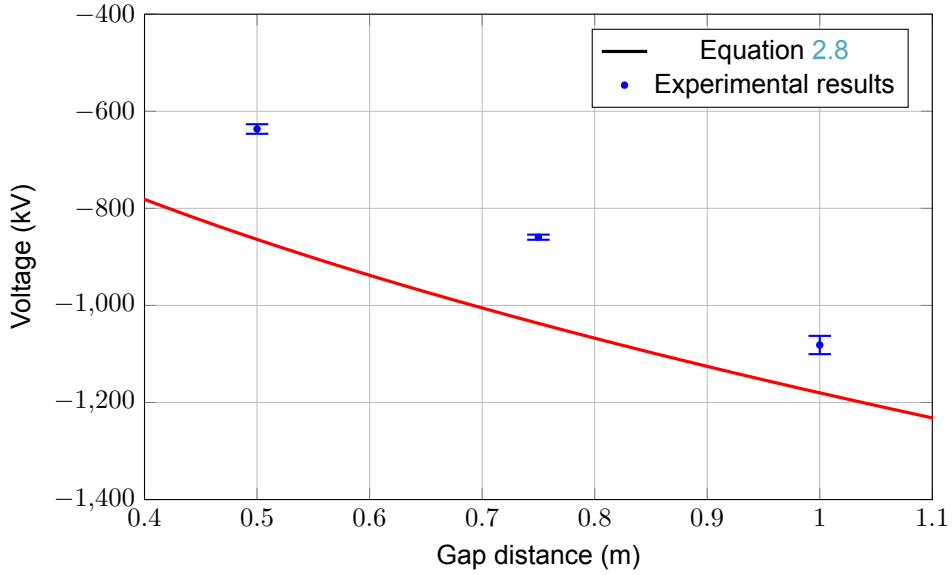

Figure 4.10: Rod-plane results with 95% confidence intervals for negative stresses. Extrapolation of the breakdown equations outside their validity range is shown in red.

4.2.4. Discussion

Comparison with literature

The results for the positive 0.5 m, 0.75 m, and both positive and negative 1 m gaps are in line with the results in [36] (see Table 4.4 and Figure 4.11), considering that the setup and waveshapes are not the same. For the other distances and polarities, [36] does not provide a reference value.

Table 4.4: Comparison of experimental results with literature

Gap distance and polarity	U_{50} experimental (kV)	U_{50} (kV) [36]
0.5 m +	279 ± 2	259
0.75 m +	381 ± 2	341
1 m +	488 ± 7	481
1 m -	1082 ± 19	1074

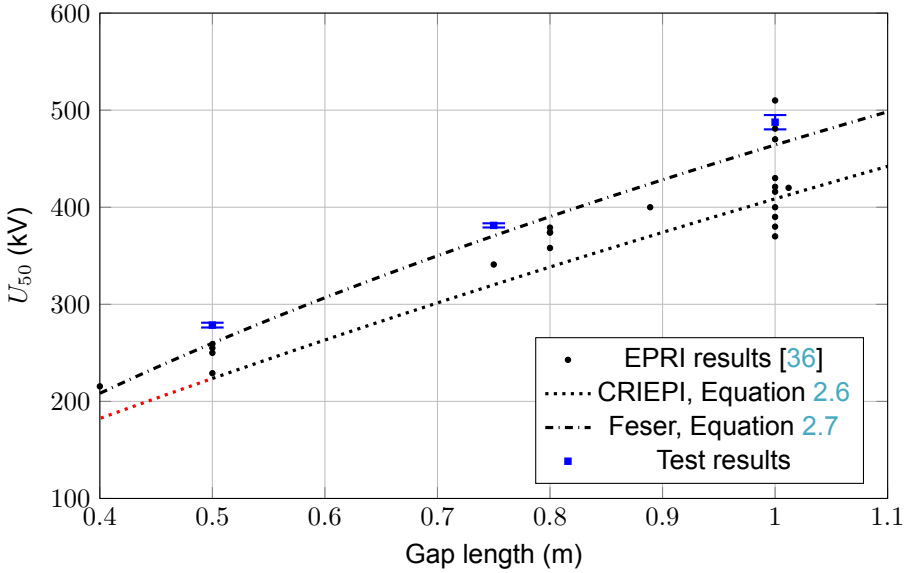

Figure 4.11: Literature results compared with test results. The CRIEPI and Feser equation are shown for reference, sections of these equations marked in red are extrapolated.

Corona discharges

When applying impulses to the rod, for some measurements, a sudden voltage drop was observed in the measured waveform, for both withstands and breakdowns. This was mainly visible for positive impulses on 0.5 m gaps. The measurement of the applied voltage and a zoom on the voltage drop are shown in Figure 4.12.

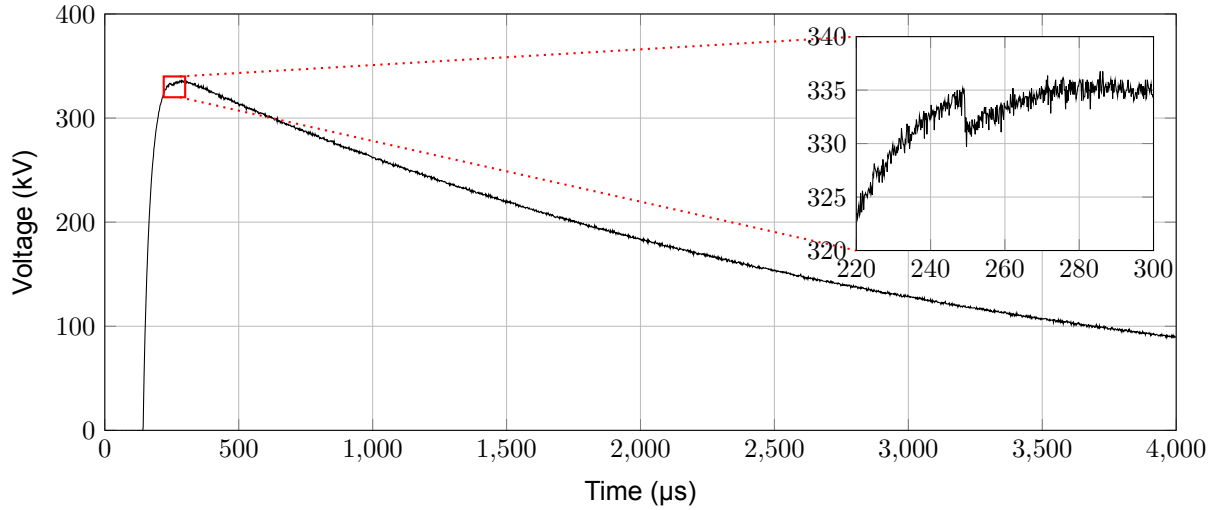

Figure 4.12: Measurement of applied impulse to the 50 cm rod-plane gap, showing a sudden drop in voltage

To ensure this was due to the rod-plane geometry, and not to the impulse generation and measurement setup, impulses were applied directly to the voltage divider, without the rod being connected. This yielded a smooth waveform, without a voltage drop. Then, the rod was sanded and polished once again to remove any leftover imperfections. After this, the voltage drops decreased, but did not disappear completely. This phenomenon could be caused by corona discharges, as they will give rise to a pre-discharge [46], which could cause a voltage drop over the front resistor of the impulse generator. This pre-discharge current is usually in the range of 2.5 A [47], and with a front resistor of 1.7 kΩ, it would lead to a voltage drop of 4.25 kV, which is comparable with the voltage drop in the waveform shown

in Figure 4.12. To test this hypothesis, the laboratory was made completely dark, and pictures were taken while applying impulses with a voltage slightly below U_{50}. A picture of a positive applied impulse is shown in Figure 4.13a. Negative applied impulses also led to corona on the rod, which is shown in Figure 4.13b. The humidity in the laboratory was higher when taking the pictures in Figure 4.13 than the moment when the waveform in Figure 4.12 was collected, and the measured waveforms related to Figure 4.13 show a smaller voltage drop. This can be explained by the fact that air has a higher dielectric strength at increased humidity, leading to reduced corona activity [21], [44], [45].

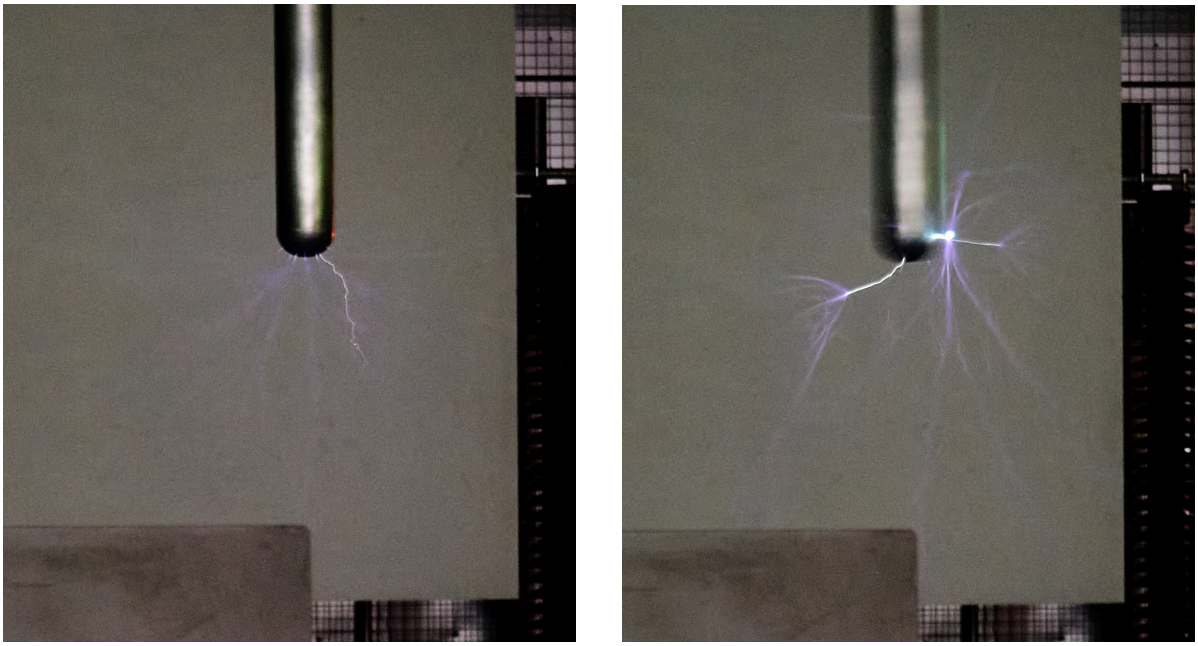

(a) Positive corona **(b)** Negative corona

Figure 4.13: Positive and negative corona on the 1 m rod-plane gap

Characteristics of the flashover strength

Feser [27] reported on breakdown behaviour of rod-plane gaps, indicating that the rod shape has a great influence on the distribution of the breakdown probability. A rod with a 30° point shows a breakdown distribution that is represented well by a normal distribution, whereas a rod with a 2 cm hemisphere shows non-normal behaviour. The results of Feser are shown in Figure 4.14.

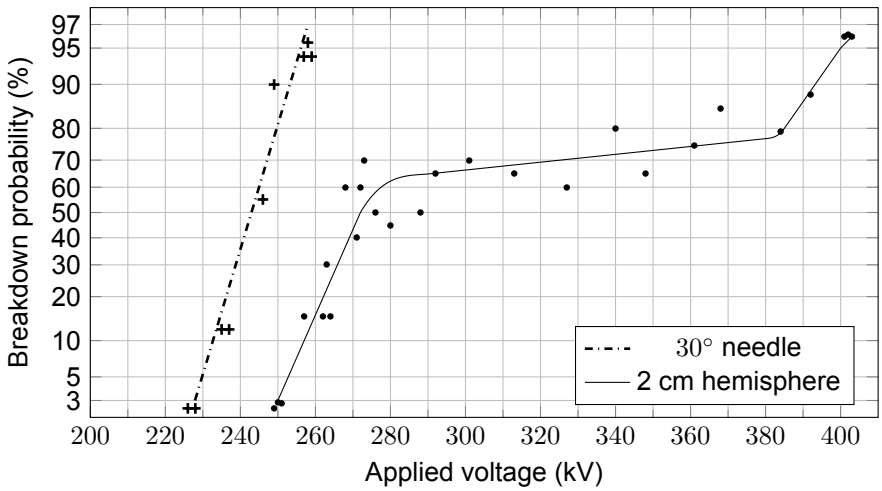

Figure 4.14: Results of Feser [27]. The 2 cm hemisphere shows a non-normal flashover distribution.

The measured breakdown probabilities for a gap distance of 0.75 m could indicate a non-normal distribution, as can be seen from Figure 4.15, where the empirical breakdown probabilities are shown, together with their 95% confidence intervals and the maximum likelihood (ML) fit. Specifically, the flattened probabilities at $U = -851$ kV, -858 kV, and -866 kV indicate non-normality. A total of 41 impulses were applied, of which 26 were at the three aforementioned voltage levels.

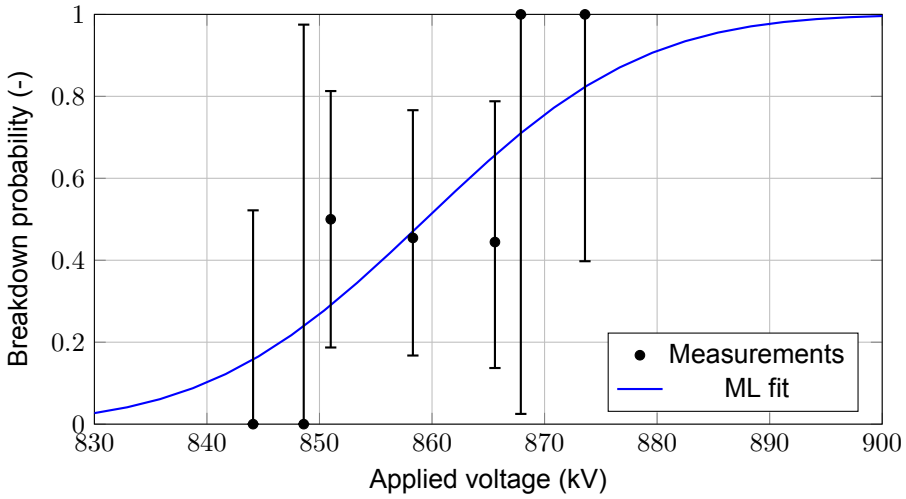

Figure 4.15: Breakdown probabilities with 95% confidence intervals and ML fit of the negatively stressed 0.75 m rod-plane gap

The non-normality of the empirical breakdown probabilities could be due to competing breakdown phenomena, streamer versus leader [27]. This can be shown by plotting the time-to-breakdown, as streamers give rise to a shorter time-to-breakdown than leaders [48]. If there are two distinct groups visible, it could indicate such a difference. Figure 4.16 shows this time-to-breakdown.

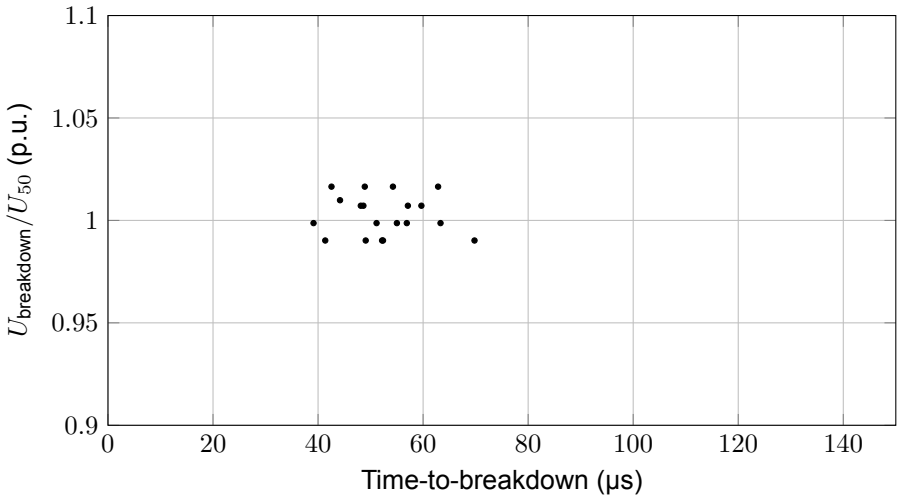

Figure 4.16: Time-to-breakdown of the 0.75 m rod-plane gap under negative stresses

Figure 4.16 does not show a clear distinction between two groups in the time-to-breakdown, so the hypothesis that there are multiple competing breakdown mechanisms can not be proven just from this data. This is also supported by the minimum and maximum E-field values obtained from a COMSOL simulation of this setup. For a streamer to start, the E-field must be at least 2.6 kV/mm [47]. To maintain a positive streamer, the E-field must be at least 0.45 kV/mm, for negative streamers this is 1 kV/mm [34]. A leader can be sustained if the E-field is at least 0.1 kV/mm [47]. The minimum and maximum E-fields from simulation are listed in Table 4.5.

Table 4.5: E-field values from COMSOL simulation

Gap distance and polarity	Min. E-field (kV/mm)	Max. E-field (kV/mm)
0.5 m +	0.154	7.226
0.5 m -	0.351	16.512
0.75 m +	0.124	9.422
0.75 m -	0.279	21.236
1 m +	0.107	11.459
1 m -	0.237	25.417

From Table 4.5, it can be seen that the E-field in all configurations is high enough to start a streamer discharge, but that the E-field is not high enough to sustain a streamer breakdown. The field is high enough for a leader breakdown. Therefore, the plateau between 850 and 866 kV is purely due to the statistical nature of the breakdown process. This is confirmed by Figure 4.15, as the normal distribution crosses through all the confidence intervals.

Figure 4.17 shows the time-to-breakdown of all gap distances for both positive and negative polarity.

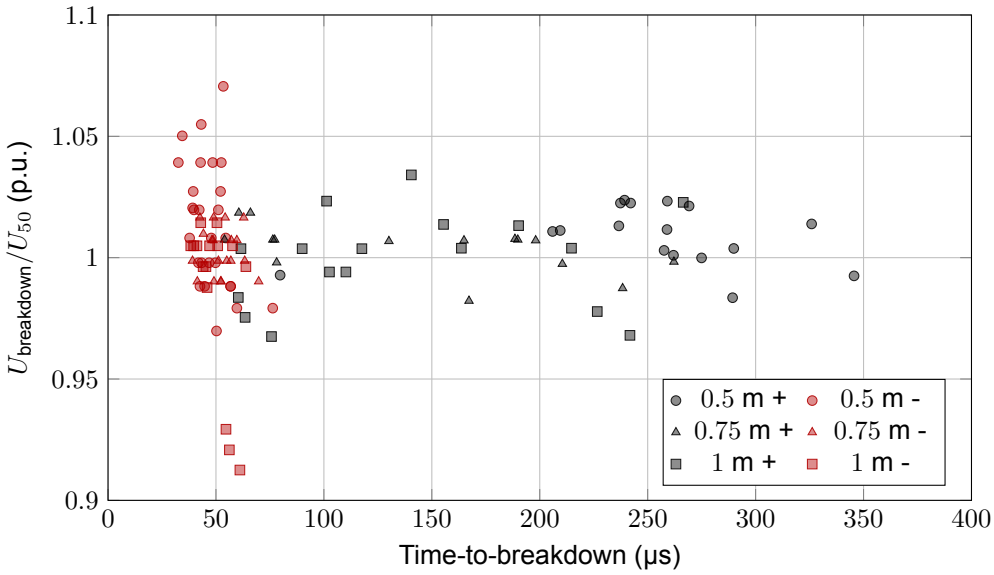

Figure 4.17: Time-to-breakdown of all gaps under positive and negative stresses

It can be seen that the time-to-breakdown for negative stresses is noticeably lower than for positive stresses. All negative breakdowns take place at the front of the impulse, whereas for positive stresses, there is a larger spreading in time-to-breakdown. For a rod-plane geometry, positive leaders progress continuously and slowly, while negative leaders progress in a stepped and rapid manner due to the higher voltage stress applied [49].

Another deduction that can be made from this graph is that for the negative polarity impulses, the T_{cr} was lower than the critical time-to-crest, as all the breakdowns happen before the crest of the impulse [30]. For the positive polarity impulses, the breakdowns were not exclusively on the front or tail. They were mostly confined to the tail, which indicates a T_{cr} slightly above the critical time-to-crest [30].

4.3. Needle - plane gap

To verify the critical radius of a rod-plane gap (see Sec. 2.4), the gap strength of several needle-plane gaps was tested. These tests are only performed with positive impulses, as these are used for the gap factor determination.

4.3.1. Geometry

Two geometries are considered, one rod with a blunt tip and one with a hemispherical tip. The total rod is composed of two parts, a long, thick rod and a short, narrow rod:

- Upper rod with a length of 1.34 m and a diameter of 50 mm connected to a:
  - Hemispherical-tipped rod with a length of 56 cm and a diameter of 8 mm, as shown in Figure 4.18a, or to a:
  - Blunt-tipped lower rod with a length of 45 cm and a diameter of 10 mm, as shown in Figure 4.18b.
- The plane consists of 1 conductive, grounded sheet of 2×1 m.

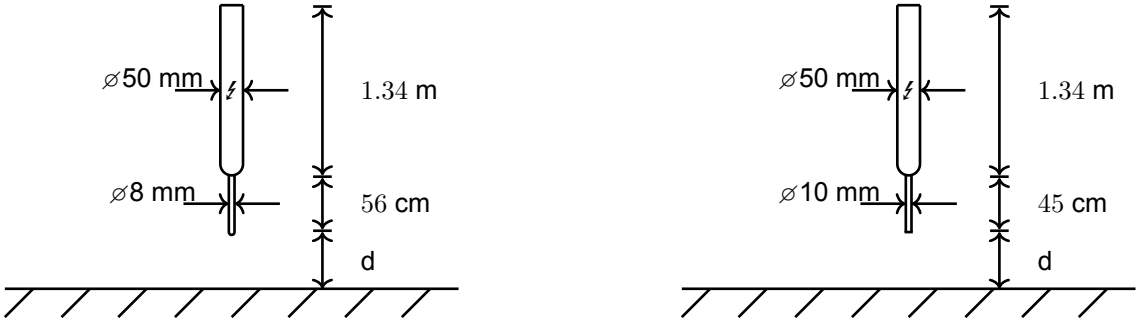

(a) Hemispherically tipped needle-plane **(b)** Blunt-tipped needle-plane

Figure 4.18: Needle-plane test setups

4.3.2. Test execution

An up-and-down test with $n = 1$ was executed using the impulse generator, generating a waveform of $T_{cr} \approx 127$ µs and $T_{tail} \approx 2103$ µs. This is close to the critical time-to-crest for this gap [23], [30]. The mechanical ventilation in the laboratory caused the rod to move. To dampen this movement, the upper side of the rod was attached with a rope to three points on the floor. The blunt rod was tested for gap distances of $d = 0.5$ and 0.75 m. The hemispherical rod was tested for a gap distance of $d = 0.5$ m to serve as a comparison only.

Figure 4.19: Breakdown of the needle-plane gap

4.3.3. Results

Table 4.6 lists the results of these tests. The full test results are listed in Appendix B.

Table 4.6: Needle-plane results, with 95% confidence intervals

Gap and polarity	U_{50} (kV)	σ (kV)	σ/U_{50} (%)	# impulses
Blunt rod 0.5 m +	256 ± 1	3 ± 1	1.2 ± 0.4	42
Hemispherical rod 0.5 m +	257 ± 1	4 ± 2	1.6 ± 0.8	51
Blunt rod 0.75 m +	352 ± 3	10 ± 5	2.8 ± 1.4	70

The breakdown voltages for the blunt and hemispherical rods at 0.5 m are nearly the same, and have overlapping 95% confidence intervals, indicating no statistical difference.

4.3.4. Discussion

Comparison with ⌀6 cm rod

In Table 4.7 and Figure 4.20, the ⌀6 cm rod of Section 4.2 is compared with the ⌀1 cm blunt rod.

Table 4.7: Comparison of the U_{50} for ⌀6 cm and ⌀1 cm rods

Gap distance and polarity	U_{50} ⌀6 cm rod	U_{50} ⌀1 cm rod
0.5 m +	279 ± 2	256 ± 1
0.75 m +	381 ± 2	352 ± 3

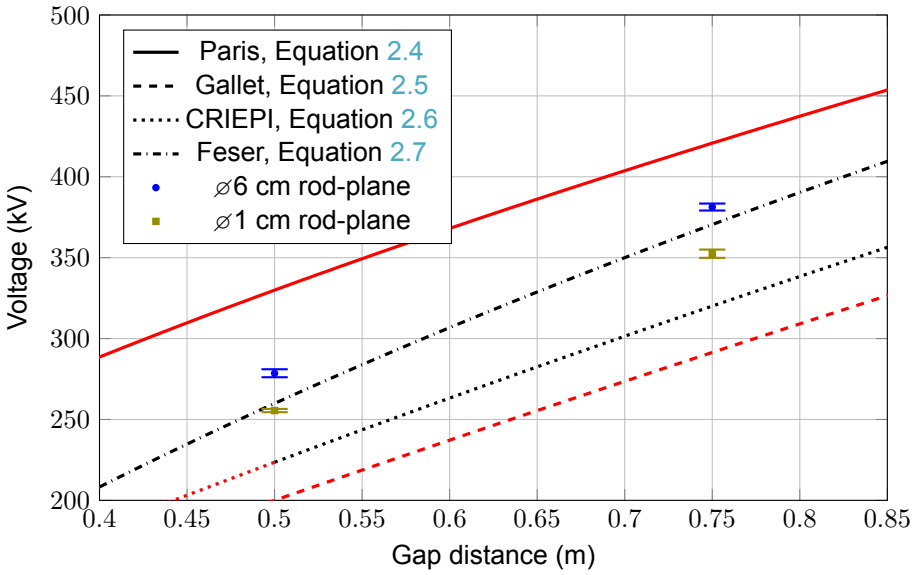

Figure 4.20: Rod-plane and needle-plane results with 95% confidence intervals for positive stresses. Extrapolation of the breakdown equations outside their validity range is shown in red.

It can be seen that, as for the ⌀6 cm rod (from Sec. 4.2), the experimental results are the best represented by the Feser equation (Eq. 2.7). The same explanation holds, namely that this equation is specifically tailored to small gaps, whereas the Paris, Gallet, and CRIEPI equations are developed to represent a large range of gap lengths. For determining clearances, the use of the CRIEPI equation is preferred, as it consistently underestimates the strength of the rod-plane gap. This is to overcome the differences in test results between different high voltage laboratories ($\sim 5\%$) and still be on the conservative side.

There is a noticeable difference in U_{50} between the two geometries. This contradicts the concept of the critical radius (Sec. 2.4), which states that below a certain rod radius, the breakdown strength is not

affected by the radius of the rod. For both rods, the diameter is below critical (7.2 cm according to Eq. 2.9). The results of both rods are shown in 4.21.

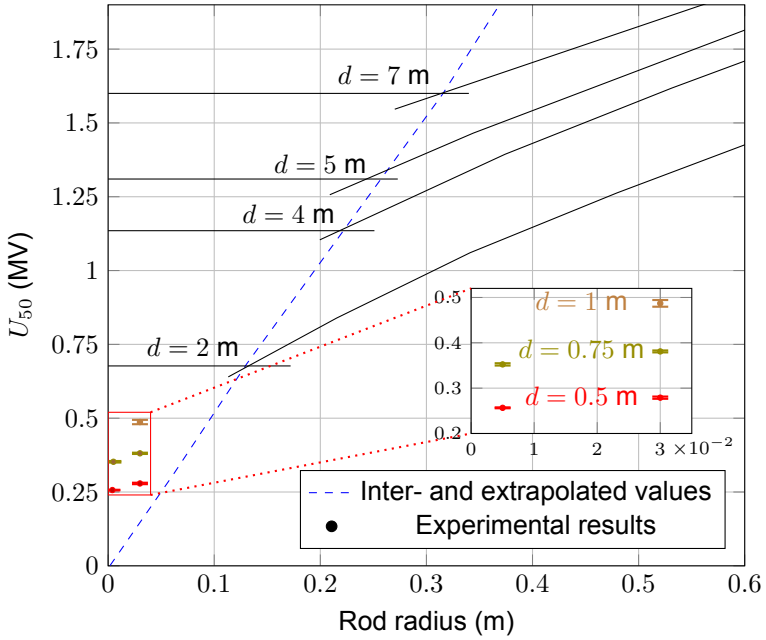

Figure 4.21: Critical radii from [29], with a zoom on experimental results. Error bars indicate 95% confidence intervals.

A possible explanation is that the critical radius in literature is based on long gaps ($2 \leq d \leq 7$ m in [29] and $3 \leq d \leq 10$ m in [31]). Extrapolating these findings can yield incorrect critical radii.

Comparison with literature

The results of these tests are compared with the EPRI report on short gaps [36] in Table 4.8 and Figure 4.22.

Table 4.8: Comparison of experimental results with literature

Gap distance and polarity	U_{50} experimental (kV)	U_{50} (kV) [36]
0.5 m +	256 ± 1	259
0.75 m +	352 ± 3	341

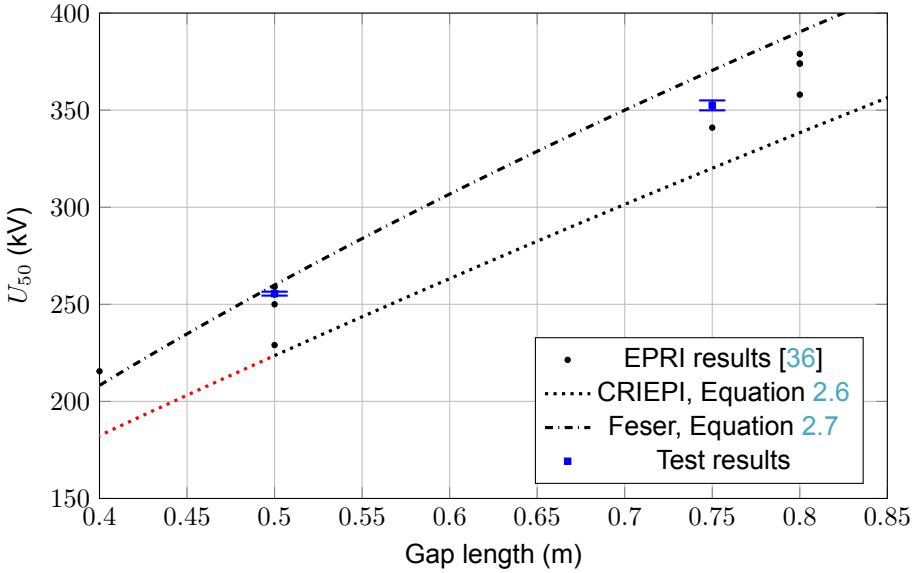

Figure 4.22: Literature results compared with test results. The CRIEPI and Feser equation are shown for reference, sections of these equations marked in red are extrapolated.

The experimental results are comparable to and lie in the same range as the results from the literature. The results of this the needle-plane test are closer to the reference value from literature than the results of the rod-plane test (see Table 4.4).

4.4. Conductor - rod gap

A conductor-rod gap is of interest, as it is a common gap to be observed when work is performed in a substation [33]. As the standard deviation of conductor-rod gaps is not well-defined in literature, in addition to the U_{50}, the U_{10} will be determined as well.

4.4.1. Geometry

The conductor-rod geometry has the following setup:

- Diameter rod: 6 cm, with hemispherical tip
- Length rod: 2.5 m
- Length conductor: 3 m
- Diameter conductor: 2.8 cm

The setup is shown in Figure 4.23.

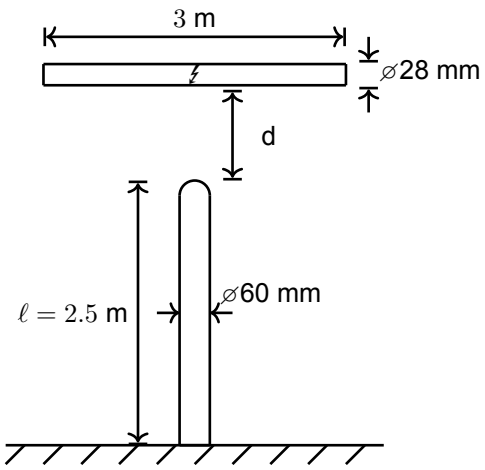

Figure 4.23: Measurement setup

The laboratory setup is shown in Figure 4.24.

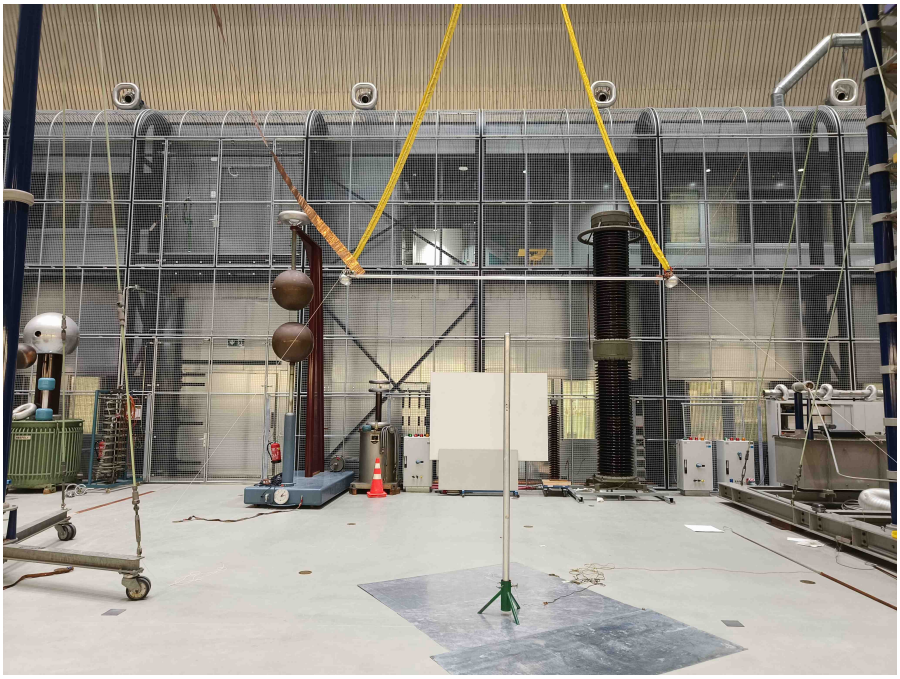

Figure 4.24: Conductor-rod in the laboratory

4.4.2. Test execution

The test was executed with the impulse generator, generating a waveform of $T_{cr} \approx 125$ µs and $T_{tail} \approx 2100$ µs. This T_{cr} represents the critical time-to-crest for a slightly different conductor-rod gap [37]. The continuous mechanical ventilation in the laboratory caused noticeable movement of the conductor during the tests. To prevent discharges from the ends of the conductor, corona spheres were applied at both ends. First, an up-and-down test with $n = 1$ was performed to determine U_{50}, and subsequently an up-and-down test with $n = 7$ was performed to determine $U_{9.427}$.

4.4.3. Results

The measurements from the U_{50} and $U_{9.427}$ tests were analysed together using the maximum likelihood method. The results of these tests are shown in Table 4.9 and Figures 4.26 and 4.27. The full test results are listed in Appendix B.

Figure 4.25: Breakdown of the conductor-rod gap

Table 4.9: Conductor-rod results, with 95% confidence intervals

Gap	U_{50} (kV)	U_{10} (kV)	σ (kV)	σ/U_{50} (%)	# impulses
0.5 m +	372 ± 1	365 ± 2	5 ± 1	1.3 ± 0.3	138
0.5 m -	343 ± 5	324 ± 4	15 ± 5	4.4 ± 1.5	141
0.75 m +	513 ± 8	469 ± 11	34 ± 10	6.6 ± 2.0	136
0.75 m -	461 ± 5	443 ± 5	14 ± 5	3.0 ± 1.1	104
1 m +	660 ± 12	617 ± 10	34 ± 12	5.2 ± 1.8	138
1 m -	609 ± 3	597 ± 2	10 ± 3	1.6 ± 0.5	230

It can be seen that between the U_{50} and U_{10} for positive impulses at $d = 0.5$ m, there is as little difference as 7 kV, leading to $\sigma = 1\%$. The 95% confidence intervals, however, do not overlap, indicating that these values are statistically different.

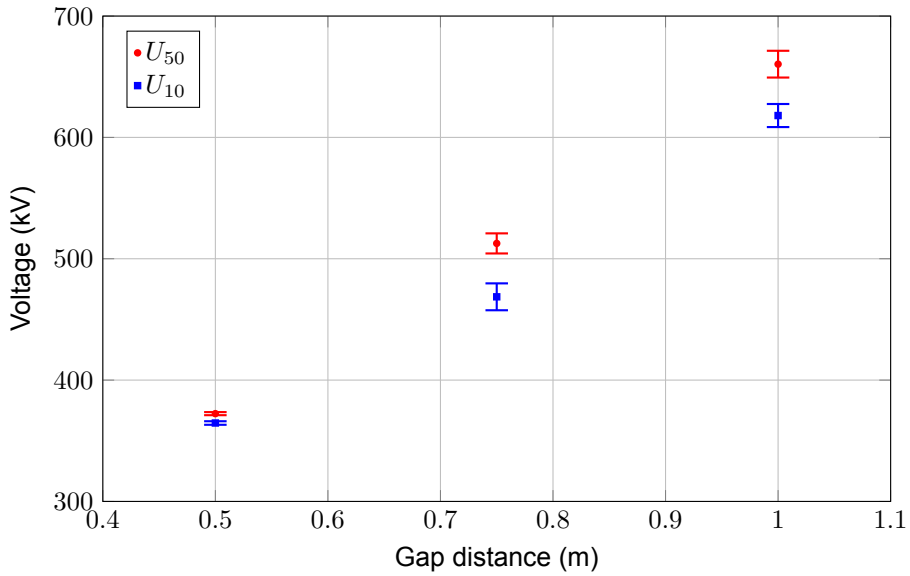

Figure 4.26: Conductor-rod U_{50} and U_{10} with 95% confidence intervals for positive impulses

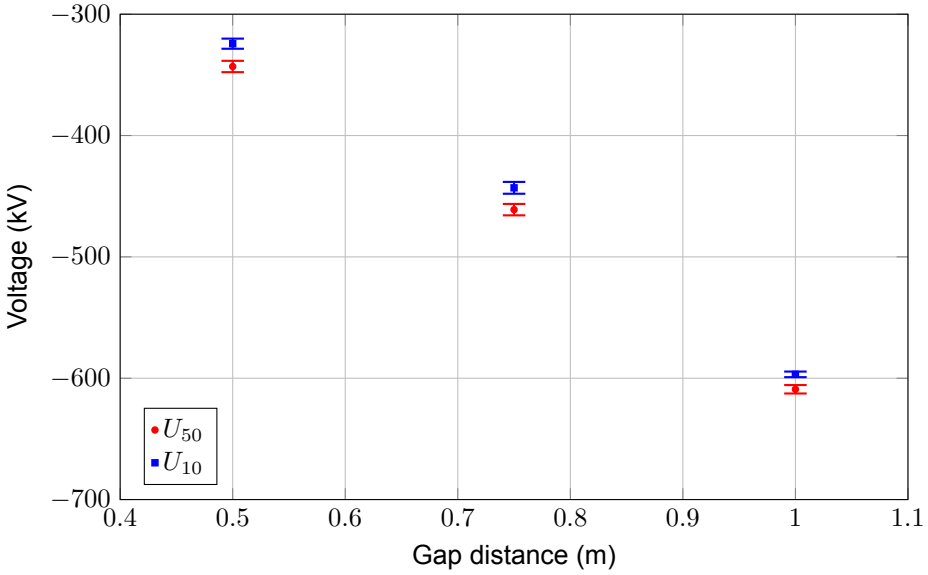

Figure 4.27: Conductor-rod U_{50} and U_{10} with 95% confidence intervals for negative impulses

4.4.4. Discussion

Comparison with literature

Gourgoulis et al. [37] report on a conductor-rod gap with a different setup, shown in Figure 4.28. U_{50} tests resulted in the breakdown voltages in Table 4.10.

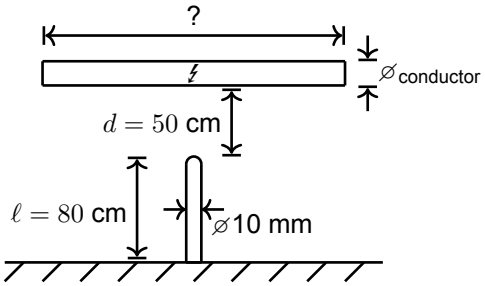

Figure 4.28: Conductor-rod gap from [37]

Table 4.10: U_{50} corresponding to the gap in Figure 4.28 from [37]

∅conductor (mm)	U_{50} (kV)
30	431
20	343

Although the T_{cr} of the applied impulses in the present work and in [37] are similar (125 µs and 100/150 µs respectively), the geometry is different, leading to different and incomparable results.

Characteristics of the flashover strength

The positive 0.75 m conductor-rod shows a large standard deviation ($\sigma = 7\%$). The measured probabilities and the fitted probability distribution are shown in Figure 4.29.

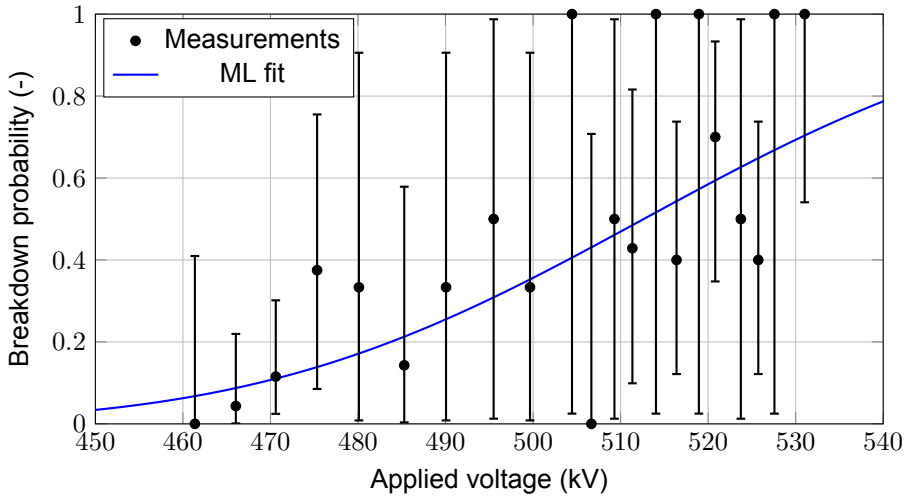

Figure 4.29: Breakdown probabilities with 95% confidence intervals and ML fit of the positively stressed 0.75 m conductor-rod gap

It can be concluded that there is indeed a wide variety in the empirical breakdown probabilities, but they also come with a large 95% confidence interval. The fitted probability distribution crosses through all the confidence intervals, indicating that the fit represents the data well. To reduce the variety and improve the fit of the distribution, more impulses at all levels should be applied, for instance, with a multiple-level test.

Figure 4.30 shows the time-to-breakdown of all conductor-rod gap distances under both positive and negative stresses. The rod-plane gap showed a clustering of negative time-to-breakdowns (see Figure 4.17). For the conductor-rod gap, it is observed that the time-to-breakdown for positive impulses is clustered, instead of the negative impulses. The differences between the two setups could be caused by the difference in geometry, as the rod-plane gap is the most asymmetric, while other gaps are more symmetric.

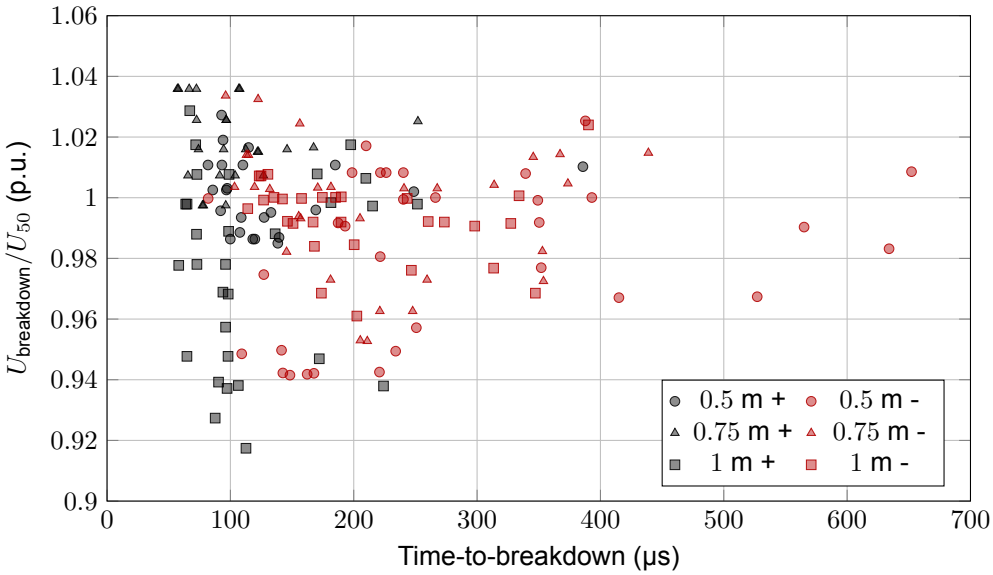

Figure 4.30: Time-to-breakdown of all gaps under positive and negative stresses

From Figure 4.30, it can be concluded that the T_{cr} for positive polarity impulses was around the critical time-to-crest, and the T_{cr} for negative polarity impulses was lower than critical [30].

4.5. Gap factor calculation

In this chapter, three geometries were tested. Firstly, the rod-plane gap, serving as a reference for the gap factor, secondly, the conductor-rod gap, and lastly, the needle-plane gap. Using the equation for the gap factor, the conductor-rod gap factor was derived for three distances:

$$k_g = \frac{U_{50,\text{gap}}}{U^+_{50,\text{rod-plane}}} \tag{4.10}$$

The $U_{50,\text{rod-plane}}$ results are taken from Table 4.3, and the $U_{50,\text{conductor-rod}}$ results are taken from Table 4.9. Both of these tables are at reference atmospheric conditions. The resulting gap factors with their 95% confidence intervals are shown in Table 4.11, together with the simulation results of Section 3.2, and a literature reference.

The confidence intervals for the gap factor are based on error propagation for division: if $z = \frac{x}{y}$, its standard deviation is defined as [50]:

$$\sigma_z = z \cdot \sqrt{\left(\frac{\sigma_x}{x}\right)^2 + \left(\frac{\sigma_y}{y}\right)^2} \tag{4.11}$$

Table 4.11: Comparison of gap factors for the conductor-rod gap, with 95% confidence intervals for the experimental results

Gap distance and polarity	Experimental k_g (Sec. 4.4)	Simulation k_g (Sec. 3.2)	Hileman k_g [17]
0.5 m +	1.34 ± 0.01	1.52	1.4 - 1.6
0.5 m -	1.23 ± 0.02		
0.75 m +	1.34 ± 0.04	1.50	1.4 - 1.6
0.75 m -	1.21 ± 0.03		
1 m +	1.35 ± 0.08	1.44	1.4 - 1.6
1 m -	1.25 ± 0.04		

From this table, it can be concluded that the gap factor for the conductor-rod gap under positive stresses is around at 1.34, and under negative stresses around 1.23. These values, however, do not match the results obtained by the simulations performed in Section 3.2, ranging from 1.44 to 1.52. Therefore, the method of Schneider and Weck [7] is concluded not to be valid for gap distances smaller than 2 meters. The difference between the experimental and simulation results decreases as the gap distance approaches 2 m, from 0.18 at 0.5 m to 0.09 at 1 m with overlapping confidence intervals. This indicates the validity of this method for larger gap distances. Hileman [17] suggests a gap factor of 1.4 to 1.6 for $d > 2$ m. The experimental results are not far from this value, although they lie outside this range.

Table 4.12 shows the differences in gap factor when a different rod-plane reference strength than the experimentally found strength is used.

Table 4.12: Conductor-rod gap factors based on different rod-plane references: the rod-plane experimental results, the CRIEPI equation (Eq. 2.6), and the Feser equation (Eq. 2.7).

Gap distance and polarity	Based on rod-plane results	Based on CRIEPI	Based on Feser
0.5 m +	1.34 ± 0.01	1.66	1.43
0.5 m -	1.23 ± 0.02	1.53	1.32
0.75 m +	1.34 ± 0.04	1.60	1.38
0.75 m -	1.21 ± 0.03	1.44	1.24
1 m +	1.35 ± 0.08	1.61	1.42
1 m -	1.25 ± 0.04	1.49	1.31

There is a large difference between positive and negative polarity gap factors. This is also explained in literature [13], [23], [33]. Figure 4.31 compares the gap factors from literature with the experimental results, and it can be seen that they are well in line. The solid line is the line where the positive and negative breakdown strengths are the same. Above this line, the negative gap is stronger and vice versa for the positive gap. The shaded region between the dashed lines indicates the range in which most results lie. For this graph, the experimental gap factors are calculated using the Gallet equation (Eq. 2.5), since the CIGRE results are also calculated using this equation as a reference, even though the Gallet equation is valid only for $d > 1$ m.

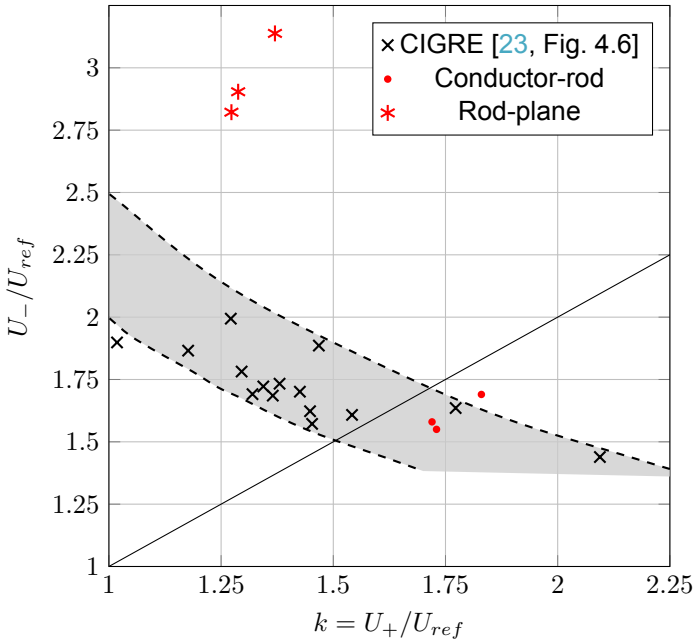

Figure 4.31: Gap strength under positive and negative polarity switching impulses. $U_{ref} = \frac{3450}{1+\frac{8}{d}}$ (Eq. 2.5)

From the figure, it can be seen that the rod-plane results are outside of the range of normally found gap factors. An explanation for this is that the Gallet equation is used to calculate the gap factor, although Figure 4.9 already showed that the Gallet equation does not fit the found breakdown strength well.

The results of Gourgoulis et al [37] on conductor-rod gaps are also used to validate the method of Schneider and Weck. This is shown in Table 4.13.

Table 4.13: Comparison of gap factors of [37] with simulation results

Diameter conductor	**Experimental k_g [37]**	**Simulation k_g (acc. Sec. 3)**	**Hileman k_g [17]**
2 cm	1.56	1.67	1.4-1.6
3 cm	1.94	1.69	

This table again shows a large difference between the experimental and simulation results, supporting the earlier claim that the method of Schneider and Weck is not valid for gaps smaller than 2 m.

5

Experimental work on complex geometries

The objective of this work is to investigate the minimal safety clearances for the BRP busbar disconnector. Therefore, tests are performed to determine the dielectric strength of this setup. The busbar disconnector is shown in Figure 5.1.

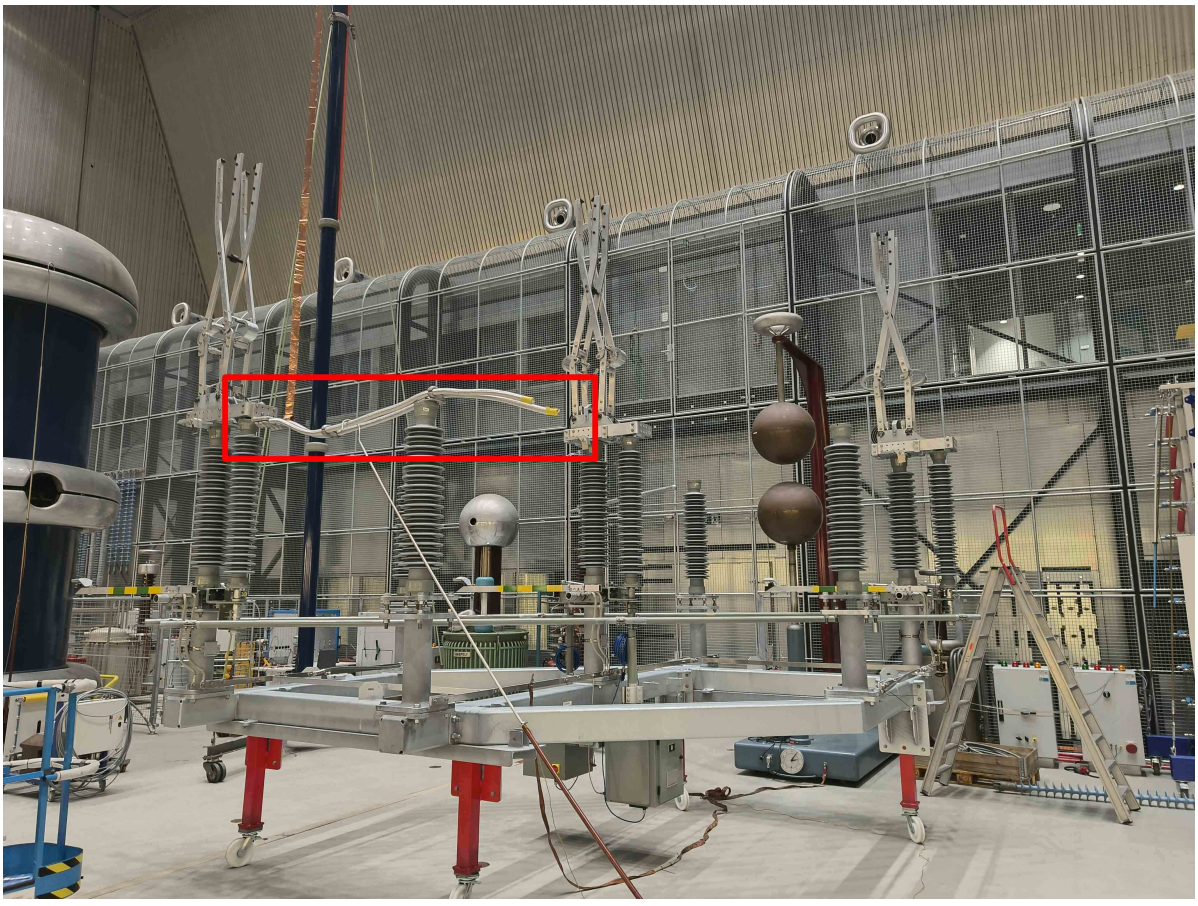

Figure 5.1: BRP busbar disconnector with the flexible conductors boxed in red

Two flexible conductors ($\varnothing\,28$ mm) are mounted to one of the outer phases (boxed in red in Figure 5.1), connected by a spacer in the middle and supported by a post insulator at the end. The conductor has a clearance to ground of at least 1100 mm (the clearance of the post insulator). No conductors are mounted to the remaining two phases. A rod will be placed pointing towards two different locations in the busbar disconnector. The rod represents the arm of a worker performing maintenance. The rod is placed at a horizontal distance of 0.5, 0.75 and 1 m. Next to tests with a rod, there will also be tests performed with a needle. This needle stands for a sharp object, e.g. a screwdriver, and will also be placed pointing at the busbar disconnector.
The impulses are applied at the far end of the conductor. The other two phases, frame and rod/needle, are grounded.

5.1. Simulation of the BRP busbar disconnector

The BRP busbar disconnector is modelled using COMSOL Multiphysics®. The 3D model is shown in Figure 5.2. This is a simplified model without bolts, nuts, holes and other small details that are considered to be of little impact on the simulation results, but have a high impact on the computational intensity.

Breakdowns start in the presence of a high electric field [34], and with this 3D model, it is studied where the highest electric field occurs on the busbar disconnector. To this end, the frame is grounded, and the three phases are energised with the normal operation voltage of $U = 123\sqrt{2/3} \approx 100$ $\mathrm{kV_{peak}}$, with a $120°$ phase shift between the three phases.

The electric field simulation indicated two locations with the highest electric field: the fixed earthing contact and the tip of the pantograph, as indicated in Figure 5.3. The highest electric field occurs at the tip of the pantograph, with a field strength of $E = 2.04$ kV/mm. The simulation showed that the electric field at the earthing contact is $E = 0.29$ kV/mm. As these two locations show the highest electric field, the breakdown strength of both these gaps will be investigated in this chapter.

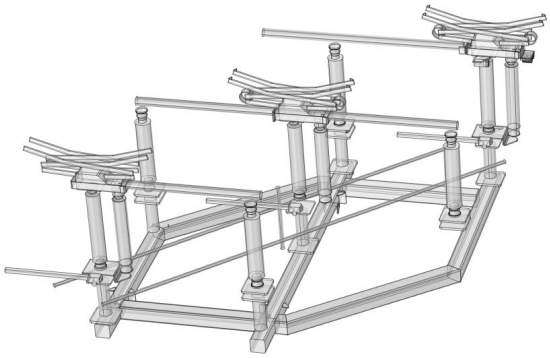

Figure 5.2: 3D COMSOL model of the BRP busbar disconnector

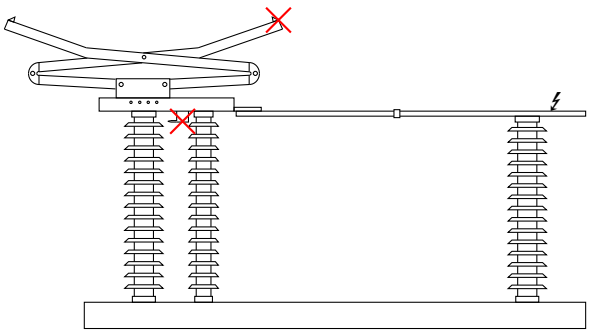

Figure 5.3: Locations of the studied electric field

5.2. Conductor in disconnector - rod

5.2.1. Geometry

The same rod as in Section 4.2 and 4.4 is used:

- Diameter rod: 6 cm, with hemispherical tip
- Length rod: 2.5 m

This rod is placed horizontally on a post insulator at the height of the spacer, pointing directly towards the spacer, as shown in Figure 5.4 and 5.5.

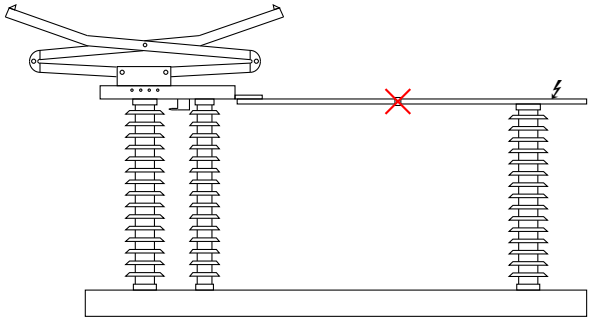

Figure 5.4: Placement of the rod

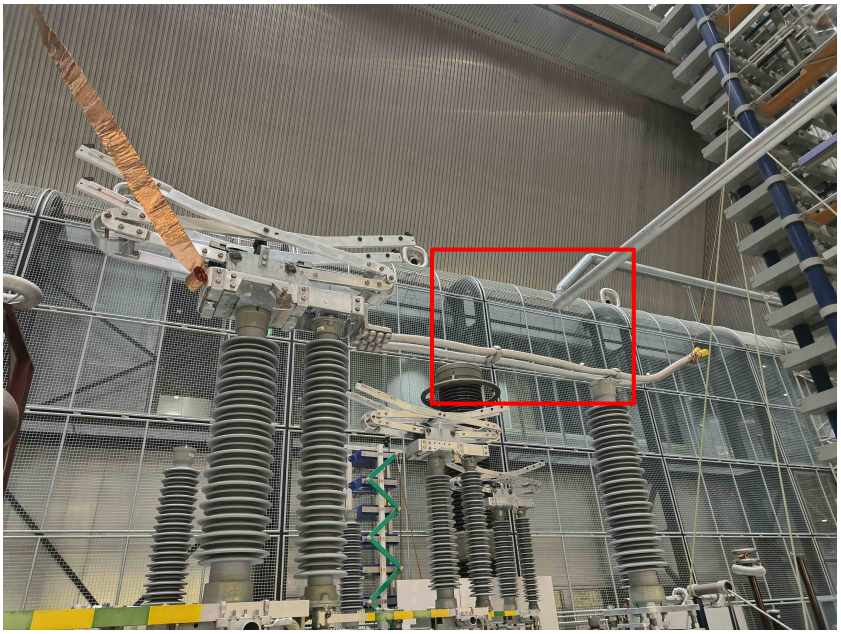

Figure 5.5: Disconnector conductor-rod gap

5.2.2. Test execution

The test was executed with the impulse generator, generating a waveform of $T_{cr} \approx 127$ µs and $T_{tail} \approx 2103$ µs. The critical T_{cr} for this specific geometry is not known, therefore, the same T_{cr} as for the conductor-rod gap (Sec. 4.4) was used, as the geometries look alike. An up-and-down test with $n = 1$ was performed to determine U_{50}.

While searching for the starting point of the positive U_{50} test, flashover over the insulator occurred at a voltage of 532 kV. A short up-and-down test was performed around this value to see if there would be a sparkover from the conductor to the rod instead of a flashover over the insulator. This short up-and-down test consisted of 7 impulses at voltage levels 534, 540, 544, and 549 kV. Three withstands and four breakdowns were observed. All the breakdowns were flashovers over the insulator. As insulator flashovers do not influence the safety clearances, no further tests on this geometry are performed with positive polarity, and only negative switching impulses are applied. The SIWV for the busbar disconnector is 486.27 kV according to Equation 2.1, so flashovers over the insulator at 532 kV are acceptable.

During the day of testing, the relative air humidity in the laboratory changed noticeably from 42.2% RH to 33.7% RH. This effect has been mitigated by correcting for the humidity for each test separately instead of taking the daily average.

Figure 5.6: Flashover over the insulator

5.2.3. Results

Since no breakdown data for positive polarity impulses is known, this subsection only considers negative polarity impulses. The results of the tests, analysed with the maximum likelihood method, are listed in Table 5.1. The full test results are listed in Appendix B.

Table 5.1: Disconnector conductor-rod results, with 95% confidence intervals

Gap distance	U_{50} (kV)	σ (kV)	σ/U_{50} (%)	# impulses
0.5 m -	318 ± 2	11 ± 5	3.5 ± 1.6	101
0.75 m -	456 ± 3	9 ± 4	2.0 ± 0.9	66
1 m -	603 ± 4	13 ± 7	2.2 ± 1.2	60

From the U_{50} and σ, U_{10} can be derived as (see Sec. 2.2):

$$U_{10} = U_{50} - 1.282\sigma \tag{5.1}$$

The derived U_{10} are shown in Table 5.2, where the 95% confidence intervals are determined through the Clopper-Pearson method [43] in the MATLAB function `binofit` [42]. U_{50} and U_{10} combined are shown in Figure 5.7.

Table 5.2: Derived U_{10} values from U_{50} and σ

Gap distance	U_{10} with 95% CI (kV)
0.5 m -	303 ± 7
0.75 m -	445 ± 6
1 m -	587 ± 10

As the U_{10} is not tested, but derived from U_{50}, its 95% confidence intervals will be larger than those of the U_{50} test, which can be seen from Figure 5.7.

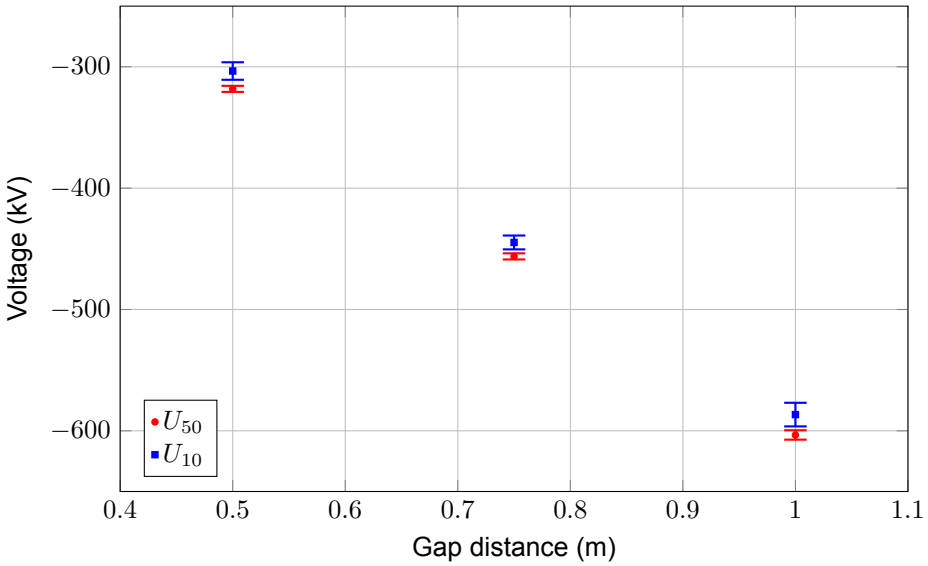

Figure 5.7: Disconnector conductor-rod U_{50} and derived U_{10} with 95% confidence intervals

5.2.4. Discussion

Characteristics of the flashover strength

The results were analysed with the maximum likelihood method. Figure 5.8 shows the empirical breakdown probabilities and the fitted distribution. The fit represents the data very well. The voltages with large confidence intervals are those visited fewer times, for instance, when searching for the starting point of the up-and-down test.

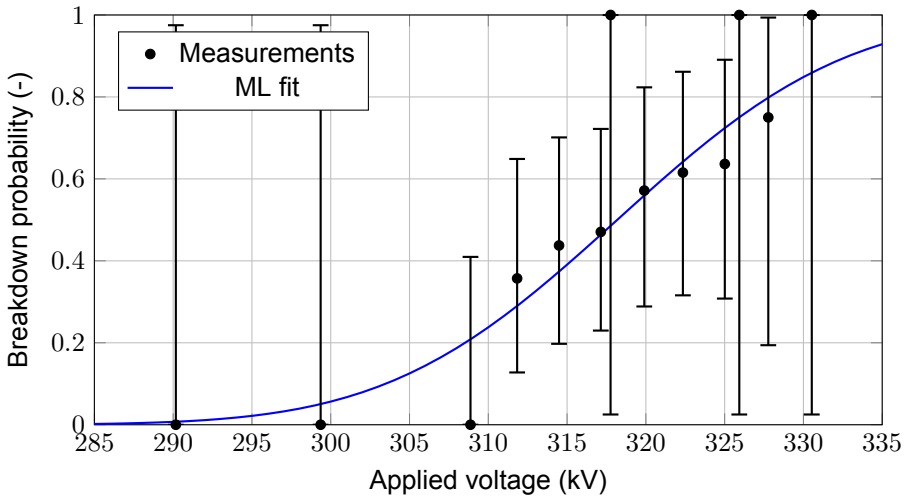

Figure 5.8: Breakdown probabilities with 95% confidence intervals and ML fit of the negatively stressed 0.5 m disconnector conductor-rod gap

Comparison to pure conductor-rod gap

As the gap discussed in this section is similar to the pure conductor-rod gap from Section 4.4, it is interesting to see how the surrounding geometry (pantograph, skid, bolts, etc.) affects the breakdown voltage of the gap. Table 5.3 compares the 50% breakdown voltages of the two gaps.

Table 5.3: Comparison between pure conductor-rod gap and the disconnector conductor-rod gap

Gap distance	Pure conductor-rod U_{50} with 95% CI (kV)	Disconnector conductor-rod U_{50} with 95% CI (kV)
0.5 m -	343 ± 5	318 ± 2
0.75 m -	461 ± 5	456 ± 3
1 m -	609 ± 3	603 ± 4

- **Behaviour under positive stresses:**
  There were no sparkovers between the conductor in the disconnector and the rod for positive impulses. Instead, only flashovers over the insulator were observed.
- **Behaviour under negative stresses:**
  The 95% confidence intervals for the 0.75 m and 1 m gaps overlap, and their breakdown voltages are relatively close. However, for the 0.5 m gap, there is a larger difference between the pure conductor-rod gap and the conductor-rod gap in the busbar disconnector. This could be due to the fact that for small distances, the influence of the spacer in the conductors becomes larger, i.e. the field distortion caused by the spacer has a larger effect on the electric field close to the spacer. At a larger distance from the spacer, this effect decreases and the electric field distribution becomes more similar to the electric field distribution of the pure conductor-rod gap.

5.3. Pantograph in disconnector - rod

5.3.1. Geometry

The same ⌀6 cm rod with a hemispherical tip is used as before. The rod is now placed at an angle on the same post insulator as before. The COMSOL simulation showed that the E-field is the highest at the end of the pantograph. The rod is therefore placed pointing towards this point at the pantograph, shown in Figures 5.9 and 5.11. The end of the pantograph is a sharp saw cut, covered with a plastic lid as shown in Figure 5.10.

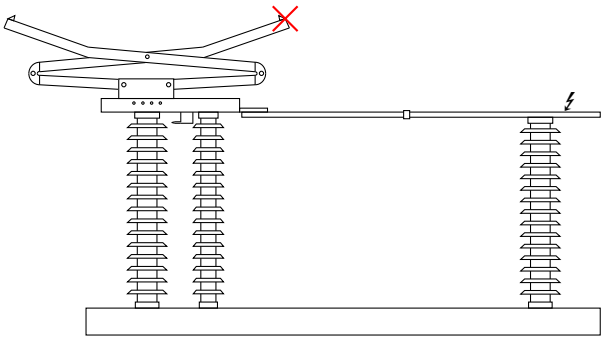

Figure 5.9: Placement of the rod

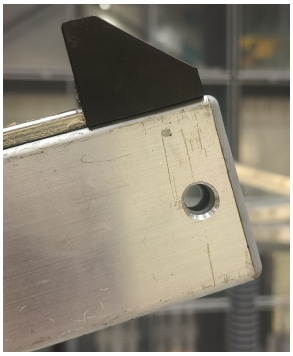

Figure 5.10: Edge of the pantograph

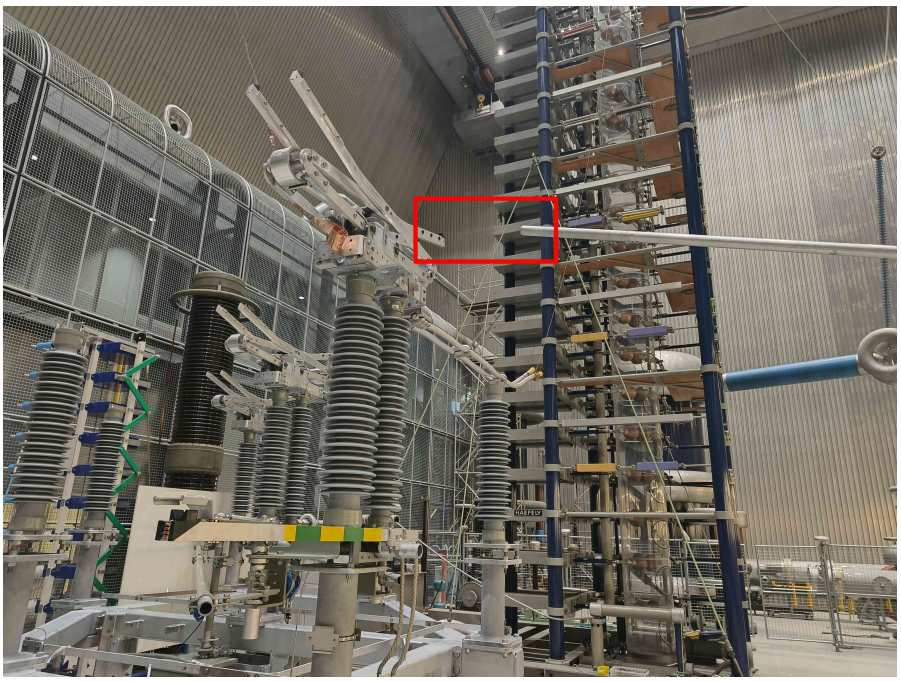

Figure 5.11: Disconnector pantograph-rod gap

5.3.2. Test execution

The test was executed with the impulse generator, generating a waveform of $T_{cr} \approx 126$ µs and $T_{tail} \approx 2098$ µs. As for the disconnector conductor-rod gap, the critical T_{cr} is not known and the same T_{cr} as before is used. An up-and-down test with $n = 1$ was performed to determine U_{50}.
This geometry allowed for sparkovers to the rod for positive polarity impulses at $d = 0.5$ and 0.75 m. For a gap distance of $d = 1$ m, flashovers over the insulator occurred instead of sparkovers to the rod, at voltage levels of 554, 573, 582, 600, and 647 kV.

5.3.3. Results

The results from the up-and-down tests determined using the maximum likelihood method are listed in Table 5.4. The full test results are listed in Appendix B.

Table 5.4: Disconnector pantograph-rod results, with 95% confidence intervals

Gap distance	U_{50} with 95% CI (kV)	σ (kV)	σ/U_{50} (%)	# impulses
0.5 m +	358 ± 3	10 ± 6	2.8 ± 1.7	72
0.5 m -	306 ± 8	33 ± 22	10.8 ± 7.2	89
0.75 m +	527 ± 2	4 ± 2	0.8 ± 0.4	38
0.75 m -	414 ± 2	9 ± 5	2.2 ± 1.2	50
1 m -	560 ± 3	12 ± 7	2.1 ± 1.3	67

Using Equation 5.1, the U_{10} has been derived from these results. The 95% confidence intervals are determined through the Clopper-Pearson method [43] in the MATLAB function `binofit` [42]. This is shown in Table 5.5.

Table 5.5: Derived U_{10} values from U_{50} and σ

Gap distance	U_{10} with 95% CI (kV)
0.5 m +	345 ± 7
0.5 m -	263 ± 27
0.75 m +	522 ± 3
0.75 m -	402 ± 7
1 m -	544 ± 9

The results are graphically shown in Figures 5.12 (positive stresses) and 5.13 (negative stresses).

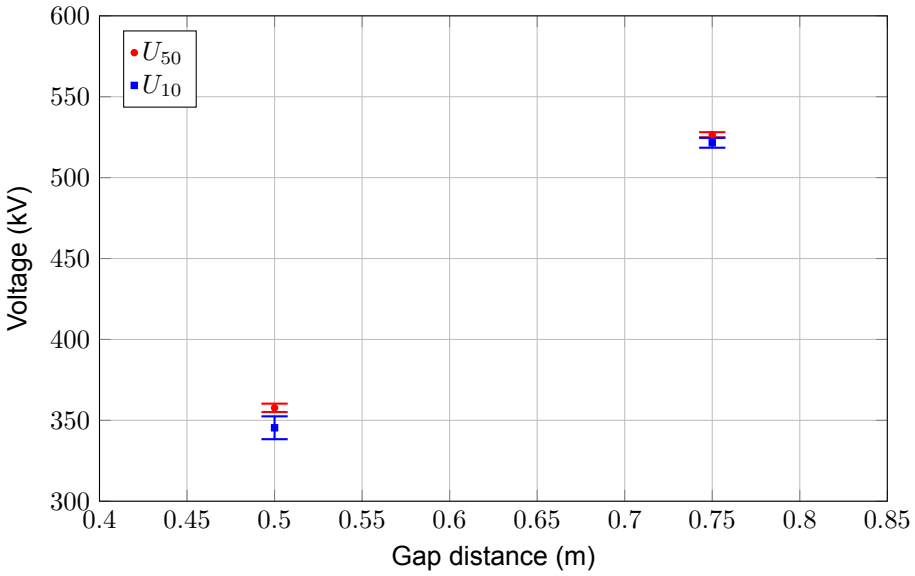

Figure 5.12: Pantograph-rod U_{50} and U_{10} with 95% confidence intervals for positive impulses

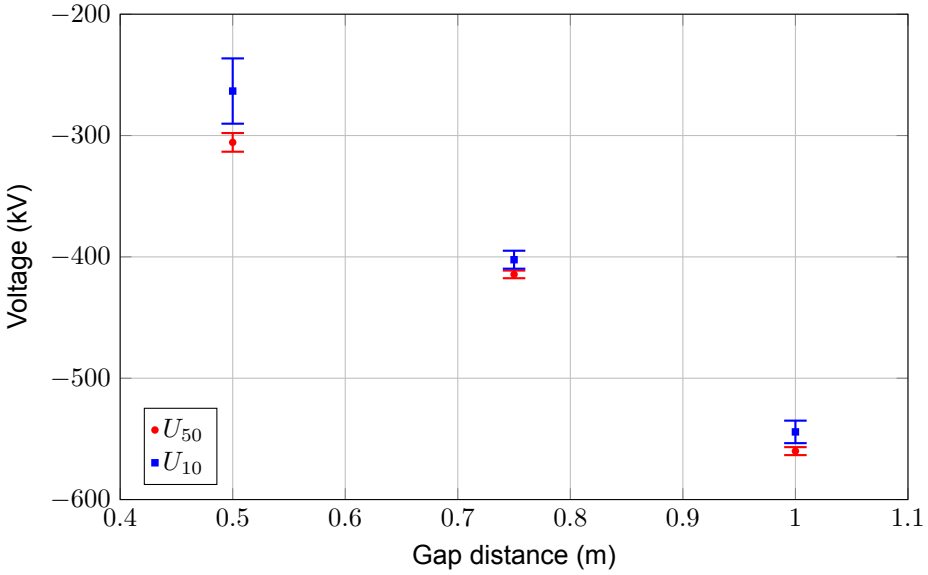

Figure 5.13: Pantograph-rod U_{50} and U_{10} with 95% confidence intervals for negative impulses

Table 5.4 shows a large standard deviation for the 0.5 m gap under negative stresses compared to other gaps. Next to this, the 95% confidence interval of the U_{10} is considerably larger than the confidence intervals of other gaps. Therefore, a modified multiple-level test with $n \geq 10$ (see Section 4.1.2) was performed to determine the U_{10} through testing instead of deriving from the U_{50}. The modified multiple-level method is preferred over an up-and-down test to determine U_{10} in this case, as the modified multiple-level method does not allow for voltage levels with low breakdown probabilities, and hence will give a better fit in the maximum likelihood method. In this specific modified multiple-level test, every level should have at least 2 breakdowns. The starting voltage level is chosen to be $U_{50} \approx 306$ kV, and the difference between voltage levels $\Delta U \approx 1\% = 3$ kV. The per-level results of this test are shown in Table 5.6.

Table 5.6: Modified multiple-level test results per level for the 0.5 m negatively stressed pantograph-rod gap

Level	Voltage (kV)	# breakdowns	# impulses
1	304	5	10
2	301	3	10
3	299	4	10
4	296	4	10
5	293	2	10
6	290	3	10
7	287	2	10
8	284	2	10
9	281	2	23
10	279	3	17
11	275	2	44

These results are analysed using the maximum likelihood method, leading to the results in Table 5.7.

Table 5.7: Modified-multiple level method results for the 0.5 m negatively stressed pantograph-rod gap

U_{50} with 95% CI (kV)	U_{10} with 95% CI (kV)	σ (kV)	σ/U_{50} (%)	# impulses
305 ± 8	279 ± 5	20 ± 8	7	164

From the above table, it can be seen that the confidence interval for the U_{10} is smaller than the U_{50} confidence interval, as there are more impulses applied at the voltage levels around U_{10}. Figure 5.14 shows the updated results for the 0.5 m pantograph-rod gap.

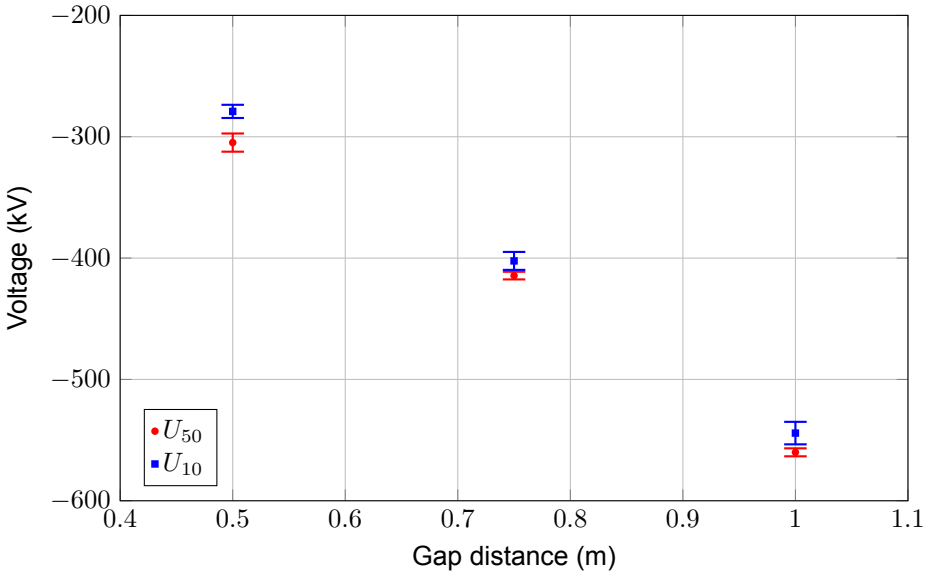

Figure 5.14: Pantograph-rod U_{50} and U_{10} with 95% confidence intervals for negative impulses. The measurements for $d = 0.5$ m were conducted using the modified multiple-level method.

5.3.4. Discussion

Large σ for the 0.5 m gap under negative stresses

The up-and-down method to determine the U_{50} for the 0.5 m gap under negative stresses resulted in a large standard deviation, which led to a relatively low U_{10} and large confidence intervals. Therefore, a modified multiple-level method was executed. The results of the two test methods are compared in Table 5.8.

Table 5.8: Up-and-down U_{50} method compared to the modified multiple-level method for the 0.5 m negatively stressed pantograph-rod gap, with 95% confidence intervals

	U_{50} (kV)	U_{10} (kV)	σ (kV)	σ/U_{50} (%)	# impulses
U_{50} up-and-down method with derived U_{10}	306 ± 8	263 ± 27	33 ± 22	10.8 ± 7.2	89
Modified multiple-level method	305 ± 8	279 ± 5	20 ± 8	6.6 ± 2.6	164

The U_{50} only changed slightly, as expected. The U_{10}, on the other hand, changed from 263 to 279 kV, while the confidence interval was reduced from 27 to 5 kV. For gaps with a large scatter (i.e., large σ), it is therefore advisable to perform a (modified) multiple-level method.

Comparison with literature

Figure 5.15 shows a comparison between the results from this section and literature. For this graph, the experimental gap factors are calculated using the Gallet equation (Eq. 2.5), since the CIGRE results are also calculated using this equation as a reference, even though the Gallet equation is valid only for $d > 1$ m.

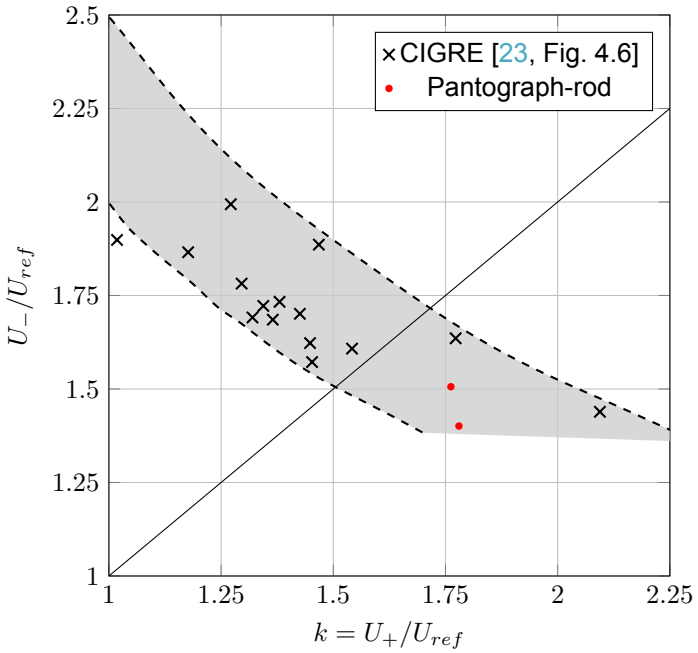

Figure 5.15: Gap strength under positive and negative polarity switching. $U_{ref} = \frac{3450}{1+\frac{8}{d}}$ (Eq. 2.5)

It is observed that the found ratio between positive and negative breakdown voltages is in line with the literature.

Figure 5.16 shows a breakdown of the pantograph-rod gap.

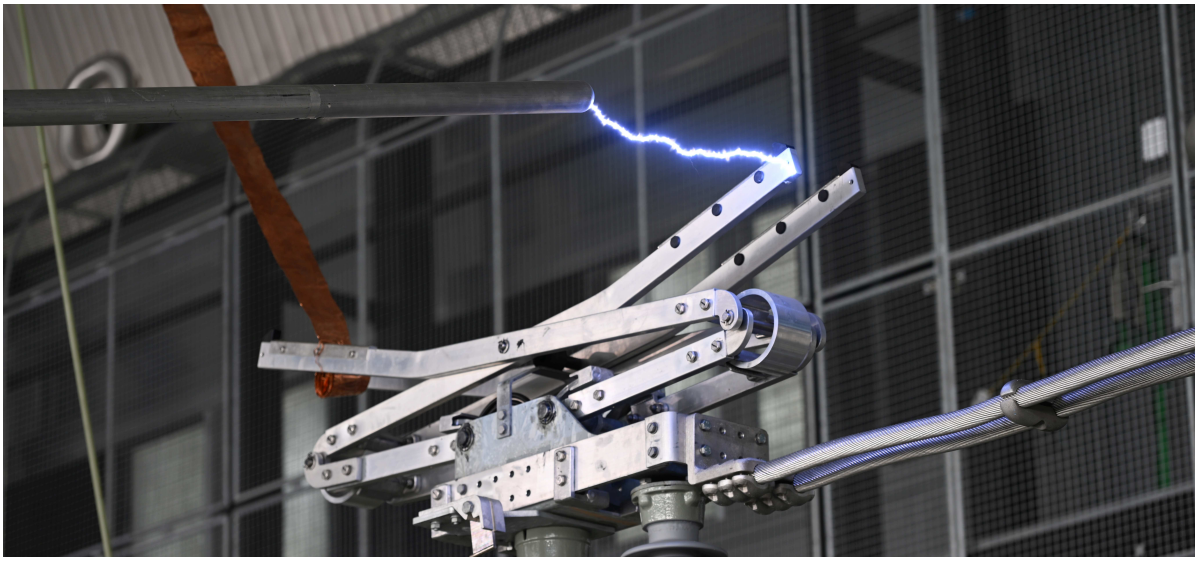

Figure 5.16: Breakdown of the pantograph-rod gap

5.4. Pantograph in disconnector - needle

To investigate whether the breakdown voltage depends on the radius of the grounded object, a needle is now placed facing the pantograph, instead of a rod.

5.4.1. Geometry

The needle is composed as follows:

- Rod with a rounded tip with a length of 1.34 m and a diameter of 50 mm, attached to:
- Blunt-tipped rod with a length of 45 cm and a diameter of 10 mm

The needle is shown in Figure 5.17, and it is placed at a distance of 0.5 and 0.75 m, pointing towards the same point as shown in Figure 5.9. The rod and needle were placed at an angle to adhere to the gap distances. The setup is depicted in Figure 5.18.

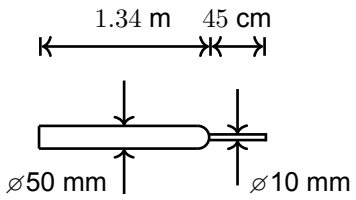

Figure 5.17: Needle geometry used for testing

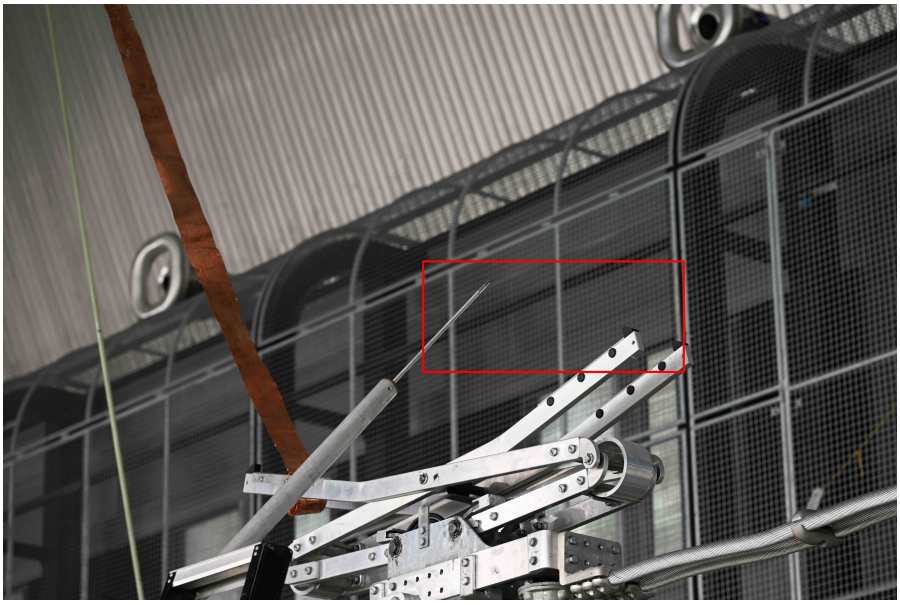

Figure 5.18: Pantograph-needle setup

5.4.2. Test execution

An up-and-down test with $n = 1$ was executed to determine the U_{50}. The impulse generator generated a waveform of $T_{cr} \approx 127$ µs and $T_{tail} \approx 2108$ µs. Only negative stresses were applied, as this resulted in the lowest breakdown voltages (and hence the most critical for determining clearances) for the pantograph-rod gap in Section 5.3.

5.4.3. Results

The results are analysed using the maximum likelihood method, and listed in Table 5.9. The full test results are listed in Appendix B.

Table 5.9: Disconnector pantograph-needle results, with 95% confidence intervals

Gap distance	U_{50} (kV)	σ (kV)	σ/U_{50} (%)	# impulses
0.5 m -	284 ± 1	3 ± 1	1.1 ± 0.4	49
0.75 m -	417 ± 1	4 ± 2	0.9 ± 0.5	50

Using Equation 5.1, the U_{10} is derived, leading to the results listed in Table 5.10. The 95% confidence intervals are determined through the Clopper-Pearson method [43] in the MATLAB function `binofit` [42].

Table 5.10: Derived U_{10} values from U_{50} and σ for the pantograph-needle gap

Gap distance	U_{10} with 95% CI (kV)
0.5 m -	280 ± 2
0.75 m -	411 ± 3

5.4.4. Discussion

Comparison with pantograph-rod

Figure 5.19 shows the 50% breakdown voltages of the pantograph-rod and the pantograph-needle gap.

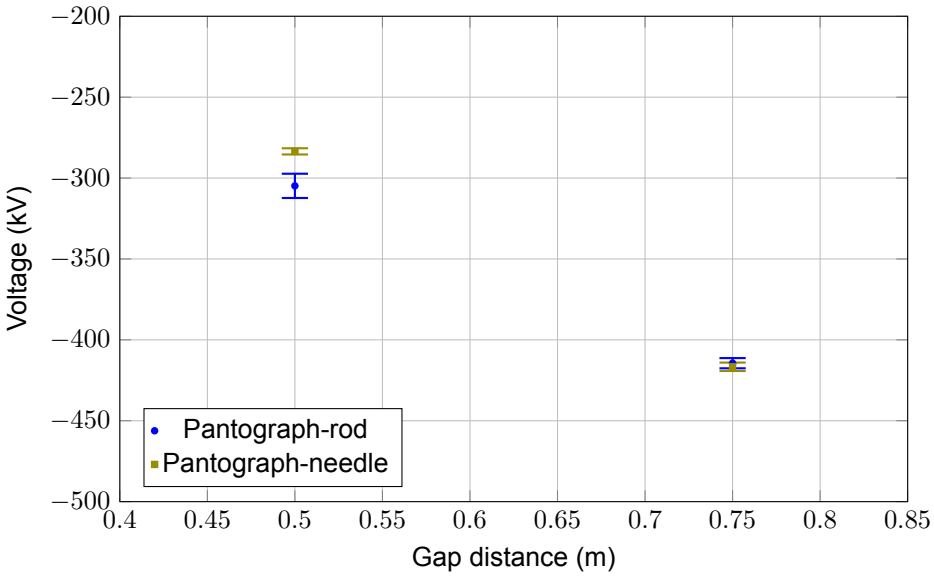

Figure 5.19: U_{50} of the pantograph-rod compared with the pantograph-needle for negative stresses

It can be seen that the 50% breakdown strength for the 0.5 m gap is higher for the $\varnothing$6 cm rod than for the $\varnothing$1 cm rod. For the 0.75 m gap, this difference is not observed. This can be explained by the fact that for small gaps, rod size has a large influence on the electric field distribution near the pantograph. For larger gaps, this effect becomes smaller.

5.5. Earthing contact in disconnector - needle

The COMSOL simulation showed that the E-field at the pantograph is the highest, followed by the fixed earthing contact on the disconnector. Therefore, the breakdown strength at this location is also investigated. The grounded electrode is a needle, to mimic the worst-case scenario.

5.5.1. Geometry

The same rod as shown in Figure 5.17 is used. It is placed at an angle, at a horizontal distance of 0.5 and 0.75 m from the earthing contact, indicated in Figure 5.20.

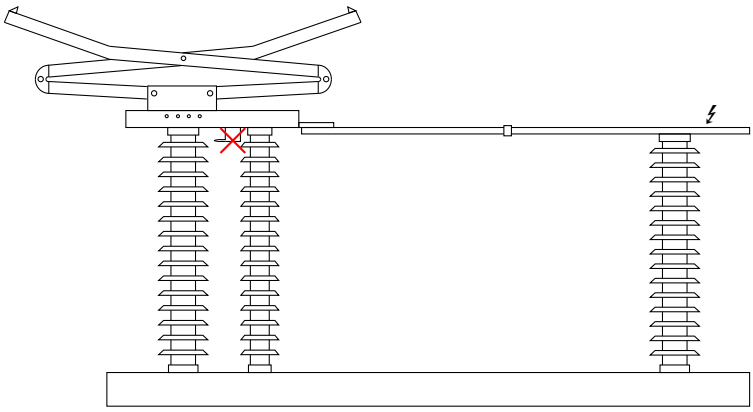

Figure 5.20: Placement of the rod

The laboratory setup is shown in Figure 5.21.

Figure 5.21: Earthing contact - needle gap

5.5.2. Test execution

As for the pantograph-needle, an up-and-down test with $n = 1$ was executed to determine the U_{50}. The impulse generator generated a waveform of $T_{cr} \approx 126$ µs and $T_{tail} \approx 2106$ µs. Only negative stresses were applied. All of the breakdowns were encountered between the needle and the bolt above the earthing contact, as can be seen in Figure 5.22.

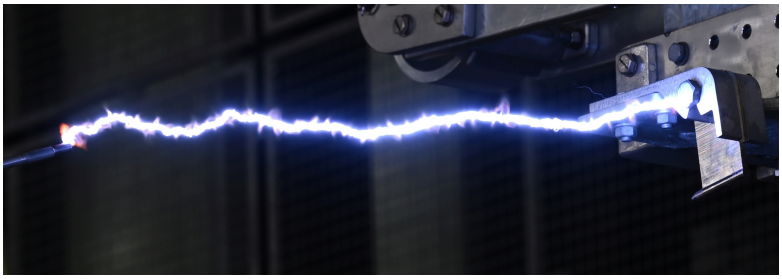

Figure 5.22: Breakdown of the earthing contact-needle gap

5.5.3. Results

The results of the tests are shown in Table 5.11. The full test results are listed in Appendix B.

Table 5.11: Disconnector earthing contact-needle results, with 95% confidence intervals

Gap distance	U_{50} (kV)	σ (kV)	σ/U_{50} (%)	# impulses
0.5 m -	269 ± 1	2 ± 1	0.7 ± 0.4	39
0.75 m -	420 ± 2	5 ± 2	1.2 ± 0.5	47

Using Equation 5.1, the U_{10} is derived, leading to the results listed in Table 5.12. The 95% confidence intervals are determined through the Clopper-Pearson method [43] in the MATLAB function `binofit` [42].

Table 5.12: Derived U_{10} values from U_{50} and σ for the earthing contact-needle gap

Gap distance	U_{10} with 95% CI (kV)
0.5 m -	267 ± 1
0.75 m -	414 ± 3

5.5.4. Discussion

Comparison with pantograph-needle

Figure 5.23 shows a comparison between the 50% breakdown strength of the pantograph-needle gap and the earthing contact-needle gaps.

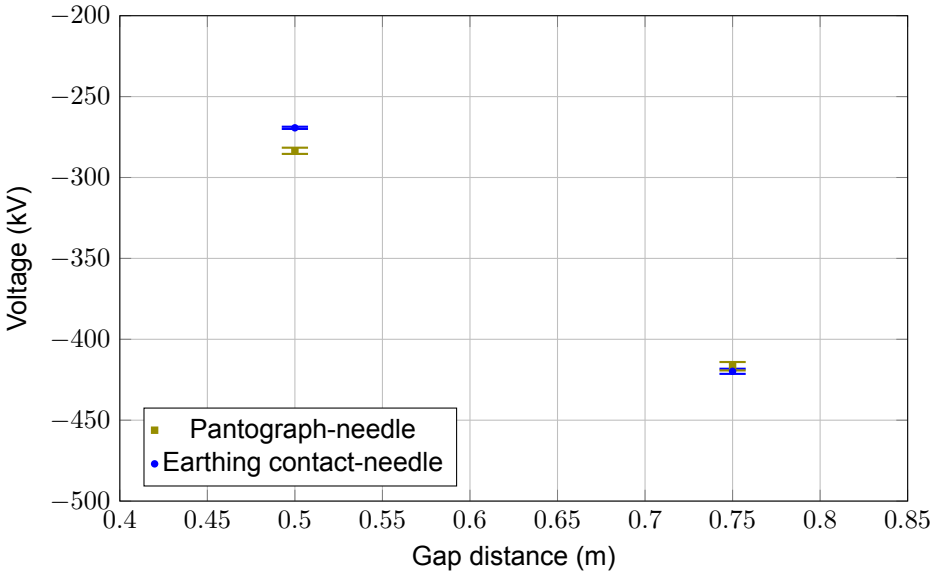

Figure 5.23: U_{50} of the pantograph-needle compared with the earthing contact-needle for negative stresses

Even though the COMSOL simulation showed a lower electric field strength near the earthing rod, the breakdown strength of these gaps is lower. The simulation, however, did not take into account details like bolts and nuts. This could have caused a lower electric field strength than encountered in practice, resulting in a lower breakdown strength.

5.6. Overall results

Figure 5.24 shows the 50% breakdown strengths of all the gaps considered in this chapter. All of these gaps are considered to be found when work is performed on the BRP busbar disconnector.

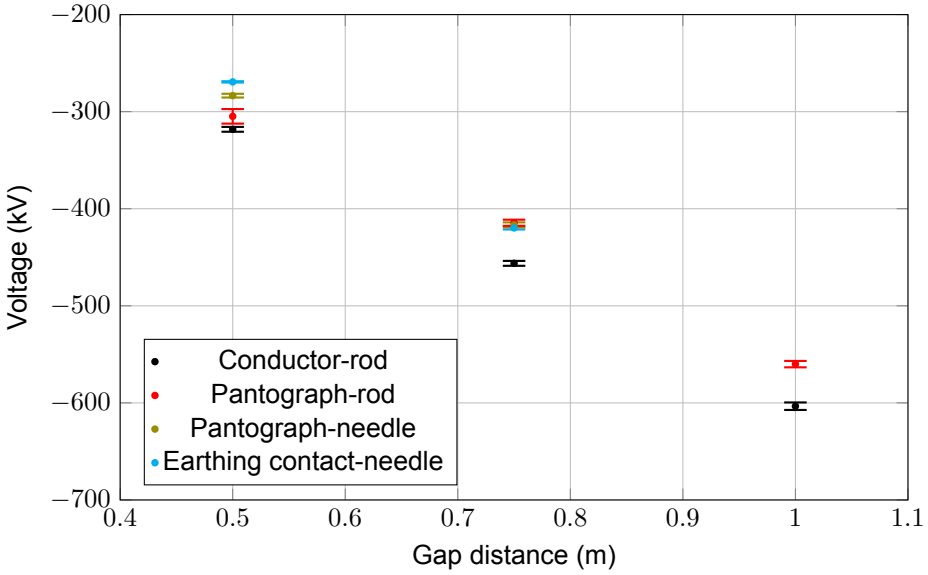

Figure 5.24: U_{50} including 95% confidence intervals of all the gaps encountered in this chapter, for negative stresses

It can be seen that amongst all the gaps and gap distances, the conductor-rod has the highest breakdown strength, i.e. is the strongest gap. The earthing contact-needle has the lowest breakdown strength for a gap distance of 0.5 m. At a gap distance of 0.75 m, there is virtually no difference between the pantograph-rod, pantograph-needle and earthing contact-needle gaps. The pantograph-needle and earthing contact-needle gaps are not tested at a gap distance of 0.75 m.

Table 5.13 lists the gap factors that are found with the experimental results from this chapter. The gap factors are calculated using Equation 2.10, where for the conductor-rod and pantograph-rod gaps the U_{50} of the rod-plane is used as the reference (Sec. 4.2), and for the pantograph-needle and earthing contact-needle, the U_{50} of the needle-plane gap is taken as the reference (Sec. 4.3). The different references are taken as there exists a significant difference in breakdown strengths of the rod-plane and needle-plane gaps. The confidence intervals are calculated using Equation 4.11.

Table 5.13: Gap factors for the gaps considered in this chapter

Gap	Distance and polarity	Gap factor and 95% CI	Reference gap
Conductor-rod	0.5 m -	1.14 ± 0.01	Rod-plane (Sec. 4.2)
	0.75 m -	1.20 ± 0.01	
	1 m -	1.24 ± 0.02	
Pantograph-rod	0.5 m +	1.28 ± 0.01	
	0.5 m -	1.10 ± 0.02	
	0.75 m +	1.38 ± 0.01	
	0.75 m -	1.09 ± 0.02	
	1 m -	1.15 ± 0.03	
Pantograph-needle	0.5 m -	1.11 ± 0.01	Needle-plane (Sec. 4.3)
	0.75 m -	1.18 ± 0.03	
Earthing contact-needle	0.5 m -	1.05 ± 0.01	
	0.75 m -	1.19 ± 0.03	

This table indicates that the gap factor for the pantograph-rod and the pantograph-needle is comparable when taken with respect to the correct reference gap. A minimum gap factor of 1.05 is observed for the 0.5 m earthing contact-needle gap.
Table 5.14 shows the differences in gap factor when a different rod-plane reference strength is used.

Table 5.14: Disconnector gap factors based on different rod-plane references: the rod-plane experimental results, the CRIEPI equation (Eq. 2.6), and the Feser equation (Eq. 2.7).

Gap	Distance and polarity	Based on rod-plane results	Based on CRIEPI	Based on Feser
Conductor-rod	0.5 m -	1.14 ± 0.01	1.42	1.22
	0.75 m -	1.20 ± 0.01	1.42	1.23
	1 m -	1.24 ± 0.02	1.48	1.30
Pantograph-rod	0.5 m +	1.28 ± 0.01	1.60	1.38
	0.5 m -	1.10 ± 0.02	1.37	1.18
	0.75 m +	1.38 ± 0.01	1.65	1.42
	0.75 m -	1.09 ± 0.02	1.29	1.12
	1 m -	1.15 ± 0.03	1.37	1.21
Pantograph-needle	0.5 m -	1.11 ± 0.01	1.27	1.09
	0.75 m -	1.18 ± 0.03	1.30	1.13
Earthing contact-needle	0.5 m -	1.05 ± 0.01	1.20	1.04
	0.75 m -	1.19 ± 0.03	1.31	1.13

6

Determination of safety distances

Electrical safety in high voltage substations consists of two parts: electrical clearance and safety regarding maximum electromagnetic fields. The safety distances related to these parts are discussed in this chapter.

6.1. Electrical clearance

To determine the electrical clearance, the IEC 61472 standard on live working is used [6]. However, this standard does not follow the horizontally structured insulation coordination standards (IEC 60071). This section proposes a method to homogenise the standards for live working and insulation coordination in the flowchart shown in Figure 6.1. This flowchart is followed to result in the required critical clearance for gaps occurring during maintenance on the 110 kV BRP busbar disconnector.

The flowchart proceeds from top to bottom, starting from the system overvoltage and ending with the required electrical clearance. The left column lists the actions performed at each step, while the right column shows the resulting quantity. At each step, a conversion factor is introduced that accounts for a specific aspect of the real-world situation, such as the statistical nature of switching overvoltages, the altitude of the installation, or the geometry of the air gap. These factors are multiplied together to progressively convert the 2% representative overvoltage into a required 50% breakdown voltage of an equivalent rod-plane gap. This rod-plane gap serves as a universal reference, because its breakdown voltage as a function of gap distance is well described by the CRIEPI equation (Eq. 2.6), which is used to yield the required electrical clearance. Each step of the flowchart is discussed in detail in the subsections below.

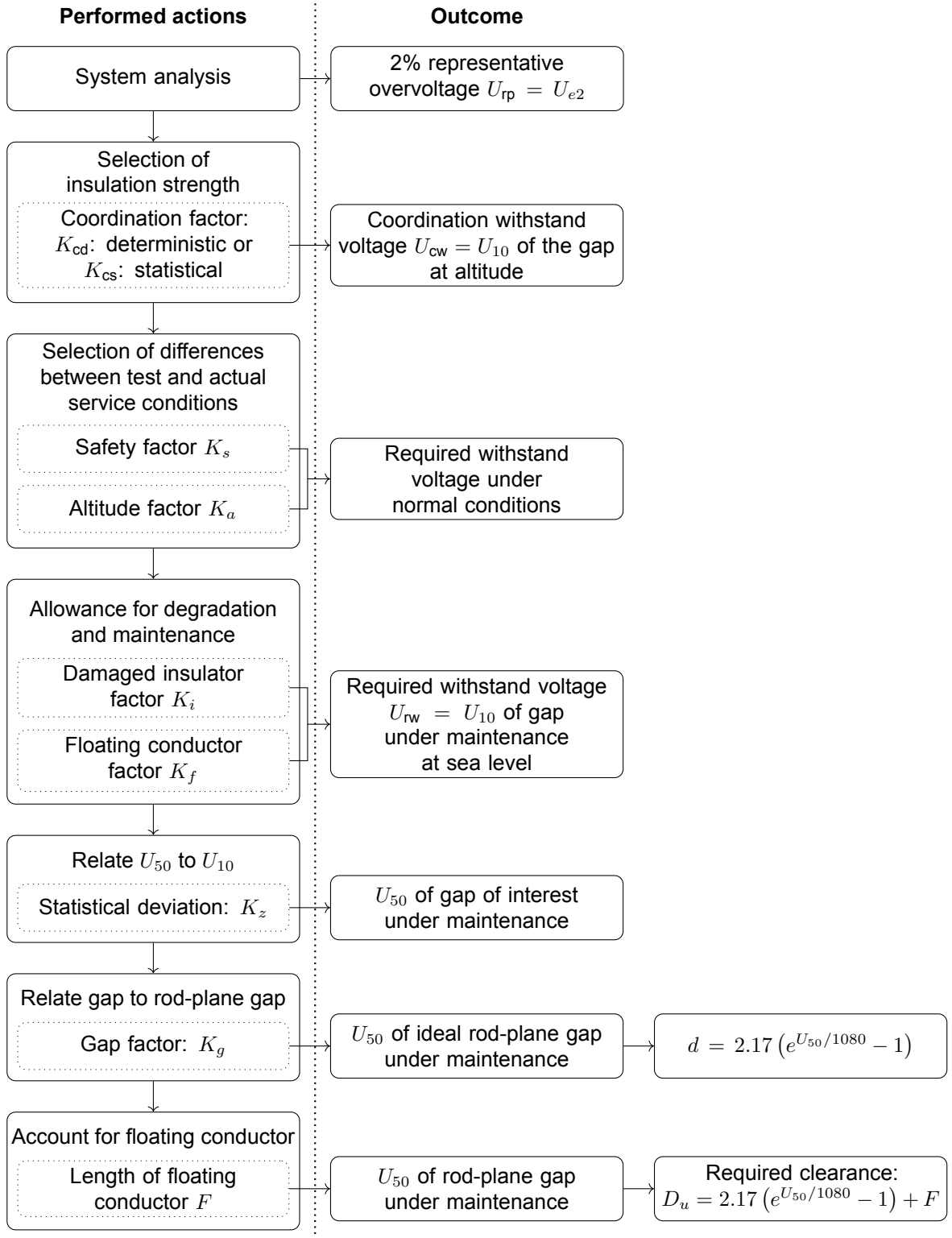

Figure 6.1: Flowchart to determine the electrical clearance, based on [6], [13], [14]

6.1.1. System analysis

Section 2.3 introduced a 2% representative overvoltage of 3.7 p.u. [19]. This overvoltage does not take into account the presence of surge arresters in the BRP. However, all the BRP substations will be equipped with surge arresters [11], limiting the magnitude of the overvoltage. The 110 kV BRP stations will be equipped with a V102 surge arrester [51], [52]. The maximum residual voltages at different

discharge currents for this surge arrester are listed in Table 6.1.

Table 6.1: Maximum residual voltage of the V102 surge arrester [52], given an overvoltage with a 30/60 µs wave shape

Discharge current (kA)	Maximum residual voltage (kV)
0.5	232
1	238
2	250

An incoming surge causes a surge current of:

$$I_{\text{surge}} = \frac{U}{Z} \tag{6.1}$$

where I_{surge} is the surge current in kA, U is the magnitude of the overvoltage in kV, and Z is the wave impedance. This wave impedance is typically $400\,\Omega$ for a single overhead conductor (to be found in a substation) and $300\,\Omega$ for a double overhead conductor (to be found in an overhead line). Overvoltages of 3.7 p.u. result in surge currents of 0.93 and 1.24 kA for $Z = 400$ and $300\ \Omega$, respectively. The aforementioned currents, together with the residual voltages from Table 6.1, are shown in Figure 6.2.

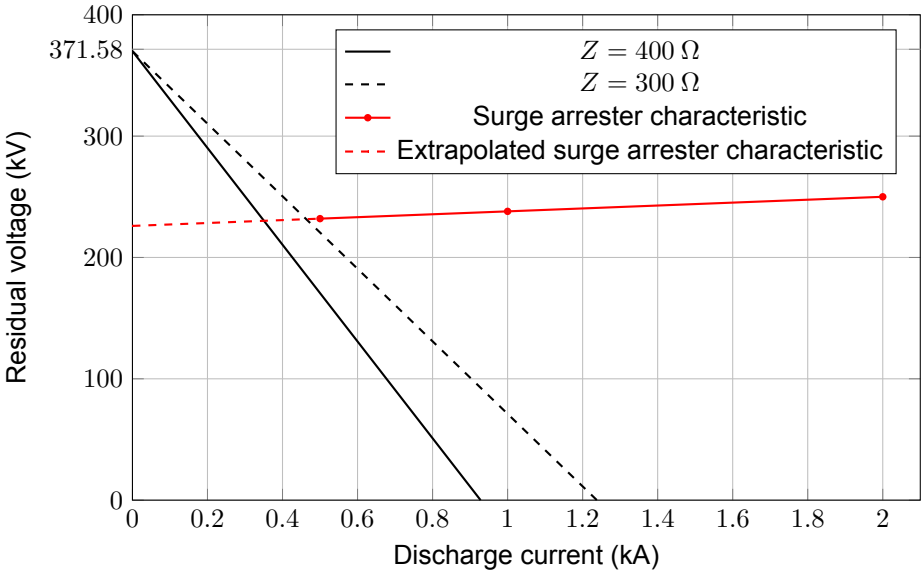

Figure 6.2: V102 surge arrester characteristic [52], together with the overvoltage and corresponding current

If the surge arrester characteristic is slightly extrapolated, the intersections with the surge characteristics can be determined. This results in residual voltages of 230.2 and 231.6 kV for the surge currents caused by an overvoltage of 3.7 p.u. for the $400\ \Omega$ and $300\ \Omega$ surge impedances. These residual voltages are taken to be the 50% and 2% representative overvoltage. The worst-case situation is in the case of a discharge current of 2 kA, when a residual voltage of 250 kV is present at the surge arrester. This is considered to be the maximum occurring residual voltage.

With this statistical information, a Weibull distribution can be fitted. A Weibull distribution is preferred over a normal distribution because it can be truncated at 0. Switching overvoltages typically truncate at 2 to 3 standard deviations above the mean overvoltage [53]. The 50% and 2% representative overvoltages result in the Weibull switching overvoltage distribution with parameters $k = 285.4$ and $\lambda = 230.48$ kV, and truncated at 3 standard deviations above the mean. This distribution is shown in Figure 6.3.

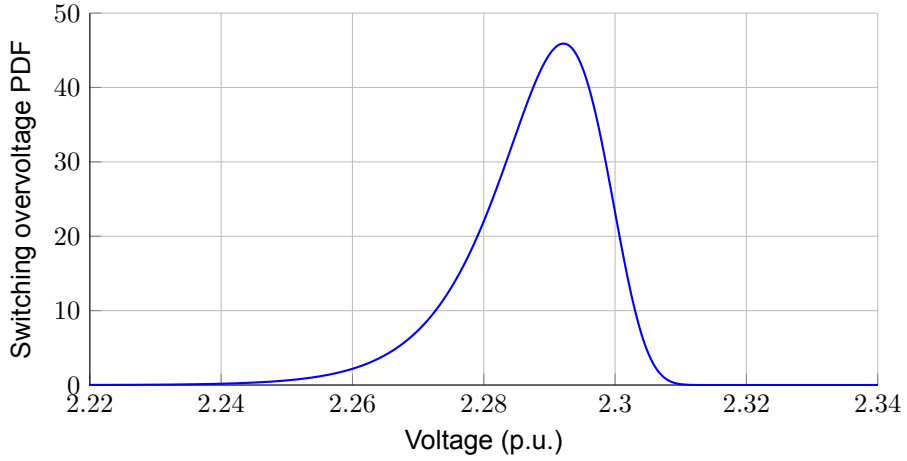

Figure 6.3: Weibull probability density function of the switching overvoltage

It can be seen that the switching overvoltage distribution is very narrow. This is because it was fitted to meet the residual voltages from the surge arresters under incoming switching surges. This distribution accurately represents overvoltages within a substation near and above its mean. It does not, however, accurately describe overvoltages below the mean.

This step results in:

$\rightarrow$ $\boldsymbol{U_{\text{rp}} = 2.3 \text{ p.u.} \approx 231.6 \text{ kV}}$

6.1.2. Selection of insulation strength

The next step is the selection of insulation strength. An extrapolation of Figure 6.4 indicates that the weakest gap at an overvoltage of $U = -231.6$ kV is the earthing contact-needle gap. Therefore, this gap is considered in the remainder of the clearance determination.

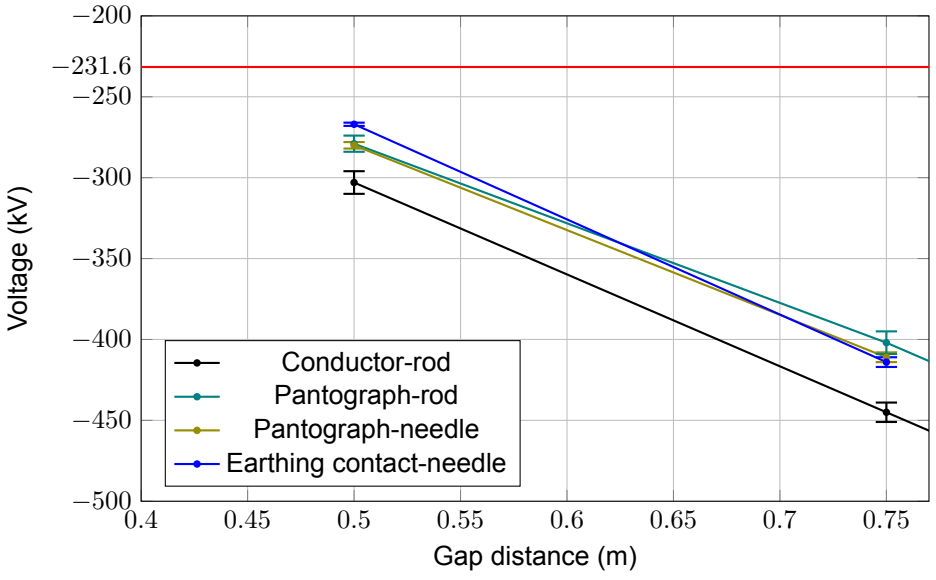

Figure 6.4: U_{10} of the disconnector gaps and the 2.3 p.u. switching overvoltage

A Weibull distribution is used for the breakdown probability of the air gap, truncating the breakdown probabilities at voltages more than 4 standard deviations below U_{50} [13].

This step requires parameter selection for one of the two following factors:

- The deterministic coordination factor K_{cd} is used for a worst-case analysis when there is no statistical information available about failure rates of the equipment.
- The statistical coordination factor K_{cs} is used when the risk of flashover is evaluated. Both the stress (distribution of switching overvoltages) and the strength (breakdown probability of the air gap) are taken into account.

Since both the probability distribution of switching overvoltages and the breakdown probability of the air gap are known, the statistical coordination factor is used. The purpose of selecting a statistical coordination factor is to limit the probability of flashover during switching overvoltages.

The risk density is obtained by multiplying the probability density function of the switching overvoltage by the cumulative density function of the flashovers. Integrating the risk density yields the risk probability, i.e., the probability that a breakdown occurs given a switching overvoltage drawn from the distribution specified earlier. By extrapolation of the earthing contact-needle gap to $U_{\text{rp}} = -231.6$ kV, a clearance of 43.9 cm is found. The extrapolated flashover probability function for this gap distance is shown together with the switching overvoltage distribution in Figure 6.5, leading to a risk probability of 0.072.

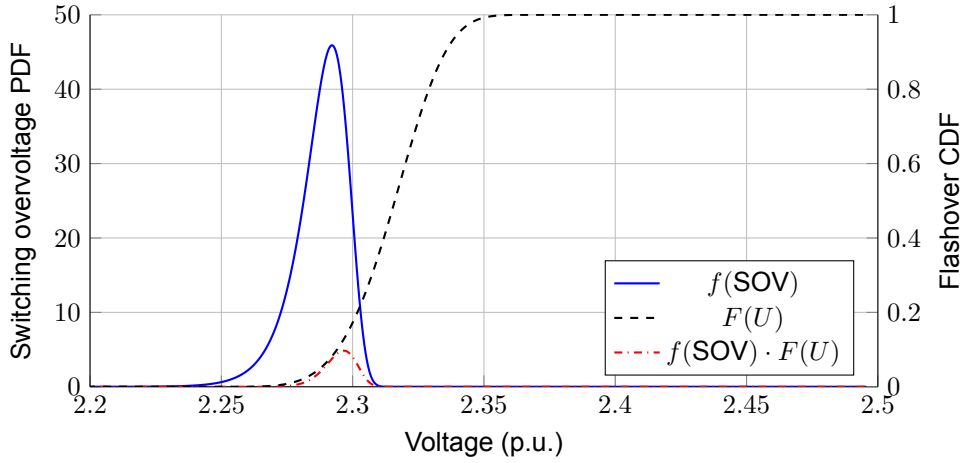

Figure 6.5: PDF of the switching overvoltage, CDF of the flashover probability and the resulting risk density for a 43.9 cm earthing contact-needle gap under negative stresses, $U_{\text{rp}} = 2.3$ p.u. and $K_{\text{cs}} = 1.0$

Figure 6.6 shows the risk as a function of the coordination factor K_{cs}. It can be seen that the risk decreases rapidly when increasing the coordination factor.

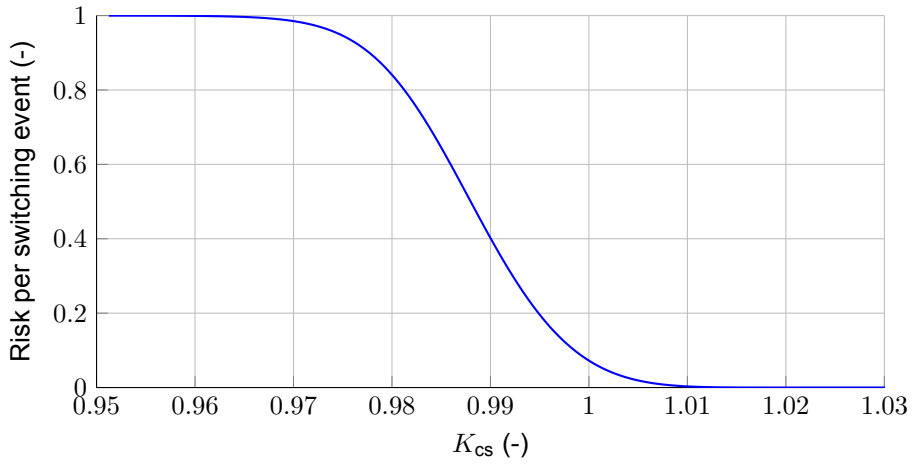

Figure 6.6: Risk as a function of the coordination factor

The upper bound of individual risk of a fatal accident in the Netherlands for new installations is 10^{-6} yr^{-1}, where the 'as low as reasonably achievable' (ALARA) principle is applied [54]. The risk probability obtained through the integral of the risk density is the risk per switching action. From October 2024 until October 2025, TenneT reported 269 measured switching events at a substation considered prone to switching events [20]. To stay on the conservative side, it is assumed that there are 500 switching events per year. This leads to a maximum acceptable risk per switching event of $\frac{10^{-6}\ \text{yr}^{-1}}{500\ \text{events yr}^{-1}} = 2 \times 10^{-9}$.

The found risk probability from Figure 6.5 is considerably higher than this maximum acceptable risk per switching event. Therefore K_{cs} is set to 1.025, reducing the risk per switching event to 3.1×10^{-10}. This is shown in Figure 6.7

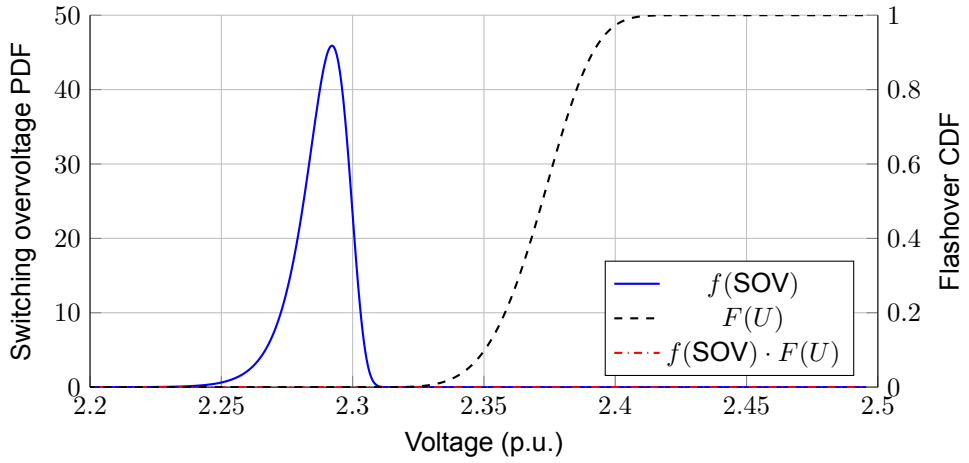

Figure 6.7: PDF of the switching overvoltage, CDF of the flashover probability and the resulting risk density for a 43.9 cm earthing contact-needle gap under negative stresses, $U_{\text{rp}} = 2.3$ p.u. and $K_{\text{cs}} = 1.024$

.

This step in the flowchart results in:

$\rightarrow$ $\boldsymbol{K_{\text{cs}} = 1.025}$

$\rightarrow$ $\boldsymbol{U_{\text{cw}} = U_{\text{rp}} \cdot K_{\text{cs}} = 2.35}$ **p.u.** $\boldsymbol{\approx 236.0}$ **kV**

6.1.3. Selection of differences between test and actual service conditions

This step consists of two factors that need to be specified:

- The safety factor K_s makes the distinction between self-restoring and non-self-restoring insulation. Normally, air insulation is self-restoring, however, in the case of safety clearances, it can be characterised as non-self-restoring. For self-restoring insulation, $K_s = 1.05$ is used, and for non-self-restoring insulation, $K_s = 1.15$. Since the statistical coordination factor K_{cs} is used to minimise the risk of sparkover below a certain value, $K_s = 1.0$.
- The altitude factor K_a accounts for the effect of air density on the breakdown strength of air gaps. The average altitude in the European Netherlands is around 30 meters above sea level [15], which results in an atmospheric factor of $K_a = 1$. If the highest part of the European Netherlands is taken (around 300 m above sea level [16]), this atmospheric factor changes to $K_a \approx 1.036$. Therefore, the atmospheric factor of $K_a = 1.036$ is used.

$\rightarrow$ $\boldsymbol{K_s = 1.0}$

$\rightarrow$ $\boldsymbol{K_a = 1.036}$

$\rightarrow$ $\boldsymbol{U_{\text{rw, normal conditions}} = U_{\text{cw}} \cdot K_s \cdot K_a = 2.43}$ **p.u.** $\boldsymbol{\approx 244.5}$ **kV**

6.1.4. Allowance for degradation and maintenance

To account for the degradation of the insulator and maintenance operations, there are two factors of importance:

- The damaged insulator factor K_i takes into account working next to damaged insulators. Its value is based on the length of undamaged insulators (A_o), length of damaged insulators (A_d) and a coefficient related to the material of the insulator ($K_d = 1$ for toughened glass insulators, $K_d = 0$ to 1 for porcelain insulators, and $k_d = 1.25$ for composite insulators). This results in $K_i = 1 - 0.8k_d(A_d/A_o)$. Damaged insulators are not considered, resulting in $K_i = 1.0$.
- The floating conductor factor K_f accounts for conductors at floating potential in the air gap, as they influence the strength of the gap. Determining their influence is more elaborate, see [6, Sec. 4.3.2.4]. This work does not consider floating conductors, resulting in $K_f = 1.0$.

$\rightarrow$ $\boldsymbol{K_i = 1.0}$

$\rightarrow$ $\boldsymbol{K_f = 1.0}$

$\rightarrow$ $\boldsymbol{U_{\text{rw, maintenance conditions}} = U_{\text{rw, normal conditions}} \cdot K_i \cdot K_f = 2.43}$ **p.u.** $\boldsymbol{\approx 244.5}$ **kV**

6.1.5. Relating U_{50} to U_{10}

To relate the 50% breakdown voltage of the gap to the 10% breakdown voltage, the standard deviation σ is used: $U_{50} = U_{10}/(1 - 1.28\sigma)$, and the statistical factor is $K_z = 1/(1 - 1.28\sigma)$. IEC 61472 [6] suggests $\sigma = 5\%$, IEC 60071-2 [13] suggests $\sigma = 6\%$, and Hileman [17] suggests $\sigma = 7\%$. Tests on the conductor-rod gap (Table 4.9) and on the pantograph-rod gap (Table 5.7) show that σ can be as high as 7%. Therefore, if the standard deviation is not known from tests, it is proposed to use $\sigma = 7\%$ to be conservative. For the weakest gap in this work (the earthing contact-needle gap), the standard deviation is known from tests and is $\sigma = 1\%$.

$\rightarrow$ $\boldsymbol{K_z = 1.098}$ **if** $\boldsymbol{\sigma}$ **is not known from tests**

$\rightarrow$ $\boldsymbol{K_z = 1.013}$ **for the earthing contact-needle gap**

$\rightarrow$ $\boldsymbol{U_{50,\text{ maintenance conditions}} = U_{\text{rw, maintenance conditions}} \cdot K_z = 2.47}$ **p.u.** $\boldsymbol{\approx 247.7}$ **kV**

6.1.6. Relating the gap of interest to the rod-plane gap

The breakdown strength of the gap of interest can be expressed as a scalar factor times the breakdown strength of the rod-plane gap, the gap factor. The CRIEPI equation (Eq. 2.6) is found to be a good and conservative fit for the breakdown voltages of the rod-plane gap (see Sec. 4.3.4), the gap factors in this section are based on this equation (and not on the experimental rod-plane or needle-plane results). The minimum gap factor resulting from the tests in this work is $K_g = 1.20$ for the earthing contact-needle gap (Table 5.14). This gap factor is higher than the currently used gap factor of $K_g = 1.10$ for safety clearance determination [11]. If the gap factor is known from tests, this gap factor should be used (with respect to the rod-plane strength from the CRIEPI equation), if this is not the case, the currently used conservative value of 1.10 is proposed.

$\rightarrow$ $\boldsymbol{K_g = 1.10}$ **if** $\boldsymbol{K_g}$ **is not known from tests**

$\rightarrow$ $\boldsymbol{K_g = 1.20}$ **for the earthing contact-needle gap**

$\rightarrow$ $\boldsymbol{U_{50,\text{ ideal rod-plane}} = U_{50,\text{ maintenance conditions}}/K_g = 2.06}$ **p.u.** $\boldsymbol{\approx 206.4}$ **kV**

With this $U_{50,\text{ ideal rod-plane}}$, the clearance of the ideal rod-plane gap can be calculated using the CRIEPI equation as: $d = 2.17\left(e^{U_{50}/1080} - 1\right)$.

6.1.7. Floating conductor

The last step is to account for the length of the floating conductor. This length gets added to the clearance of the ideal rod-plane gap. Floating conductors are not considered in this work, leading to $F = 0$ m.

$\rightarrow$ $\boldsymbol{F = 0}$ **m**

6.1.8. Clearance determination

The final clearance determination is performed with the 50% breakdown voltage of the rod-plane gap based on the CRIEPI equation, and the length of floating conductors is added. This results in Equation 6.2.

$$D_u = 2.17 \left(e^{U_{50}/1080} - 1 \right) + F \tag{6.2}$$

The minimum electrical safety clearance around the 110 kV busbar disconnector is therefore:

$$D_u = 2.17 \left(e^{206.4/1080} - 1 \right) + 0 = 0.456 \text{ m} \tag{6.3}$$

The calculated safety distance is based on a worst-case scenario. In practice, the actual risk will be lower because [6]:

- The actual system voltage is not always at a maximum value
- The location where the work is performed is not always the location where the switching overvoltage is at a maximum value
- Not all switching overvoltages have a critical time-to-crest
- Work is generally not performed when there will be switching operations

Figure 6.8: Mannequin placed deliberately too close to the busbar disconnector with an applied switching impulse

6.2. Electromagnetic fields

Power-frequency electromagnetic fields can have direct effects on the human body. They may induce small currents which stimulate the nerves, potentially causing tingling, pain, uncontrolled muscle contractions, disturbances of the heart rhythm, or visual stimulations, such as light flashes [55]. Therefore, it is of great importance that the maximum allowed field strengths are well set and adhered to. The EU directive 2013/35/EU [56] describes the minimum health and safety requirements regarding the electromagnetic fields for workers. This directive describes different exposure levels for fields, based on different levels (at power-frequency):

- Exposure limit values (ELV): internal electric field limits (inside the human body), related to the effects on the human body. For $f > 1$ Hz, the exposure to magnetic fields is assessed through the induced internal electric field. Compliance can be verified using action levels (see below).
  - Sensory effect ELV: related to effects on the central nervous system in the head.
  - Health effect ELV: related to electric stimulation of all peripheral and central nervous system tissues in the body.

Table 6.2: Sensory and health effects ELV at $f = 50$ Hz [56]

	E-field (V/m)
Sensory effects ELV	$0.0028f = 0.14$
Health effects ELV	1.1

- Action levels (AL): external electric and magnetic field limits, related to the internal electric field they will cause:
  - Low AL: based on limiting the internal electric field below the ELVs.
  - Below high AL: internal electric field does not exceed the ELVs, provided protection measures are taken.
  - Exposure of limbs to a localised magnetic field is allowed for higher field strengths.

Table 6.3: Action levels at $f = 50$ Hz [56]

	E-field (V/m)	**B-field (μT)**
Low AL	$5.0 \times 10^5/f = 1.0 \times 10^4$	1.0×10^3
High AL	2.0×10^4	$3.0 \times 10^5/f = 6.0 \times 10^3$
Exposure of limbs to a localised magnetic field		$9.0 \times 10^5/f = 1.8 \times 10^4$

Summarising, it is allowed to perform work in an electric field that is below the high AL, provided that adequate measures have been taken and that the internal electric field does not exceed the health effects ELV. Adequate measures include, for instance, the informing and training of workers, the use of technical means, and personal protection [56].

A simulation of the three-phase busbar disconnector at operating voltage ($U = 123\sqrt{2/3} \approx 100$ kV_{peak}) is performed to analyse the electric field around the disconnector. The electric field is analysed along the 3 planes shown in Figure 6.9. The planes are placed at such a distance that the high action levels are observed. Figure 5.2 shows the 3D model that is used to analyse the electric field.

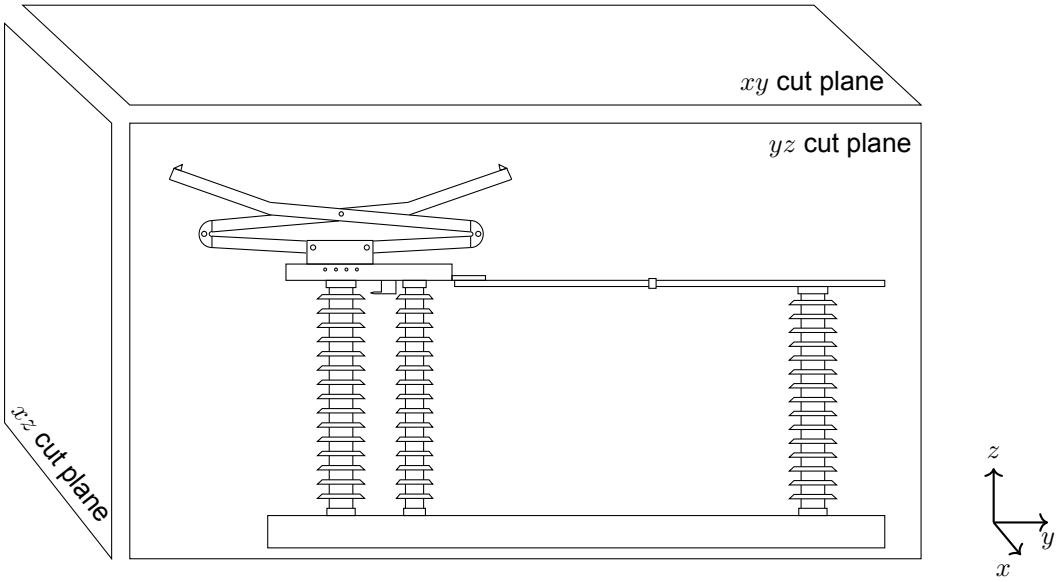

Figure 6.9: Illustration of the cut planes to analyse the electric field. In the simulation, the three-phase model of the busbar disconnector is used (see Fig. 5.2).

The electric field simulation yielded the results listed in Table 6.4.

Table 6.4: Minimum plane approach distances related to the highest E-field action level

Plane	E-field (V/m)	Distance of plane to disconnector (m)
xy	2×10^4	0.95
xz		0.80
yz		0.68

As the magnetic field is highly dependent on the substation configuration and varies with load, the safety distances associated with it are outside the scope of this thesis. However, a rough estimate is made as follows:

The magnetic field caused by a current through an infinitesimally thin wire is defined as

$$B = \frac{\mu_0 I}{2\pi R} \tag{6.4}$$

where $\mu_0 = 4\pi \times 10^{-7}$ H/m, I is the maximum busbar current of 3150 A, and R the perpendicular distance from the wire in meters. Equating this equation to the low action level of 1.0 mT (see Table 6.3) leads to a distance of 63 cm. The high action value is reached at a distance of 10.5 cm.

The distance at which the high action value is reached is significantly lower than the clearance that is needed based on the electrical field. The magnetic field is therefore not considered to be a limiting factor for safety clearances in the BRP busbar disconnector.

7 Discussion

This chapter discusses and interprets the findings of this work.

7.1. Validation of the method of Schneider and Weck

The COMSOL simulations reproduce the original results of Schneider and Weck [7] reasonably well for gap distances of $d > 2$ m, with deviations below 5%. This indicates that the simulation in COMSOL is consistent with the original experiments performed in an electrolytic tank.

For shorter gaps ($d < 2$ m), however, the method shows inconsistent behaviour. Sudden changes in the gap factor were observed for the simulated gap factor of the conductor-rod gap, suggesting the invalidity of this method. Experimental results on the conductor-rod gap show significant deviations from the simulated gap factors. Therefore, the method of Schneider and Weck cannot be considered valid for geometries with gap distances below 2 m.

7.2. Breakdowns in air gaps

The results of the rod-plane and needle-plane gap are in line with literature results. However, their breakdown strengths are not equal, contrary to what would be expected based on the theory of the critical radius. This critical radius is not researched for small gaps ($d < 2$ m), and extrapolation leads to incorrect results.

The equations describing the breakdown strength of a rod-plane gap were compared to the experimental results. The Paris equation (Eq. 2.4) consistently overestimates the breakdown strength. The Feser equation (Eq. 2.7) describes the experimental results the best, as this equation is specifically tailored for small gaps ($0.4 \leq d \leq 3$ m). The CRIEPI and Gallet equations (Eqs. 2.6 and 2.5, resp.) underestimate the gap strength by around 20 and 30%, respectively. The deviations from the experimental results can be explained by two main reasons. The first reason is that the applied impulses were not always exactly of the same shape (time-to-crest and time-to-half) as the equations were developed for. The second reason is that the Paris, Gallet, and CRIEPI equations are valid for a large range of gap lengths (Paris: $2 < d < 6$ m, Gallet: $1 < d < 21$ m, and CRIEPI: $0.5 < d < 12$ m) and need to perform reasonably well for all gap distances in this range. The Paris and Gallet equations are shown to be not valid outside their validity range.

The breakdown strength of a gap under positive impulse stresses is usually lower than under negative stresses. This turns around when the (positive) gap factor exceeds 1.5 [10]. However, this is not observed for the pure conductor-rod gaps and the pantograph-rod gaps. The positive gap factors are 1.33 and 1.28, respectively, but the gaps are stronger under positive impulses than under negative impulses. This could be caused by the short gaps considered in this work, contrary to the literature, which mostly deals with long gaps. The gap factors found for the conductor-rod gap are in line with the literature, as well as the ratio between positive and negative breakdown strength.

The conductor-rod gap in the BRP busbar disconnector has a 50% breakdown voltage close to the 50%

breakdown voltage of the pure conductor-rod gap for gap distances of 0.75 and 1 m. For a gap distance of 0.5 m, the spacer between the two conductors is likely to have a large effect on the electric field distribution, resulting in a lower breakdown strength. This effect decreases as the gap distance increases. This is also observed for the pantograph-rod and pantograph-needle gaps, where the pantograph-rod has a higher breakdown strength than the pantograph-needle at 0.5 m, but at 0.75 m they are virtually equal.

The COMSOL simulation of the BRP busbar disconnector showed the highest electric field strength at the tip of the pantograph, followed by the fixed contact of the earthing mechanism. Tests have shown that, contrary to what is to be expected based on the simulations, the earthing contact-needle gap has a lower breakdown strength than the pantograph-needle gap. This can be explained by the way the simulation is performed: not all details (bolts, nuts, etc.) were included in this simulation. During testing, all sparkovers occurred towards a bolt located close to the earthing contact, indicating that the local electric field enhancement dominated the breakdown behaviour.

7.3. Implications for safety clearances

The rod-plane experiments showed that the CRIEPI equation consistently underestimates the strength of the gap. Therefore, this equation is recommended to be used for safety clearances, as it will overcome differences in results between different laboratories and still be conservative.
Experiments on the BRP busbar disconnector led to gap factors for four different gaps. The earthing contact-needle gap has the lowest breakdown strength amongst the four studied gaps, resulting in a gap factor of 1.05 with respect to the experimentally found rod-plane strength. As the CRIEPI equation is preferred as a reference, the gap factor for the earthing contact-needle gap with respect to this equation is 1.20. The currently used gap factor for determining clearances is 1.1 [11]. The use of the gap factor of 1.1 is recommended in combination with the CRIEPI equation to remain conservative.

This work led to the minimum electrical clearance of the BRP busbar disconnector of 45.6 cm. This is in the same order of magnitude as the currently by TenneT defined 47.9 cm. The main reason for this difference is that the clearance in this work is based on the surge arrester characteristics, leading to a switching overvoltage distribution with a very low standard deviation, resulting in a relatively low 2% representative overvoltage. The found safety distance is a worst-case scenario, as several conservative assumptions were made.

The observed standard deviations for the investigated gaps indicate that $1\% < \sigma < 7\%$. If the U_{10} is derived from the U_{50}, with σ being unknown, it is proposed to use $\sigma = 7\%$ to remain conservative.

Next to the electrical safety clearances, the clearance related to the electric field was investigated. This was studied using the same COMSOL model as before. This has the shortcoming that details (bolts, nuts, etc.) are not included in the simulation, which could lead to changes in the found safety distance. These changes are expected to be limited, as these details are rather small in size, and will therefore only have a limited influence on the electric field strength at a distance of approximately 70 cm. Taking into account the total risk for a flashover, this can increase based on the assumptions made (e.g. the normal distribution of the overvoltage).

7.4. Calculating the safety clearances

Based on the findings of this work, the following procedure is recommended for calculating the breakdown strength of gaps in 110 kV substations. First, the breakdown strength of the rod-plane gap should be described using the CRIEPI equation (Eq. 2.6), as this consistently underestimates the experimental results and therefore provides a conservative reference. Second, the gap factor of the specific geometry should be determined experimentally if possible. If no experimental data is available, the conservative value of $k_g = 1.1$ should be used. Third, when deriving U_{10} from U_{50}, a standard deviation of $\sigma = 7\%$ should be assumed if not known from tests. Together, these three steps provide a consistent and conservative basis for calculating the breakdown strength of gaps encountered during maintenance on compact 110 kV substations.

8

Conclusion & Recommendations

This chapter presents a conclusion and proposes recommendations based on the current work.

8.1. Conclusion

This work investigated safety clearances in the compact and modular 110 kV BRP busbar disconnector that TenneT is currently placing in the Netherlands. The objective was to determine gap factors that are found during maintenance and to validate a method to simulate these gap factors. This objective has been met by performing both simulations and laboratory experiments.

The method of simulating the gap factor of Schneider and Weck was investigated. A COMSOL simulation reproduced the original results from the electrolytic tank for large gaps. However, for small and simple gaps ($d < 2$ m), this method fails to model the gap factor accurately.

The experiments led to the 50% breakdown voltages of different gap configurations. The Feser equation best represents short rod-plane gaps, but the CRIEPI equation should be used for clearance determination to remain conservative. There is a large difference between the experimental results and the breakdown equations when they are extrapolated outside their validity range. The experiments on the busbar disconnector show that negative polarity impulses have a lower breakdown strength than positive polarity impulses. It is therefore not sufficient to only consider positive or negative impulse strength for clearance determination.

The found gap factors were in line with results from literature, and the currently used gap factor of $k_g = 1.1$ for clearance determination is conservative enough when being used in combination with the CRIEPI equation. The experiments show that the gap factor can be as low as $k_g = 1.20$ for the gap between the earthing contact and a needle.

The experimental results led to a critical electrical clearance of $D_U = 45.6$ cm. Therefore, the currently enforced critical clearances by TenneT of $D_U = 47.9$ cm and $D_L = 50$ cm are considered to be adequate. A simulation showed that the minimum safety clearance regarding the electric field is approximately 68 cm.

8.2. Recommendations

Based on the findings of this work, the following recommendations are proposed:

- Maintain the currently used live working zone $D_L = 50$ cm.
- Perform both positive and negative impulse testing when determining critical breakdown voltages for safety clearances.
- Maintain the currently used gap factor of 1.1 in combination with the CRIEPI equation.
- If the standard deviation σ is not known from tests, use $\sigma = 7\%$ when deriving U_{10} from U_{50} for determining clearances.
- The breakdown equations are only to be used inside their validity ranges.

8.3. Future work

To build on the results of this work, the following directions for future research are recommended:

- The 2% representative overvoltage for 110 kV grids is not uniquely defined, but has a large influence on the clearance determination. Future research could investigate what overvoltage best represents switching actions in the 110 kV grids.
- In this study, a critical time-to-crest of 100 µs is assumed for all gap configurations. However, this value may vary depending on the gap geometry. Future research could therefore investigate the critical time-to-crest for different gaps and the resulting implications on safety clearances.
- The concept of the critical radius is not defined for gaps with a gap distance below 2 m. This limitation could be investigated experimentally using different rod radii and gap distances.
- Although the method of Schneider and Weck does not apply to small gaps ($d < 2$ m), it may be worth exploring whether an alternative model can be developed to accurately simulate gap factors for small gaps.

References

[1] Compendium voor de Leefomgeving (CLO). “Aanbod en verbruik van elektriciteit, 1990-2024.” (in Dutch), Accessed: Jan. 19, 2026. [Online]. Available: www.clo.nl/nl002029.

[2] Netbeheer Nederland. “Het energiesysteem van de toekomst: de II3050-scenario’s.” (in Dutch), Accessed: Jan. 20, 2026. [Online]. Available: www.netbeheernederland.nl/publicatie/rapport-ii3050-scenarios.

[3] Centraal Bureau voor de Statistiek (CBS). “Datacenters verbruiken 4,6 procent van de elektriciteit.” (in Dutch), Accessed: Apr. 13, 2026. [Online]. Available: www.cbs.nl/nl-nl/nieuws/2025/51/datacenters-verbruiken-4-6-procent-van-de-elektriciteit.

[4] TenneT. “Net op land, ontwerp investeringsplan 2026.” (in Dutch), Accessed: Jan. 20, 2026. [Online]. Available: www.tennet.eu/nl/over-tennet/publicaties/investeringsplannen.

[5] A. Lathouwers, P. Jansen, and E. de Meulemeester, “TenneT’s giant leap to be able to replace 140 substations within next 10 year, while in service and coming from different lay-outs,” in *Proc. CIGRE Paris Session 2020*, B3-104, 2020.

[6] IEC 61472:2013, *Live working - Minimum approach distances for a.c. systems in the voltage range 72,5 kV to 800 kV - A method of calculation*.

[7] K. H. Schneider and K. H. Weck, “Parameters influencing the gap factor,” *Electra*, no. 35, pp. 25–45, 1974.

[8] EN 50110-1:2023, *Operation of electrical installations - Part 1: General requirements*.

[9] I. Tannemaat, “Bay Replacement Program, review insulation coordination and standardisation proposition,” TenneT, Tech. Rep. AMT-PU 21-207 v1.1, Feb. 2022.

[10] IEC 60071-1:2019, *Insulation co-ordination - Part 1: Definitions, principles and rules*.

[11] I. Tannemaat and C. S. Engelbrecht, “Air clearances for project ’Veldvervanging’,” TenneT, Tech. Rep. AM-AST-SST 17-163, Apr. 2017.

[12] NEN 3840:2011+A3:2019, *Bedrijfsvoering van elektrische installaties - Hoogspanning*, (in Dutch).

[13] IEC 60071-2:2023, *Insulation co-ordination - Part 2: Application guidelines*.

[14] I. Tannemaat and C. S. Engelbrecht, “Improved calculations for external clearances on overhead lines,” in *Proc. CIGRE Paris Session 2026*, B2-10288, unpublished, 2026.

[15] WorldData. “Netherlands: country data and statistics,” Accessed: Jun. 10, 2026. [Online]. Available: www.worlddata.info/europe/netherlands.

[16] Rijkswaterstaat. “Normaal Amsterdams Peil (NAP),” Accessed: Jun. 11, 2026. [Online]. Available: www.rijkswaterstaat.nl/zakelijk/open-data/normaal-amsterdams-peil.

[17] A. R. Hileman, *Insulation Coordination for Power Systems*. Boca Raton, FL, USA: Taylor & Francis Group, LLC, 1999. DOI: 10.1201/9781420052015.

[18] G. Le Roy, C. Gary, B. Hutzler, J. Lalot, and C. Dubanton, *Les propriétés diélectriques de l’air et des très hautes tensions*, (in French). Paris, France: Éditions Eyrolles, 1984.

[19] C. S. Engelbrecht, P. L. J. Hesen, C. S. Stuurman, I. Tannemaat, and E. P. Evertz, “Nota Isolatiecoördinatie voor 380, 220, 150, 110 en 50 kV elektriciteitsnetten in Nederland. Deel 2 – Technische onderbouwing,” (in Dutch), DNV KEMA, Tech. Rep. 74101904-ETD/POL 13-00068 V1.0, Jul. 2013.

[20] I. Tannemaat, K. Velitsikakis, S. Nauta, and J. McBride, “Results of continuous transient voltage measurement in the Dutch 110kV grid,” in *Proc. CIGRE Paris Session 2026*, C4-10305, unpublished, 2026.

[21] IEC 60060-1:2025, *High-voltage test techniques - Part 1: General terminology and test requirements*.

[22] L. Paris, “Influence of Air Gap Characteristics on Line-to-Ground Switching Surge Strength,” *IEEE Trans. Power App. Syst.*, vol. PAS-86, no. 8, pp. 936–947, Aug. 1967. DOI: 10.1109/TPAS.1967.291917.

[23] CIGRE Working Group 33.07, “TB 72: Guidelines for the evaluation of the dielectric strength of external insulation,” 1992.

[24] G. Gallet, M. Bettler, and G. Leroy, “Switching impulse results obtained on the outdoor testing area at Renardières,” *IEEE Trans. Power App. Syst.*, vol. PAS-95, no. 2, pp. 580–585, Mar./Apr. 1976. DOI: 10.1109/T-PAS.1976.32138.

[25] I. Kishizima, K. Matsumoto, and Y. Watanabe, “New Facilities for Phase-to-Phase Switching Impluse Tests and Some Test Results,” *IEEE Trans. Power App. Syst.*, vol. PAS-103, no. 6, pp. 1211–1216, Jun. 1984. DOI: 10.1109/TPAS.1984.318451.

[26] G. Gallet, G. Leroy, R. Lacey, and I. Kromer, “General expression for positive switching impulse strength valid up to extra long air gaps,” *IEEE Trans. Power App. Syst.*, vol. PAS-94, no. 6, pp. 1989–1993, Nov./Dec. 1975. DOI: 10.1109/T-PAS.1975.32045.

[27] K. Feser, “Mechanism to explain the switching impulse phenomena,” *Schweizerische Technische Zeitschrift*, no. 46, pp. 937–946, Nov. 1971.

[28] Les Renardières Group, “Negative discharges in long air gaps at Les Renardières. 1978 results,” *Electra*, no. 74, pp. 67–216, 1981.

[29] G. Carrara and L. Thione, “Switching surge strength of large air gaps: A physical approach,” *IEEE Trans. Power App. Syst.*, vol. PAS-95, no. 2, pp. 512–524, Mar./Apr. 1976. DOI: 10.1109/T-PAS.1976.32131.

[30] L. Thione, “The dielectric strength of large air insulation,” in *Proc. Brown Boveri Symp. Surges High-Voltage Netw.*, Sep. 1979, pp. 164–205.

[31] Les Renardières Group, “Positive discharges in long air gaps at Les Renardières. 1975 results and conclusions,” *Electra*, no. 53, pp. 31–153, 1977.

[32] L. Paris and R. Cortina, “Switching and Lightning Impulse Discharge Characteristics of Large Air Gaps and Long Insulator Strings,” *IEEE Trans. Power App. Syst.*, vol. PAS-87, no. 4, pp. 947–957, Apr. 1968. DOI: 10.1109/TPAS.1968.292069.

[33] L. Paris, A. Taschini, K. H. Schneider, and K. H. Weck, “Phase-to-ground and phase-to-phase air clearances in substations,” *Electra*, no. 29, pp. 29–44, 1973.

[34] V. Cooray, *An Introduction to Lightning*. Dordrecht, The Netherlands: Springer, 2014. DOI: 10.1007/978-94-017-8938-7.

[35] G. Gela, “Air gap sparkover and gap factors,” EPRI, Tech. Rep. TR-104437, Dec. 1994.

[36] G. Gela, “Sparkover Performance and Gap Factors of Air Gaps Below 1 Meter,” EPRI, Tech. Rep. TR-106335, Mar. 1998.

[37] D. E. Gourgoulis, P. N. Mikropoulos, C. A. Stassinopoulos, and C. Yakinthos, “Behaviour of positive conductor–rod gaps stressed by impulse voltages in atmospheric air,” *IEE Proc.-Sci. Meas. Technol.*, vol. 144, no. 5, pp. 29–44, Sep. 1997. DOI: 10.1049/IP-SMT:19971250.

[38] L. Buono, F. Di Bona, and F. Palone, “Switching Impulse Withstand of HVDC Overhead Lines in Italy: gap factor and clearance evaluation,” in *Proc. AEIT HVDC Int. Conf.*, May 2025. DOI: 10.1109/AEITHVDC66044.2025.11079489.

[39] IEC 60060-2:2025, *High-voltage test techniques - Part 2: Measuring systems*.

[40] W. C. Guyker, A. R. Hileman, and J. F. Wittibschlager, “Full-Scale Tests for the Allegheny Power System 500-kV Tower-Insulation System,” *IEEE Trans. Power App. Syst.*, vol. PAS-85, no. 6, pp. 614–623, Jun. 1966. DOI: 10.1109/TPAS.1966.291597.

[41] G. W. Brown, “Method of Maximum Likelihood Applied to the Analysis of Flashover Data,” *IEEE Trans. Power App. Syst.*, vol. PAS-88, no. 12, pp. 1823–1830, Dec. 1969. DOI: 10.1109/TPAS.1969.292298.

[42] The MathWorks Inc. “binofit - Binomial parameter estimates,” Accessed: Feb. 25, 2026. [Online]. Available: www.mathworks.com/help/stats/binofit.html.

[43] C. J. Clopper and E. S. Pearson, “The Use of Confidence or Fiducial Limits Illustrated in the Case of the Binomial,” *Biometrika*, vol. 26, no. 4, pp. 404–413, Dec. 1934. DOI: 10.2307/2331986.

[44] CIGRE Working Group D1.50, “TB 888: Atmospheric and altitude correction factors for air gaps and clean insulators,” 2023.

[45] L. Arevalo, D. Wu, and M. Larsson, “Air Humidity Factor for External Insulation Under Positive Switching Impulses - Revisited,” in *Proc. 21st Int. Symp. High Voltage Eng.*, Oct. 2019, pp. 784–794. DOI: 10.1007/978-3-030-31680-8_76.

[46] E. Lemke, “Der Durchslag im inhomogenen Feld in Luft bei Schaltspannungen,” (in German), *Period. Polytech. Elect. Eng.*, vol. 11, no. 3, pp. 229–239, Jan. 1967.

[47] I. Gallimberti, “The mechanism of the long spark formation,” *J. Phys. Colloq.*, vol. 44, no. C7, pp. 193–250, Jul. 1979. DOI: 10.1051/jphyscol:19797440.

[48] W. Hauschild and E. Lemke, *High-Voltage Test and Measuring Techniques*, 2nd ed. Cham, Switzerland: Springer, 2019. DOI: 10.1007/978-3-319-97460-6.

[49] R. Zhu et al., “Analysis of Positive and Negative Lightning Impulse Discharge Characteristics in Long Air Gaps,” *Energies*, vol. 18, no. 21, Oct. 2025. DOI: 10.3390/en18215746.

[50] J. R. Taylor, *An Introduction to Error Analysis*, 2nd ed. Sausalito, CA, USA: University Science Books, 1997.

[51] “Technical Specification Surge Arresters,” TenneT, Tech. Rep. DAT.01.421-NL, Feb. 2025.

[52] Siemens Energy, “V102 Surge Arrester Pass,” TenneT, Tech. Rep. V102_s_27189866.0300, Feb. 2026.

[53] *EPRI AC Transmission Line Reference Book - 200 kV and Above*, 3rd ed. Palo Alto, CA, 2005.

[54] I. Häring, *Risk Analysis and Management: Engineering Resilience*, 1st ed. Singapore: Springer, 2015. DOI: 10.1007/978-981-10-0015-7.

[55] Kennisplatform elektromagnetische velden. “Elektromagnetische velden en gezondheid.” (in Dutch), Accessed: Apr. 8, 2026. [Online]. Available: www.kennisplatform.nl/elektromagnetische-velden-en-gezondheid/.

[56] European Parliament and Council of the European Union, “Directive 2013/35/EU of the European Parliament and of the Council of 26 June 2013 on the minimum health and safety requirements regarding the exposure of workers to the risks arising from physical agents (electromagnetic fields),” *Official Journal of the European Union*, vol. L 179, no. 56, pp. 1–21, Jun. 2013.

A

Simulation results

This appendix includes all the simulation results from Section 3.1 and compares them to literature [17], and the paper of Schneider and Weck introducing the simulation method [7].

Table A.1: Simulated gap factor compared to literature

	Gap factor k_g (-)							
	Rod-plane				Rod-rod			
d (m)	COMSOL	COMSOL normalised	[17]	[7]	COMSOL	COMSOL normalised	[17]	[7]
0.25	1.083	1						
0.5	1.059	1			1.352	1.276		
0.75	1.055	1						
1	1.052	1			1.355	1.288		
2	1.047	1	1	1	1.308	1.249	1.25 to 1.35	1.27
4	1.038	1		1	1.217	1.172		1.21
6	0.991	1		1	1.163	1.173		1.14

	Conductor-plane				Conductor - 2m rod			
d (m)	COMSOL	COMSOL normalised	[17]	[7]	COMSOL	COMSOL normalised	[17]	[7]
0.25	1.282	1.185			1.437	1.327		
0.5	1.233	1.164			1.558	1.471		
0.75	1.215	1.142			1.585	1.502		
1	1.201	1.141			1.584	1.505		
2	1.189	1.135	1.15	1.08	1.530	1.461	1.4 to 1.6	1.47
4	1.188	1.144		1.14	1.438	1.385		1.40
6	1.202	1.212		1.15	1.376	1.388		1.25

	Conductor - 4m rod			
d (m)	COMSOL	COMSOL normalised	[17]	[7]
0.25	1.460	1.348		
0.5	1.606	1.516		
0.75	1.653	1.566		
1	1.666	1.583		
2	1.646	1.572	1.4 to 1.6	1.55
4	1.569	1.511		1.54
6	1.352	1.364		1.40

B

Experimental results

This appendix lists the experimental results of all the performed tests. It includes the measured peak voltage of the applied impulse, the number of breakdowns and the total number of applied impulses. The shown voltages are corrected to reference atmospheric conditions. The actual atmospheric conditions are listed.

B.1. Rod - plane

Table B.1: Experimental results, rod-plane 0.5m + Atmospheric conditions: $t = 17.75$ °C, $p = 995.71$ hPa, $h = 3.86$ g/m^3

Voltage (kV)	# breakdowns	# impulses
270.8	0	1
273.4	1	3
276.6	2	5
278.9	4	8
281.9	4	9
284.9	5	5

Table B.2: Experimental results, rod-plane 0.5m - Atmospheric conditions: $t = 17.79$ °C, $p = 1005.83$ hPa, $h = 5.59$ g/m^3

Voltage (kV)	# breakdowns	# impulses
610.6	0	1
617.3	1	3
623.3	2	6
629.0	4	8
635.2	4	7
641.7	3	7
649.2	4	6
653.9	3	4
661.5	2	3
668.5	1	1

Table B.3: Experimental results, rod-plane 0.75m +
Atmospheric conditions: $t = 17.79$ °C, $p = 1005.86$ hPa, $h = 5.59$ g/m^3

Voltage (kV)	# breakdowns	# impulses
369.3	0	1
372.9	0	2
376.2	1	5
380.5	3	12
384.1	8	10
388.3	2	2

Table B.4: Experimental results, rod-plane 0.75m -
Atmospheric conditions: $t = 17.79$ °C, $p = 1005.83$ hPa, $h = 5.59$ g/m^3

Voltage (kV)	# breakdowns	# impulses
844.1	0	5
851.0	4	9
858.3	4	9
865.6	4	9
873.6	4	4

Table B.5: Experimental results, rod-plane 1 m +
Atmospheric conditions: $t = 18.65$ °C, $p = 977.89$ hPa, $h = 7.52$ g/m^3

Voltage (kV)	# breakdowns	# impulses
466.8	0	2
471.8	1	5
475.6	2	4
479.6	1	4
484.7	2	8
489.3	5	7
494.1	2	4
499.0	2	3
504.2	1	1

Table B.6: Experimental results, rod-plane 1 m -
Atmospheric conditions: $t = 18.65$ °C, $p = 977.89$ hPa, $h = 7.52$ g/m^3

Voltage (kV)	# breakdowns	# impulses
977.8	0	1
986.9	0	1
995.8	0	2
1005.1	1	2
1013.9	0	1
1023.5	0	1
1032.2	0	1
1041.4	0	1
1049.7	0	1
1059.5	0	2
1068.5	1	5
1077.3	3	9
1086.7	6	8
1097.1	2	2

B.2. Conductor - rod

B.2.1. U_{50} tests

The conductor-rod U_{50} test was performed two times. The results of the first test are listed in Table B.7, and the results of the second test are listed in Table B.8.

Table B.7: Experimental results, conductor-rod U_{50} 0.5 m +, first time
Atmospheric conditions: $t = 16.96$ °C, $p = 993.31$ hPa, $h = 5.56$ g/m^3

Voltage (kV)	# breakdowns	# impulses
365.2	0	2
367.7	2	9
370.4	8	13
373.2	5	7
376.1	2	3
378.8	1	1

Table B.8: Experimental results, conductor-rod U_{50} 0.5 m +, second time
Atmospheric conditions: $t = 18.03$ °C, $p = 1006.38$ hPa, $h = 5.95$ g/m^3

Voltage (kV)	# breakdowns	# impulses
364.7	0	2
367.8	1	5
373.4	3	9
376.3	6	8
379.1	2	3
382.5	1	1

Table B.9: Experimental results, conductor-rod U_{50} 0.5 m -
Atmospheric conditions: $t = 16.96$ °C, $p = 993.31$ hPa, $h = 5.56$ g/m^3

Voltage (kV)	# breakdowns	# impulses
323.8	0	1
326.4	0	1
329.0	0	1
332.3	0	3
335.2	1	2
337.3	0	4
340.2	3	9
343.0	5	12
345.9	6	7
349.1	1	2
351.2	1	1

Table B.10: Experimental results, conductor-rod U_{50} 0.75 m +
Atmospheric conditions: $t = 18.03$ °C, $p = 1006.38$ hPa, $h = 5.95$ g/m^3

Voltage (kV)	# breakdowns	# impulses
506.7	0	3
511.3	3	7
516.4	4	10
520.8	7	10
525.7	4	10
531.0	6	6

Table B.11: Experimental results, conductor-rod U_{50} 0.75 m -
Atmospheric conditions: $t = 17.98$ °C, $p = 1013.54$ hPa, $h = 4.16$ g/m^3

Voltage (kV)	# breakdowns	# impulses
453.3	0	2
457.9-	2	11
462.7	8	12
467.5	4	5
476.0	1	1

Table B.12: Experimental results, conductor-rod U_{50} 1 m +
Atmospheric conditions: $t = 18.09$ °C, $p = 998.08$ hPa, $h = 4.33$ g/m^3

Voltage (kV)	# breakdowns	# impulses
632.4	0	1
639.4	1	4
645.8	2	4
652.4	2	7
658.9	4	9
665.3	4	7
671.9	2	4
679.3	1	1

Table B.13: Experimental results, conductor-rod U_{50} 1 m -
Atmospheric conditions: $t = 18.09$ °C, $p = 998.08$ hPa, $h = 4.33$ g/m^3

Voltage (kV)	# breakdowns	# impulses
599.6	0	4
604.1	4	14
609.0	9	11
613.6	2	2

B.2.2. U_{10} tests

Table B.14: Experimental results, conductor-rod U_{10} 0.5 m +
Atmospheric conditions: $t = 18.03$ °C, $p = 1006.38$ hPa, $h = 5.95$ g/m^3

Voltage (kV)	# breakdowns	# impulses	# accepted groups
364.4	0	42	6
367.2	5	30	7
369.9	2	3	2

Table B.15: Experimental results, conductor-rod U_{10} 0.5 m -
Atmospheric conditions: $t = 17.70$ °C, $p = 999.95$ hPa, $h = 5.93$ g/m^3

Voltage (kV)	# breakdowns	# impulses	# accepted groups
320.4	0	42	5
323.2	5	33	7
325.8	3	7	3
331.8	2	5	0
334.7	1	4	0
337.3	1	3	0
340.0	1	4	0

Table B.16: Experimental results, conductor-rod U_{10} 0.75 m +
Atmospheric conditions: $t = 17.98$ °C, $p = 1013.54$ hPa, $h = 4.16$ g/m^3

Voltage (kV)	# breakdowns	# impulses	# accepted groups
461.4	0	7	0
466.0	1	23	4
470.6	3	26	6
475.3	3	8	4
480.1	1	3	0
485.3	1	7	0
490.1	1	3	0
495.5	1	2	0
499.7	1	3	0
504.4	1	1	0
509.3	1	2	0
514.0	1	1	0
518.9	1	1	0
523.7	1	2	0
527.6	1	1	0

Table B.17: Experimental results, conductor-rod U_{10} 0.75 m -
Atmospheric conditions: $t = 17.98$ °C, $p = 1013.54$ hPa, $h = 4.16$ g/m^3

Voltage (kV)	# breakdowns	# impulses	# accepted groups
434.0	0	14	2
439.2	2	14	3
443.7	2	24	4
448.4	3	11	4
453.2	2	5	2
457.9	1	5	0

Table B.18: Experimental results, conductor-rod U_{10} 1 m +
Atmospheric conditions: $t = 18.09$ °C, $p = 998.08$ hPa, $h = 4.33$ g/m^3

Voltage (kV)	# breakdowns	# impulses	# accepted groups
599.8	0	7	0
605.8	1	10	2
612.4	1	30	5
619.3	4	28	6
625.7	3	11	3
632.2	1	6	0
639.8	1	6	0
645.6	1	2	0
653.0	1	1	0

During the execution of the U_{10} test for negatively stressed 1 m gaps, the resulting U_{10} seemed to be very close to the found U_{50}. More impulses than specified by [21] were applied. Table B.19 shows a large number of impulses and relatively few accepted groups.

Table B.19: Experimental results, conductor-rod U_{10} 1 m - Atmospheric conditions: $t = 18.25$ °C, $p = 1003.09$ hPa, $h = 4.87$ g/m^3

Voltage (kV)	# breakdowns	# impulses	# accepted groups
571.1	0	7	0
575.9	0	26	0
580.4	0	14	2
585.1	1	27	2
589.8	2	28	0
594.8	2	38	3
599.4	2	37	6
604.0	4	21	5
609.0	1	1	0

B.3. Disconnector conductor - rod

Table B.20: Experimental results, disconnector conductor-rod 0.5 m - Atmospheric conditions: $t = 19.01$ °C, $p = 1024.12$ hPa, $h = 6.91$ g/m^3

Voltage (kV)	# breakdowns	# impulses
290.2	0	1
299.4	0	1
308.9	0	7
311.8	5	14
314.5	7	16
317.1	8	17
319.9	8	14
322.4	8	13
325.0	8	12
327.8	3	4
330.5	1	1

Table B.21: Experimental results, disconnector conductor-rod 0.75 m - Atmospheric conditions: $t = 19.46$ °C, $p = 1024.86$ hPa, $h = 6.26$ g/m^3

Voltage (kV)	# breakdowns	# impulses
412.1	0	1
431.0	0	1
439.6	0	1
444.6	0	3
448.9	2	13
453.4	9	19
457.8	9	15
462.5	5	9
465.7	4	4

Table B.22: Experimental results, disconnector conductor-rod 1 m - Atmospheric conditions: $t = 19.82$ °C, $p = 1024.30$ hPa, $h = 5.80$ g/m^3

Voltage (kV)	# breakdowns	# impulses
509.3	0	1
527.7	0	1
546.0	0	1
564.2	0	1
583.0	0	2
587.3	0	2
592.0	2	5
596.5	2	8
601.0	6	12
602.2	0	1
605.4	5	13
609.5	8	9
614.7	1	2
618.8	2	2

B.4. Disconnector pantograph - rod

Table B.23: Experimental results, disconnector pantograph-rod 0.5 m + Atmospheric conditions: $t = 19.10$ °C, $p = 1028.08$ hPa, $h = 5.20$ g/m^3

Voltage (kV)	# breakdowns	# impulses
430.7	1	1
413.4	1	1
313.3	0	1
322.1	0	1
331.3	0	1
340.5	0	1
348.9	1	1
350.4	0	4
352.6	3	9
355.4	5	17
358.1	12	17
360.6	4	7
363.4	3	5
366.2	2	3
369.2	1	1

Table B.24: Experimental results, disconnector pantograph-rod 0.5 m - Atmospheric conditions: $t = 19.10$ °C, $p = 1028.08$ hPa, $h = 5.20$ g/m^3

Voltage (kV)	# breakdowns	# impulses
230.0	0	1
239.3	0	1
248.9	0	1
258.3	0	1
267.3	0	1
276.6	1	2
285.8	0	1
287.4	0	1
290.1	1	3
292.4	3	5
293.8	1	3
295.1	1	6
297.8	4	10
300.9	5	9
303.6	4	6
306.9	2	6
309.2	4	10
312.1	6	9
314.8	3	7
317.6	4	5
320.7	1	1

Table B.25: Experimental results, disconnector pantograph-rod 0.75 m + Atmospheric conditions: $t = 19.10$ °C, $p = 1028.08$ hPa, $h = 5.20$ g/m^3

Voltage (kV)	# breakdowns	# impulses
461.9	0	1
480.9	0	1
499.0	0	1
534.6	1	1
517.1	0	3
521.7	2	6
526.4	4	15
530.6	10	10

Table B.26: Experimental results, disconnector pantograph-rod 0.75 m - Atmospheric conditions: $t = 19.10$ °C, $p = 1028.08$ hPa, $h = 5.20$ g/m^3

Voltage (kV)	# breakdowns	# impulses
369.0	0	1
388.0	0	1
402.0	0	2
406.5	2	8
410.9	5	11
415.7	6	15
420.2	8	10
425.1	2	2

Table B.27: Experimental results, disconnector pantograph-rod 1 m - Atmospheric conditions: $t = 19.10$ °C, $p = 1028.08$ hPa, $h = 5.20$ g/m^3

Voltage (kV)	# breakdowns	# impulses
527.6	0	1
546.9	0	1
564.4	1	1
544.8	0	1
549.5	1	4
554.3	3	13
558.7	10	20
563.1	10	14
568.0	4	7
572.9	3	4
578.2	1	1

Table B.28: Experimental results, disconnector pantograph-rod modified multiple-level method 0.5 m - Atmospheric conditions: $t = 19.29$ °C, $p = 1026.80$ hPa, $h = 4.41$ g/m^3

Voltage (kV)	# breakdowns	# impulses
303.7	5	10
301.1	3	10
298.5	4	10
295.6	4	10
292.6	2	10
289.8	3	10
286.7	2	10
284.3	2	10
281.5	2	23
278.6	3	17
275.4	2	44

B.5. Disconnector pantograph - blunt needle

Table B.29: Experimental results, disconnector pantograph-blunt needle 0.5 m - Atmospheric conditions: $t = 19.29$ °C, $p = 1026.80$ hPa, $h = 4.41$ g/m^3

Voltage (kV)	# breakdowns	# impulses
263.4	0	1
273.0	0	1
277.0	0	1
279.8	1	8
282.7	7	19
285.9	11	14
287.6	1	1
288.8	3	3
292.1	1	1

Table B.30: Experimental results, disconnector pantograph-blunt needle 0.75 m - Atmospheric conditions: $t = 19.29$ °C, $p = 1026.80$ hPa, $h = 4.41$ g/m^3

Voltage (kV)	# breakdowns	# impulses
390.9	0	1
400.1	0	1
406.3	0	1
409.5	0	1
410.9	1	3
414.1	2	14
414.9	1	1
418.1	11	19
418.9	1	1
421.5	7	7
435.7	1	1

B.6. Disconnector earthing contact - needle

Table B.31: Experimental results, disconnector earthing contact-blunt needle 0.5 m - Atmospheric conditions: $t = 19.48$ °C, $p = 1028.11$ hPa, $h = 4.19$ g/m^3

Voltage (kV)	# breakdowns	# impulses
261.8	0	1
267.0	0	14
269.8	13	17
271.3	1	1
272.6	4	5
275.6	1	1

Table B.32: Experimental results, disconnector earthing contact-blunt needle 0.75 m - Atmospheric conditions: $t = 19.48$ °C, $p = 1028.11$ hPa, $h = 4.19$ g/m^3

Voltage (kV)	# breakdowns	# impulses
412.2	0	3
415.8	3	10
419.7	6	15
421.3	1	2
423.3	9	11
425.9	1	1
427.0	2	2
429.7	1	1
440.3	1	1
463.3	1	1

B.7. Needle - plane

Table B.33: Experimental results, blunt rod-plane 0.5 m + Atmospheric conditions: $t = 19.48$ °C, $p = 1028.11$ hPa, $h = 4.19$ g/m^3

Voltage (kV)	# breakdowns	# impulses
231.5	0	1
240.5	0	1
250.6	0	4
252.8	2	10
255.7	7	15
257.1	1	1
258.3	7	8
261.7	1	1
263.6	1	1

Table B.34: Experimental results, blunt rod-plane 0.75 m + Atmospheric conditions: $t = 19.48$ °C, $p = 1028.11$ hPa, $h = 4.19$ g/m^3

Voltage (kV)	# breakdowns	# impulses
332.4	0	1
337.2	0	1
341.0	0	3
343.6	1	1
344.3	2	6
348.4	3	16
351.8	11	20
355.9	8	13
359.1	5	7
364.9	2	2

Table B.35: Experimental results, hemispherical rod-plane 0.5 m + Atmospheric conditions: $t = 19.48$ °C, $p = 1028.11$ hPa, $h = 4.19$ g/m^3

Voltage (kV)	# breakdowns	# impulses
240.9	0	1
249.9	0	2
250.7	0	1
252.4	2	6
255.3	4	14
257.6	10	19
260.5	8	8